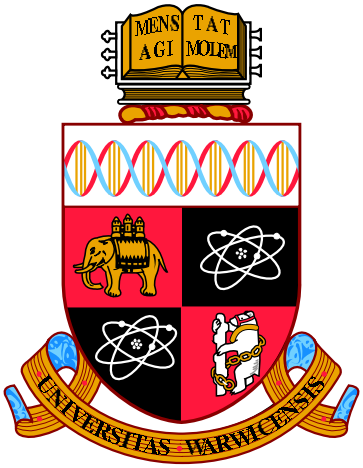

Nonequilibrium BKT Transition in Microcavity Polaritons.

by

Galbadrakh Dagvadorj

Thesis

Submitted to the University of Warwick

for the degree of

Doctor of Philosophy

Department of Physics

May 2016

THE UNIVERSITY OF
WARWICK

Contents

Acknowledgments

I feel so lucky to have been supervised by Dr Marzena Szymanska and Dr. Nick H. d'Ambrumenil, and thank them for their patient support and guidance over the course of my PhD. This dissertation would not be possible without the help of so many people in so many ways. My special thanks go for my group colleagues Dr. Jonathan Fellows, Dr. Alejandro Zamora, Dr. Themis Mavrogordatos and Kirsty Dunnett. I am also grateful to all the members of the Theory group at Physics Department, University of Warwick for providing an intellectually stimulating environment. I thank particularly my office mates Matthew Bates, Andrew Goldsborough and Daniel Pearce. From outside of the theory group, I thank Dr. Iacopo Carusotto at Universita' di Trento and Dr Francesca Marchetti at Universidad Autonoma de Madrid. Outside of physics, I thank my wife and two kids for supporting me all the time.

Declarations

I declare that the content of this thesis is original work except where referenced within the text and has not been submitted as part of any other degree or qualification. Chapters 1, 2 and 3 provide a background to the field, the information for which was gathered from the texts cited throughout. Chapter 4 is based on the following paper:

- G. D. Dagvadorj, J. M. Fellows, S. Matyjaśkiewicz, F. M. Marchetti, I. Carusotto, and M. H. Szymańska , Non-equilibrium phase transition in a two-dimensional driven open quantum system, Physics Review X 5, 041028, December 2015

The entirety of the work was conducted under the supervision of Dr. M. H. Szymańska and the content of the chapters highlighted above was performed in collaboration with the indicated authors. The thesis was typeset with LaTeX 2_ε and the warwickthesis style. Graphs were drawn using Mathematica.

Abstract

Bose-Einstein condensation where there is a macroscopic occupation of a single low energy state can occur in three dimensional systems. In two dimensions, a transition of this kind is only possible in the presence of a trap. Instead, for two-dimensional homogeneous systems, the Berezinskii-Kosterlitz-Thouless phase transition is expected, in which a phase transition is mediated by the proliferation of topological defects, governs the critical behavior of a wide range of equilibrium two-dimensional systems with a continuous symmetry, ranging from spin systems to superconducting thin films and two-dimensional Bose fluids, such as liquid helium and ultracold atoms. In this thesis, we show that this phenomenon is not restricted to thermal equilibrium, rather it survives more generally in a dissipative highly nonequilibrium system driven into a steady state. By considering a quantum fluid of polaritons of an experimentally relevant size, in the so-called optical parametric oscillator regime, we demonstrate that it indeed undergoes a phase transition associated with a vortex binding-unbinding mechanism. Yet, the exponent of the power-law decay of the first-order correlation function in the (algebraically) ordered phase can exceed the equilibrium upper limit: this shows that the ordered phase of driven-dissipative systems can sustain a higher level of collective excitations before the order is destroyed by topological defects. Our work suggests that the macroscopic coherence phenomena, observed recently in interacting two- dimensional light-matter systems, result from a nonequilibrium phase transition of the Berezinskii- Kosterlitz-Thouless rather than the Bose-Einstein condensation type.

List of Tables

List of Figures

Chapter 1

Introduction

At low temperatures many physical systems undergo a phase transition from a disordered to an ordered state in which phase coherence is spontaneously established. This spontaneously formed coherence allows pure quantum mechanical effects to be visible at mesoscopic and even macroscopic scales. The most representative examples of these effects are superconductivity and superfluidity and, more recently, Bose-Einstein condensation (BEC) [2]. Each of these phenomena have been deepened our fundamental understanding of many body physics, and have been led to novel research areas and experimental tools as well as applications.

BEC was originally a theoretical concept, and only gained application when its connection to the superfluidity of liquid Helium was realised [3]. Recent experiments in atomic gases have enabled the realisation of equilibrium BEC [4, 5], via cooling atoms then trapping only atoms with low energies, and have lead to much interest in the subject. However, atoms are heavy particles so one has to reach very low temperature to condensate. Moreover, increasing atomic gas density is quite challenging task because once density increases atoms bind together and form molecules which are more difficult to control. Nowdays, experiments on atomic gases which are probing many-body physics effects are facing a high level of sophistication [6], so the limitations of the system start showing up. This is specially true for low-dimensional systems where the fluctuations and interactions are play an important roles. In particularly, the true lower dimensional systems are not yet possible in atomic gases, only engineered lattice potentials with very periodic structures are possible in current experiments.

In 1992, Weisbuch and his co-workers showed that in a high finesse semiconductor cavity, the cavity photons, if the density is large enough, can interact strongly

Systems	Atoms	Excitons	Polaritons
Effective mass: m^*	$\sim 10^3 m_e$	$\sim 10^{-1} m_e$	$\sim 10^{-5} m_e$
Bohr radius: a_B	10^{-1}Å	10^2Å	10^2Å
Particle spacing: $n^{-1/d}$	10^3Å	10^2Å	$1.0\mu m$
Critical temperature: T_c	$1.0nK - 1.0\mu K$	$1.0mK - 1.0K$	$(1 - 300)K$
Termalization/Lifetime: $\tau_{C,T}$	1.0ms	10.0ps	(1.0-10.0)ps

Table 1.1: Comparison of characters of atoms, excitons and polaritons, adopted from [1].

with excitons in a quantum well placed inside. As a result, both particles lose their independent characters and are better described in terms of new two-dimensional quasiparticles called exciton-polaritons. This solid state implementation promises a solution to many of the obstacles presented by its atomic counterpart, and is therefore a very interesting system for studying many-body collective phenomena as well as possible applications in the field of quantum photonics. Due to the strong confinement along growth direction of the semiconductor exciton-polaritons are ideally two-dimensional system, however with more advanced growth techniques it could be even one- or zero-dimensional system.

Exciton-polaritons have light mass due to the photonic component and therefore Bose-Einstein condensation is expected at higher temperatures [1, 7]. The main relative properties of atomic, exciton and exciton-polariton gases for Bose-Einstein condensation are summarised in Table 1.1. Because of no perfect confinement of cavity, cavity photons have short lifetime, continuously leaks out of cavity, so thermal equilibrium cannot be reached in this system. Because of this continuous lose system one has to be also continuously fed by fresh particles at same rate so that a steady state with constant particle density is maintained. Indeed, this particularity of the system allows us to studies that would be otherwise impossible, and raises new questions, such as what superfluidity means in a non-equilibrium context.

The system of study in this thesis is two-dimensional. In general, it is known that Bose-Einstein condensation cannot occur in an infinite two-dimensional gas [7], but a superfluid transition of a universal character is expected to take place at low temperatures [8]. On the other hand, BEC like behaviours have been observed in different excitation regimes in exciton-polaritons [9, 10]. These half light, half matter quasiparticles that are created in semiconductor microcavities show a threshold behaviour above which a low energy state is macroscopically occupied [1, 7].

In the next chapter, we present the general equilibrium theory of Bose gas in three- and two-dimensional systems with emphasising what superfluidity is along with the background concepts that are necessary to understand the current topic. In Chapter 3, we describe first what is exciton-polaritons and how it form. Than we will introduce the regime, Optical Parametric Oscillation regime, which we studied in this thesis. We close the chapter by briefly reviewing phase space techniques which are originally developed in quantum optics context and introducing the stochastic approach. In Chapter 4, results are presented and conclusions and future possible works are in Chapter 5.

Chapter 2

Background

The aim of this chapter is to describe superfluidity in two-dimensional bosonic equilibrium systems [2]. Although the theory developed in this chapter is not directly applicable to the system of exciton-polaritons, due to its intrinsically non-equilibrium nature, it provides a good account on what superfluidity is and reveals its important features, such as quantized vortices.

We will start with tree-dimensional non-interacting Bose gas to introduce the basic concepts of Bose-Einstein Condensation (BEC) and superfluidity, then discuss their properties under rotations and weak interactions. After showing the absence of a true long range order and a true condensate at finite temperatures, the Hohenberg-Mermin-Wagner theorem, we present the Berezinskii-Kosterlitz-Thouless theory of superfluidity in two dimensional systems.

2.1 Three dimensional Bose gas and Bose-Einstein condensation

In 1924, when quantum theory was still counting its early ages and the concepts of bosons and fermions were not born yet, A. Einstein proposed that non-interacting particles, which are governed by Bose-Einstein statistics and not constrained by the Pauli exclusion principle, could occupy a single ground state in macroscopic numbers [11]. This state of matter was called a Bose-Einstein condensate. The theory received little attraction for a long time because of the phenomena was considered an anomalies feature of ideal Bose gas. Moreover, physicists believed that this phase transition would not appear in interaction gases therefore no practical application since real atoms are interact to each other so at low temperature they are in solid or

liquid phases. The first application of BEC to a physical system was by F. London in 1938 when he proposed [3, 12] that theory of BEC could explain the recent discovery of superfluid phenomena that had just been observed in liquid helium [13, 14]. The first unambiguous realization of BEC itself was achieved more than half a century after first theoretical propose in weakly interacting dilute atomic gases [4, 15].

2.1.1 Non-interacting Bose gas

The properties of ideal, non-interacting Bose gases are essentially determined by the particle quantum statistics. Quantum statistics determines how particles distribute over all possible quantum states, depending on the symmetry of the wave function upon a permutation of the particles. In the grand canonical ensemble - a system that is in contact with a large reservoir, such that it can exchange energy and particles with the reservoir - one can start with the Bose-Einstein distribution function which lead us to a criterion for BEC then we define the critical temperature and the condensate fraction for the homogeneous gas. The distribution function $f(\epsilon_\nu)$ for the average occupation of a single particle state ν with energy ϵ_ν is

$$f(\epsilon_\nu) = \frac{1}{\exp\left[\left(\epsilon_\nu - \mu\right) / \left(k_B T\right)\right] - 1}, \tag{2.1}$$

where k_B is the Boltzmann constant. The chemical potential μ is determined as a function of N-total number of particles and the temperature T by the condition that the total number of particles be equal to sum of the occupancy of individual levels. Sometimes it is more convenient to work in terms of the *fugacity* which is given by $\zeta = \exp(\mu/k_B T)$. For free bosons, this quantity is equal to unity bellow transition temperature and less than unity above. In Figure 2.1 the distribution function (2.1) is shown as a function of energy for different fugacities.

At high temperatures the chemical potential lies well bellow the energy of the lowest single particle state ϵ_0. Hence, in this limit, the average occupation number of any state is much less than unity. When temperature decreases, the chemical potential increases together with the average occupation numbers. However, because the average occupation number N_0 of the lowest single particle state with energy ϵ_0

$$N_0 = \frac{1}{\exp\left[\left(\epsilon_0 - \mu\right) / \left(k_B T\right)\right] - 1} \tag{2.2}$$

must be positive, the chemical potential cannot exceed the lowest possible energy, $\mu < \epsilon_0$. Consequently, any excited single particle state cannot exceed $N_\nu =$

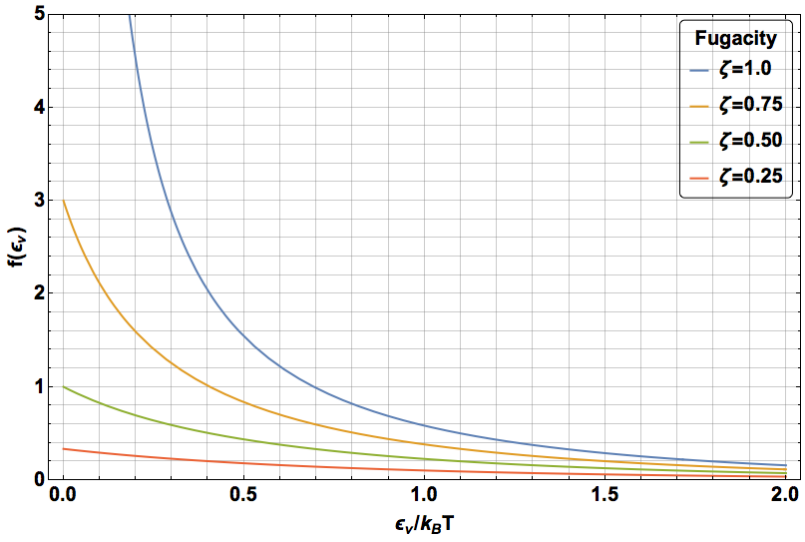

Figure 2.1: The Bose-Einstein distribution function as a function of energy for different values of the fugacity ζ.

$\frac{1}{\exp[(\epsilon_\nu-\epsilon_0)/(k_BT)]-1}$. The total number of particles N_{ex} in the excited states is just the sum

$$N_{ex} = \sum_{\nu\neq 0} N_\nu. \tag{2.3}$$

If N_{ex} is less than total number of particles N, the remaining particles must be accumulated in the lowest single-particle state, ground state, whose occupation number can be arbitrarily large since N_0 diverges as $\mu \to \epsilon_0^-$, so the system exhibits *Bose-Einstein condensation*. Knowledge about the quantum statistics, i.e. the distribution function of the particles, allows one to derive some average quantities like the total number of particles and average energy in the system

$$N = \sum_\nu f(\epsilon_\nu) \quad \text{and} \quad E = \sum_\nu \epsilon_\nu f(\epsilon_\nu). \tag{2.4}$$

In general, in order to calculate thermodynamic properties of gases, the above sums over the discrete energy levels are usually replaced by integrals, and one needs to use a density of states in which the details of the level structure are smoothed out:

$$N = \sum_\nu f(\epsilon_\nu) \approx \int_0^\infty d\epsilon f(\epsilon) g(\epsilon). \tag{2.5}$$

In the above expression $g(\epsilon)$ is the density of states. In contrast to $f(\epsilon)$ which

describes the probability of occupying a certain state, the concept of the density of states is employed for the states which are actually available in the system under consideration. Integrating the product of the two yields then the total number of particles. In order to replace the sum by an integral the density of states is required to be high. However, for a vanishing density of states this replacement might be problematic.

Density of states

Heisenbergs uncertainty relation dictates the quantisation of the phase space in quantum mechanics. In that respect, there is one quantum state per phase space cell occupying a volume equal to $(2\pi\hbar)^3$. Ascribing to a phase space region the real volume $\Delta V = \Delta x \Delta y \Delta z$ and the volume $\frac{4}{2}\pi p^3$ in momentum space which contains states with momenta smaller than p, one can express the total number of states having energy less than $\epsilon = \frac{p^2}{2m}$ as

$$G(\epsilon) = \frac{V\frac{4}{3}\pi p^3}{(2\pi\hbar)^3} = V\frac{\sqrt{2}}{3\pi^2\hbar^3}(m\epsilon)^{3/2}. \tag{2.6}$$

Hence, the density of states $g(\epsilon)$ for a homogeneous system in three dimensions can be written as

$$g(\epsilon) = \frac{dG(\epsilon)}{d\epsilon} = V\frac{\sqrt{2}}{3\pi^2\hbar^3}m^{3/2}\epsilon^{1/2}. \tag{2.7}$$

The density of states in the majority of cases can be expressed as a function of the energy in the form

$$g(\epsilon) = C_\alpha \epsilon^{\alpha-1}, \tag{2.8}$$

where C_α is a constant. For the homogeneous case in d dimensions we find $\alpha = d/2$, while for the harmonic oscillator in d dimensions one has $\alpha = d$. It is worth noting here that the density of states for the homogeneous two dimensional system proves to be independent of the energy. This implies that Bose condensation in a two dimensional box can only take place at zero temperature.

We will now study the behaviour of the expression (2.5) keeping the temperature T fixed but adding progressively more particles to the system. The density $n = N/V$ will consequently rise and we can write

$$n = \frac{N}{V} = A\int_0^\infty d\epsilon \frac{\epsilon^{1/2}}{\exp\left(\frac{\epsilon-\mu}{k_B T}\right)}, \tag{2.9}$$

where we have defined the prefactor $A = \sqrt{2}m^{3/2}/(3\pi^2\hbar^3)$. An increase in the density follows from an increase in the chemical potential. Since the latter can only be negative (otherwise $f(\epsilon)$ would yield unphysical negative occupation numbers), the maximum allowed value is zero if the minimum energy ϵ_0 is set to zero. A further implication is that the density of the system appears to be bound by a maximum value:

$$n_c = n(\mu = 0) = A\int_0^\infty d\epsilon \frac{\epsilon^{1/2}}{\exp\left(\frac{\epsilon}{k_BT}\right)} = A(k_BT)^{3/2}\int_0^\infty dx \frac{x^{1/2}}{e^x - 1}, \tag{2.10}$$

with the substitution $x = \epsilon/(k_BT)$. We can evaluate this integral with recourse to the Gamma function $\Gamma(\alpha)$ and the Riemann zeta function $\zeta(\alpha)$: $\int_0^\infty dx \frac{x^{\alpha-1}}{e^x-1} = \Gamma(\alpha)\zeta(\alpha)$. In our case we have $\alpha = 3/2$ and we then find

$$n_c = A\Gamma(3/2)\zeta(3/2) = 2.3A. \tag{2.11}$$

This result is manifestly unphysical, as the density of the system is bound in spite of the increase in the particle number. We might then ask what happens to the particles we add? The mistake we committed occurred when we replaced the sum by an integral, which is invalid when the density of states is small. In fact, this is the case for a three-dimensional homogeneous system. In order to correct this mistake, we ought to separate the lowest energy state from all the excited states, so that

$$n = n_0 + n_{\text{ex}} = \frac{1}{V}\frac{1}{e^{-\mu/(k_BT)} - 1} + A\int_0^\infty d\epsilon \frac{\epsilon^{1/2}}{\exp\left(\frac{\epsilon-\mu}{k_BT}\right)}. \tag{2.12}$$

If we now consider the limit $\mu \to 0$, corresponding to an increase in the number of particles available in our system, the second term will be bound to n_c, which is the critical density, while the first term, n_0, can grow without bounds as $\frac{1}{V}\frac{1}{e^{\to 0}-1} \to \infty$. The ground state of the system will accommodate any additional particle in excess of the critical density. The ground state then becomes macroscopically occupied, giving rise to the phenomenon of *Bose-Einstein condensation* (BEC).

The formation of a BEC is an admirable result in its own right, since there is no particle at a specific energy in a normal gas, but particles that only belong to a given energy interval. Finding a particle at a specified point in space has zero probability. In a similar fashion, a point has zero volume and therefore will never be occupied in a continuum of states. By analogy, the ground state represents a specific

point in phase space which becomes macroscopically occupied.

Phase space density at the phase transition

It proves useful to write the critical density n_c as a function of the thermal de Broglie wavelength $\lambda_T = \sqrt{\frac{2\pi\hbar^2}{mk_BT}}$, which can be construed as the spatial extent of a particle wave function. We can then write

$$n_c = 2.3A(k_BT)^{3/2} = 2.3\frac{2}{\sqrt{\pi}}\frac{1}{\lambda_T}. \tag{2.13}$$

The critical density at which BEC sets in is thus reached if the interparticle distance is of the order of the thermal de Broglie wavelength. At that density the corresponding wave packets of the individual particles begin to overlap, and the system Bose condenses under the influence of quantum statistics.

Transition temperature and condensate fraction

We will now give expressions for the critical temperature T_c, below which the ground state of the system becomes macroscopically occupied, and for the corresponding condensed atomic fraction $n_0 = N_0/N$ below the critical temperature. We simplify our treatment by setting $\epsilon_0 = 0$.

In order to find the critical temperature we fix the system at the critical point, where all the particles are occupying the excited energy states with density

$$n = \frac{N}{V} = \frac{N_{\text{ex}}}{V} = A\Gamma(3/2)\zeta(3/2)(k_BT_c)^{3/2}, \tag{2.14}$$

such that

$$k_BT_c \approx 3.31\frac{\hbar^2n^{2/3}}{m}. \tag{2.15}$$

The expression for condensate fraction n_0 can now be derived from

$$n = n_0(T) + n_{\text{ex}}(T) = n_0(T) + A\Gamma(3/2)\zeta(3/2)(k_BT)^{3/2}. \tag{2.16}$$

If a BEC is formed in the system, the second term will remain fixed at the critical density n_c. We can replace the coefficients of the second term making use of the expression (2.14), to find

$$n = n_0(T) + n\left(\frac{T}{T_c}\right)^{3/2}. \tag{2.17}$$

The condensate fraction, finally, reads

$$n_0 = \frac{N_0}{N} = 1 - \left(\frac{T}{T_c}\right)^{3/2}. \tag{2.18}$$

In the next part we will give the general description of continuous phase transitions and underline their key concepts related to BEC, in particular symmetry breaking and the concept of the order parameter.

2.1.2 Spontaneous symmetry breaking, order parameter and long range order

Phase transitions are the cooperative phenomena associated with a global change of structure and the related physical properties of a system which is subject to a continuous change of a certain external conditions, such as temperature, pressure, or others. A phenomenological theory of second order phase transitions was proposed by Landau in 1937 [16] and since then has attracted a lot of interest because of its simplicity and universality in terms of its application. The Landau theory can be used to describe a wide range of phase transitions. Notable examples include the ferroelectric, structural and magnetic, but equally the superconducting and superfluid phase transitions. The arguments are based on thermodynamic principles through the unification of various mean field theories. In that context we give emphasis on two closely related important, general concepts: broken symmetry and the order parameter.

Broken symmetry

Symmetry breaking very often accompanies a phase transition. Here, symmetry is to be understood as the invariance of certain physical quantities under some operations, which may form a closed set (called a *symmetry group*). The physical properties of the liquid state, for example, are invariant to arbitrary translations and rotations, i.e. invariant under the action of the elements in the Euclidean group $E(3)$.

A physical system is described by a Hamiltonian. The symmetry possessed by that system is reflected in the invariance of the Hamiltonian under a particular class of transformations.

Subject to the change of macroscopic conditions (e.g. an increase temperature, a decrease in pressure, or the application of an external field) one or more symmetry elements may vanish: this is namely the phenomenon of broken symme-

try. Broken symmetry refers to a situation in which a particular state does not have the full symmetry possessed by the system Hamiltonian. A well-known example is that of a magnetic system: at temperatures above the Curie temperature the system has zero magnetization for zero external field; it is therefore symmetric, i.e. there is no preferred direction of the magnetization. As the temperature is lowered below the Curie temperature, however, a spontaneous magnetization develops in a specific direction, breaking down the full anterior symmetry.

We will now discuss a structural phase transition. Here, the symmetry may be transformed from the liquid to a crystalline state the temperature decreases. This process breaks continuous translation and rotation symmetries. The symmetry group of the broken symmetric state is a subgroup of the initial group in numerous cases of second order phase transitions,

We can distinguish between two types of broken symmetries: the spontaneous breaking where the Hamiltonian H remains invariant, and the externally disturbed, $H \to H + H'$, where H' is a perturbation addition to the original Hamiltonian H.

Order parameter

We shall now proceed to give a quantitative description of phase transitions that occur in a given system. Invoking the concept of broken symmetry we discussed above, we can classify phase transitions through the loss or gain of some symmetry elements subject to the change of macroscopic system variables. When a system is transformed from a high symmetry to a low symmetry phase, there is a physical quantity η, called the *order parameter*, varying in such a fashion that it assumes a zero value in the high symmetry phase and non-zero values in the low symmetry phase. In the famous example of a magnetic transition, for instance, the parameter η may be taken as the macroscopic magnetic moment per unit volume of a ferromagnet undergoing the transition.

Since the order parameter is intimately related to the symmetry of a system, the high symmetry phase can be called the *disordered phase*, and the low symmetry phase the *ordered phase*. In the spirit of the Landau theory of phase transitions, a macroscopic order parameter η may be defined to measure the ordered phase below the transition temperature T_c. We consider this variable η a thermodynamic variable, namely the ensemble average of a microscopic variable σ_i, which is a function of the space and time coordinates. The time and spatial distributions are important for the averaging of such statistical variables. Above the critical temperature T_c, in the

disordered phase, those variables σ_i are usually performing a fast random motion with their time average $\langle \sigma_i \rangle_t$ vanishing at each point independently of the site i. Below T_c, on the other hand, the variables are correlated while performing slow motion. Their spatial distribution dominates the behaviour of the ordered phase.

We will emphasize once more that the symmetry of a system is altered only when η becomes different to zero. Any nonzero value of the order parameter, even arbitrarily small, brings about a lowering of the symmetry. Although the change of symmetry is always abrupt, the order parameter can vary in two distinct fashions. The order of the transition is decided upon the manner by which the symmetry is

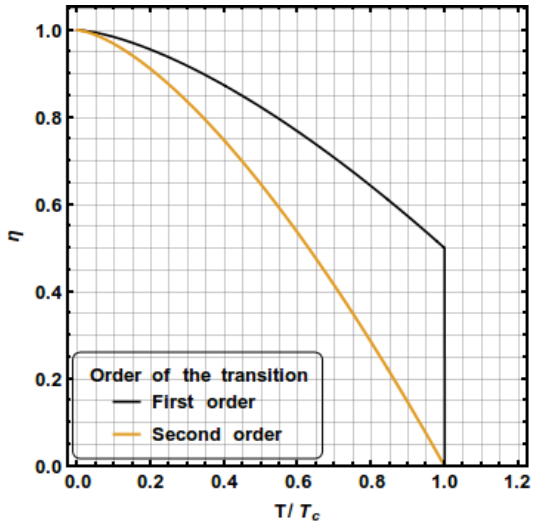

Figure 2.2: Variation of the order parameter as a function of a control parameter in first and second order phase transitions. Here, η is the order parameter with the temperature playing the role of the control parameter.

broken. Generally speaking, there are phase transitions of two kinds. One is the *first order* phase transition, in which the order parameter varies discontinuously in the region of the transition temperature T_c. The two symmetry groups for the high symmetry phase and low symmetry phase are not necessarily subject to any group-subgroup relationship.

The other kind is the *second order* phase transition, also known as the continuous phase transition, in which the order parameter varies continuously. In contrast to the first order transition, in this case the symmetries on the two sides of the transition are connected, with the symmetry group on the lower symmetry phase being a subgroup of the higher symmetry phase.

We have seen in the previous sections that the condensate fraction N_0/N in a BEC is different to zero below the critical temperature T_c, and tends to zero above that temperature value. It appears then that the condensate fraction N_0/N would be an anticipated choice for the order parameter. It will prove more useful, however, to define a single quantity providing information simultaneously on the number of particles in the condensate as well as on and the single particle state in which condensation takes place. With that in mind, if $\psi_0(\mathbf{r})$ is the wavefunction of the lowest energy state with population N_0, we define the order parameter for a BEC transition occurring in a non-interacting Bose gas as below

$$\Psi(\mathbf{r}) \equiv \sqrt{N_0}\psi_0(\mathbf{r}). \tag{2.19}$$

The BEC is a second order phase transition since the order parameter gradually increases when crossing the transition temperature, while the spontaneous breaking of symmetry reflects the gauge symmetry.

Long range order

In the most general case, the system we are considering can be described by a statistical mixture of mutually orthogonal states m with weights p_m. We can then define the one-body density matrix as

$$\begin{aligned} n^{(1)}(\mathbf{r},\mathbf{r}') &\equiv N\sum_m p_m \int d\mathbf{r}_2 d\mathbf{r}_3 ... d\mathbf{r}_N \psi_m^*\left(\mathbf{r},\mathbf{r}_2,..,\mathbf{r}_N\right)\psi_m\left(\mathbf{r}',\mathbf{r}_2,..,\mathbf{r}_N\right) \\ &\equiv \left\langle \hat{\psi}^\dagger(\mathbf{r})\hat{\psi}(\mathbf{r\prime})\right\rangle. \end{aligned} \tag{2.20}$$

Since the operator $n^{(1)}(\mathbf{r},\mathbf{r}')$ is Hermitian, it can be diagonalized, with

$$n^{(1)}(\mathbf{r},\mathbf{r}') = \sum_i n_i \chi_i^*(\mathbf{r})\chi_i(\mathbf{r}'). \tag{2.21}$$

The phenomenon of BEC occurs when only one of the above eigenvalues n_i is of order N, while all the rest are of the order of unity. We label the macroscopically occupied state that corresponds to the eigenvalue n_i as $i \equiv 0$ and its occupation number as $n_{i=0} \equiv N_0$. We are able then to define the order parameter similarly to (2.19)

$$\Psi(\mathbf{r}) \equiv \sqrt{N_0}\chi_0(\mathbf{r}). \tag{2.22}$$

The system is in a normal state if all the eigenvalues n_i of the density matrix are of

the order of unity. On the other hand, if two or more eigenvalues n_i are of order N, the system exhibits a so-called *fragmented BEC*.

The diagonal part of the one-body density matrix ($\mathbf{r} = \mathbf{r'}$) yields the particle density, while the off-diagonal part ($\mathbf{r} \neq \mathbf{r'}$) measures the established coherence between distant points in space. In order to understand its behaviour we consider the momentum distribution

$$n(\mathbf{p}) = \left\langle \hat{\psi}^\dagger(\mathbf{p})\hat{\psi}(\mathbf{p}) \right\rangle, \tag{2.23}$$

where $\hat{\psi}(\mathbf{p}) = (2\pi\hbar)^{-3/2} \int d\mathbf{r} \exp[i\mathbf{rp}/\hbar]\hat{\psi}(\mathbf{r})$ is the expression of the field operator in momentum (Fourier) space. In a homogeneous system, the elements $n^{(1)}(\mathbf{r}, \mathbf{r'})$ depend only on the relative distance $\mathbf{s} \equiv \mathbf{r} - \mathbf{r'}$ between the particles. The Fourier transform of the momentum distribution reads

$$n^{(1)}(\mathbf{s}) = \frac{1}{V} \int d\mathbf{p} n(\mathbf{p}) e^{-i\mathbf{sp}/\hbar}, \tag{2.24}$$

with V the total volume of the homogeneous system. In a non-interacting BEC, the lowest energy state with zero momentum is macroscopically occupied, so the density distribution exhibits the singular behaviour

$$n(\mathbf{p}) = N_0 \delta(\mathbf{p}) + \tilde{n}(\mathbf{p}), \tag{2.25}$$

where $\tilde{n}(\mathbf{p})$ is a smooth function. The long-distance behaviour of $n^{(1)}(\mathbf{s})$ is then determined predominantly by the delta function in the first term. In particular, the momentum distribution approaches a non-zero value as $s \to \infty$

$$n^{(1)}(\mathbf{s})_{s\to\infty} \to \frac{N_0}{V}. \tag{2.26}$$

This behaviour is termed as *off-diagonal long-range order*.

The distribution function $n^{(1)}(\mathbf{s})$ provides information on the thermodynamics of the system and the mechanism by which order is established. We refer the reader to section 2.2 for more details on the case of a two-dimensional Bose gas, and the calculation of $n^{(1)}(\mathbf{s})$ in several limiting cases.

In the exciton polariton system, the distribution $n^{(1)}(\mathbf{s})$ can be experimentally measured. As we will see in Chapter 4, in an interference experiment between two points separated by distance $\mathbf{s}$, in a similar fashion to a Young's double slit setup, this function is proportional to the fringe visibility.

We also define for convenience the first order correlation function $g^{(1)}(\mathbf{s})$, taking $n^{(1)}(\mathbf{s})$ and normalizing by the local particle density

$$g^{(1)}(\mathbf{r}) = \frac{\left\langle \hat{\psi}^\dagger(\mathbf{r}+\mathbf{s})\hat{\psi}(\mathbf{r}) \right\rangle}{\sqrt{\left\langle \hat{\psi}^\dagger(\mathbf{r}+\mathbf{s})\hat{\psi}(\mathbf{r}+\mathbf{s}) \right\rangle \left\langle \hat{\psi}^\dagger(\mathbf{r})\hat{\psi}(\mathbf{r}) \right\rangle}}. \tag{2.27}$$

Because of their close connection the two quantities are often used interchangeably.

2.1.3 Interacting Bose gas

In order to describe the behaviour of an interacting system we cannot resort to a collection of particles each one occupying a single-particle state. One instead employs a many-body state wavefunction $\psi_n(\mathbf{r}_1, \mathbf{r}_2, .., \mathbf{r}_N)$, where N is the total number of particles, $\mathbf{r}_i$ is the radius vector of the i-th particle, and the function ψ_n is symmetric under the exchange of any index pair (here we are considering Bose statistics).

We describe quantitatively such an interacting BEC state by making the simplest possible ansatz for the many-body wavefunction ψ_N in a system of N bosons all occupying the same state

$$\psi_N(\mathbf{r}_1, \mathbf{r}_2, ..., \mathbf{r}_N; t) = \prod_{i=1}^{N} \chi_0(\mathbf{r}_i, t). \tag{2.28}$$

In the absence of interactions, the wavefunctions $\chi_0(\mathbf{r}_i, t)$ would satisfy the time dependent Schrödinger equation

$$i\hbar \frac{\partial \chi_0(\mathbf{r}, t)}{\partial t} = \left[-\frac{\hbar^2}{2m^*}\nabla^2 + V_{ext}(\mathbf{r}, t) \right] \chi_0(\mathbf{r}, t), \tag{2.29}$$

where m is the single particle mass and $V_{\text{ext}}(\mathbf{r}, t)$ is a potential which is externally applied to the system. The contact interaction generates an effective potential of the form $N_0 g|\chi_0(\mathbf{r}, t)|^2$. Adding this nonlinear term in (2.29) yields

$$i\hbar \frac{\partial \chi_0(\mathbf{r}, t)}{\partial t} = \left[-\frac{\hbar^2}{2m^*}\nabla^2 + V_{\text{ext}}(\mathbf{r}, t) + N_0 g|\chi_0(\mathbf{r}, t)|^2 \right] \chi_0(\mathbf{r}, t). \tag{2.30}$$

The above equation serves as a self-consistent mean-field approximation. We anticipate it to be a satisfactory approximation for a reasonably weak and short-ranged interaction. We then substitute the order parameter (2.22) for $N_0\chi_0(\mathbf{r}, t)$, and arrive

finally at the (time-dependent) Gross-Pitaevskii equation (GPE)

$$i\hbar\frac{\partial\Psi(\mathbf{r},t)}{\partial t} = \left[-\frac{\hbar^2}{2m^*}\nabla^2 + V_{ext}(\mathbf{r},t) + g|\Psi(\mathbf{r},t)|^2\right]\Psi(\mathbf{r},t). \tag{2.31}$$

If the external potential $V_{\rm ext}(\mathbf{r},t)$ is time-independent, then (2.31) admits solutions of the form $\Psi(\mathbf{r})\exp(-i\mu t/\hbar)$, where $\Psi(\mathbf{r})$ satisfies the time-independent GPE

$$\mu\Psi(\mathbf{r}) = \left[-\frac{\hbar^2}{2m^*}\nabla^2 + V_{ext}(\mathbf{r},t) + g|\Psi(\mathbf{r})|^2\right]\Psi(\mathbf{r}). \tag{2.32}$$

The equation (2.32) can also be derived [17] from the requirement that $\Psi(\mathbf{r})$ minimizes the total energy functional

$$E = \frac{\hbar^2}{2m^*}\int|\nabla\Psi(\mathbf{r})|^2 d\mathbf{r} + \int V_{ext}(\mathbf{r})|\Psi(\mathbf{r})|^2 d\mathbf{r} + \frac{1}{2}g\int|\Psi(\mathbf{r})|^4 d\mathbf{r}, \tag{2.33}$$

under the constraint (normalization condition)

$$\int|\Psi(\mathbf{r})|^2 d\mathbf{r} = N, \tag{2.34}$$

where N is the total particle number. The time dependence is fixed by the chemical potential, μ, which is just the Lagrange multiplier associated with the particle number conservation (2.35), namely

$$\mu = \frac{\partial E}{\partial N}. \tag{2.35}$$

In a spatial region with a density $n_0(\mathbf{r}) = |\Psi(\mathbf{r})|^2$ remaining nearly constant, a characteristic length can be defined as

$$\xi = \frac{\hbar}{\sqrt{2m^* g n_0}}. \tag{2.36}$$

The quantity ξ is called the *healing length*, providing the length scale over which $\Psi(\mathbf{r})$ can change appreciably. In order to render our point more explicit, we consider a configuration where a condensate is confined in a box, with the order parameter vanishing on the wall (which we take as the plane $z = 0$). Then, as $z \to 0^+$, the function $\Psi(z)$ decays to zero as $\tanh[z/(2\xi)]$. We can interpret therefore the healing length as a screening length of a sort, since barriers (e.g. walls) are not visible at distances larger than ξ. In 2.1.5, we will deduce that ξ is also the size of the vortex

core.

2.1.4 Superfluidity

Superfluidity is the ensemble of phenomena first attributed to liquid helium below the critical transition temperature of 2.17 K. The specific heat data, when plotted against temperature, resemble the Greek letter lambda (λ) in the region of the phase transition, hence this temperature is termed the (λ)-point. The state of liquid helium above the (λ)-point is traditionally called Helium I (or He I), and below the (λ)-point Helium II (or He II). The term *superfluidity* was coined by Kapitza, who employed it to describe experiments of zero friction in the liquid flow in his laboratory in Moscow [13]. Superfluidity was simultaneously and independently discovered by Allen and Misener [14] in Cambridge, who investigated experimentally the flow of liquid helium through small glass capillaries. F. London suggested soon afterwards that BEC might be akin to this new phase, since the calculated BEC transition temperature and the associated entropy change abide very well to the values measured experimentally [3, 12].

The explanation of transport phenomena, such as zero friction and the fountain effect, necessitated the proposal of the two-fluid model by Tisza [18]. For the history of this discovery the reader is referred to [19]. In this section, we will review the properties of superfluidity related to exciton polariton condensation.

The two-fluid model

The empirical two-fluid model can explain many of the properties of He II [2, 20]. In that framework, one assumes that the liquid is composed of a normal and a superfluid component, each one having their own local velocities: ($\mathbf{v}_n$ for the normal component, and $\mathbf{v}_s$ for the superfluid component) together with an effective mass density (ρ_n and ρ_s respectively). The total (mass) current density is equal to the sum of the current densities of each component

$$\mathbf{j} = \rho_n \mathbf{v}_n + \rho_s \mathbf{v}_s. \tag{2.37}$$

The normal component possesses ordinary viscosity, while the superfluid component is capable of flow without friction. The ratio of the superfluid component density over the total density is called the *superfluid fraction*. Above the transition temperature, the superfluid fraction is zero. As the temperature is decreased below the λ-point,

the superfluid fraction increases and reaches unity at zero temperature. Therefore, the statement "He II shows zero viscosity" is not generally valid. If the normal component participates in the motion for some experiment, the measured viscosity will be different from zero.

The superfluid fraction should not be confused with the condensate fraction appearing in 2.1.1. In particular, the superfluid fraction in He II is unity at $T = 0$, whereas the condensate fraction is believed to be around 10% at that temperature. In addition, the superfluid and normal components cannot be physically separated, nor can one assign certain atoms to one component and the rest to the other.

Landau was the first who attempted to justify theoretically the two-fluid model [21]. He portrayed helium as a background liquid in which elementary excitations can be created move about. At zero temperature, there are no excitations, and the liquid exhibits no viscosity. As the temperature increases, excitations are created, which can collide amongst themselves as well as with the walls of the thin capillaries causing friction and hence dissipation. In this picture, the background perfect liquid is the superfluid component, while the normal component comprises the gas of excitations.

Employing hydrodynamic arguments, Landau deduced that the important low-energy excitations are of two kinds: phonons with a linear dispersion relation $E_{\rm ph} = pc$ where p is the momentum and c is the speed of sound, and another kind called *rotons* following the dispersion law $E_{\rm rot} = \Delta + p^2/2m$. Following comparison with experimental data that became available at a later time, the above dispersion relation was modified to

$$E_{\rm rot} = \Delta + \frac{(p - p_0)^2}{2m}. \tag{2.38}$$

In the above expression, c, Δ, p_0 and m are the free parameters of the model determined from fits to the measured thermodynamic quantities [22]. Feynman demonstrated later that both phonons and rotons are part of the same dispersion line [23], developing a microscopic theory of He II. According to this theory there are no other excitations in the low-energy part of the spectrum [24]. A very instructive review of these arguments can be found in [25]. The microscopic theory of the excitation spectrum was subsequently refined [26] and corroborated in experiments of neutron scattering [27].

Landau critical velocity

The Landau criterion is the most widely used in order to assess the presence of superfluidity. This provides however a necessary, but not sufficient condition. In addition, it is usually difficult to analyse experiments which are designed based on this criterion. We will now discuss two additional experimental situations addressing superfluid phenomena.

Let us consider the motion of a large body having mass M and moving with velocity $\mathbf{v}_i$ inside a liquid. If this movement can give rise to excitations inside the liquid then dissipation can occur. According to Landau the special form of excitation spectrum in He II prevents any particles of being excited if the mass M has a velocity smaller than a critical value, the so-called *Landau critical velocity.*

In order to ascertain this fact, let us assume that the mass M scatters a particle of the liquid, changing its velocity to $\mathbf{v}_f$. If the emerging particle has momentum $\mathbf{p}$ and energy $\epsilon(p)$, then employing energy and momentum conservation we obtain

$$\frac{1}{2}M\mathbf{v}_i^2 = \frac{1}{2}M\mathbf{v}_f^2 + \epsilon(p) \tag{2.39}$$

$$M\mathbf{v}_i = M\mathbf{v}_f + \mathbf{p}. \tag{2.40}$$

We can eliminate $\mathbf{v}_f$ from the above system of equations to obtain

$$\epsilon(p) = \mathbf{p}\cdot\mathbf{v}_i + \frac{p^2}{2M}. \tag{2.41}$$

In most experiments the last term in (2.41) can be neglected since the mass M is large. We easily deduce that (2.41) can be satisfied, with an excitation being created, only if

$$v_i \geq \frac{\epsilon(p)}{p}. \tag{2.42}$$

Hence, the Landau critical velocity reads

$$v_L = \left[\frac{\epsilon(p)}{p}\right]_{\min}. \tag{2.43}$$

If the excitations in the liquid follow the free-particle dispersion relation $\epsilon(p) = p^2/2m$, it is clear that the Landau critical velocity (2.43) is zero. The dispersion law for $\epsilon(p)$ must be linear in terms of p at small momenta for a critical velocity different to zero. In the weak interaction limit for a Bose gas showing BEC, the

quasi-particle dispersion at small momenta is linear according to the prediction of Bogoljubov [2, 28, 29]. Later, Feynman and Cohen [23, 26] calculated the excitation spectrum of He II, and derived a linear relation for small momenta. Cowley and Woods verified experimentally that prediction in 1971 [27].

A complementary experiment would have the liquid moving inside a tube. One could then follow the above analysis in the reference frame where the liquid is at rest. Of course, at non-zero temperature, the finite normal component is going to move as a normal liquid and cause friction with the moving object or the walls. But if the diameter of the tube is too small, motion of the normal component is completely blocked, and only the superfluid component participates in the motion. This was the case in the experiments by Kapitza [13] and by Allen and Misener [14].

As mentioned before, the Landau criterion is not a sufficient condition for superfluidity, which is a collective phenomenon. When a superfluid moves, all particles participate coherently in this motion. Therefore, phase coherence needs to be established across the whole volume. The idea of phase coherence and long range order is the basis of the modern understanding of superfluidity [30].

Furthermore, experiments designed with the aim of testing directly the Landau criterion are difficult to analyse. In particular, when a large object moves inside a superfluid, or when a superfluid enters a small tube, turbulent flow occurs and vortices can be excited. Creation and movement of vortices causes dissipation, as will be discussed in section 2.1.5, so the critical velocity measured in this type of experiments is almost always smaller than what equation (2.43) implies. In He II, v_L has only been measured in complicated experiments in which charged ions are moving inside the liquid under an applied electric field [31].

Superfluids under rotation

Simpler conceptual manifestations of superfluidity occur when a superfluid is subject to rotation [30]. We firstly assume that the superfluid component of (2.37) can be described by an order parameter similar to (2.22). But now $|\Psi(\mathbf{r})|$ represents the superfluid density instead of the condensate density. This assumption is not based on firm theoretical grounds. There is strong evidence that the type of BEC occurs in He II (with condensate fraction 10% at $T = 0$), and superfluid phenomena have been observed in atomic BECs. But as we shall see in section 2.2.4, superfluidity can occur without BEC. Therefore, one can only argue that, based on the current experimental facts, the phase coherence established across 3D superfluids allows the

description of the superfluid component by a complex order parameter $|\Psi(\mathbf{r})|$. The wavefunction $\Psi(\mathbf{r})$ is characterized by its amplitude $|\Psi(\mathbf{r})|$ and phase $\phi(\mathbf{r})$:

$$\Psi(\mathbf{r}) = |\Psi(\mathbf{r})| \exp[i\phi(\mathbf{r})]. \tag{2.44}$$

Similar to the usual definition of probability density and current density in quantum mechanics, we can define the superfluid density $\rho_s(\mathbf{r})$ and current $\mathbf{j}_s(\mathbf{r})$ as below

$$\rho_s(\mathbf{r}) = |\Psi(\mathbf{r})|^2, \tag{2.45}$$

$$\mathbf{j}_s(\mathbf{r}) = -\frac{i\hbar}{2m^*}\Psi^*(\mathbf{r})\nabla\Psi(\mathbf{r}) + \text{c.c} = |\Psi(\mathbf{r})|^2 \frac{\hbar}{m^*}\nabla\phi(\mathbf{r}). \tag{2.46}$$

The ratio $\mathbf{j}_s(\mathbf{r})/\rho_s(\mathbf{r})$ has units of velocity. We call it the *superfluid velocity*, and it depends only on the superfluid phase

$$\mathbf{v}_s \equiv \frac{\hbar}{m^*}\nabla\phi(\mathbf{r}). \tag{2.47}$$

A quantity similar to (2.47) can be defined for a single-particle wavefunction, but in that case it represents something quite different. The velocity of a single particle cannot be measured locally. When one measures the velocity of a particle, the measurement result depends on the values of the wavefunction everywhere in space. A superfluid, however, is a collective state of many particles, so it does not follow the uncertainty relations of quantum mechanics. The term v_s in (2.43) represents the local collective velocity of the superfluid component, which can be measured classically with arbitrary accuracy. In conclusion, v_s represents a classical quantity that describes a collective quantum mechanical phenomenon.

An immediate consequence of the definition (2.43) is that wherever $\Psi(\mathbf{r})$ is non-zero (so that $\phi(\mathbf{r})$ is well defined)

$$\nabla \times \mathbf{v}_s = 0 \tag{2.48}$$

This results means that the velocity field is irrotational. The integral of $\mathbf{v}_s$ over a closed contour will be zero unless the contour encloses one or more singularities, namely points where $\Psi(\mathbf{r})$ vanishes. Since $\phi(\mathbf{r})$ is defined modulo 2π, the change of phase $\Delta\phi$ around a contour can only be an integer multiple of 2π

$$\Delta\phi = \oint \nabla\phi \cdot d\mathbf{l} = 2\pi l, \quad l = 0, \pm 1, \pm 2, \ldots \tag{2.49}$$

Consequently, the circulation Γ around a close contour is quantized

$$\Gamma = \oint \mathbf{v}_s \cdot d\mathbf{l} = l\frac{\hbar}{m^*}. \tag{2.50}$$

This is the expression of the *Onsager-Feynman quantization condition.*

The quantization condition (2.50) predicts the appearance of quantized vortices. Here, we will employ it to describe the behaviour of liquid helium in the geometry of Figure 2.3, namely the annular region between two concentric cylinders [30]. Assume that the radius of the inner cylinder is only slightly smaller that the radius of the outer cylinder, so that the liquid is confined in a narrow circular region of mean radius R. At temperatures higher than the λ-point, liquid helium behaves as a normal liquid. Below the λ-point, the mass flow is described by the two-fluid equation (2.37). The normal component behaves as a (normal) liquid, hence in equilibrium $\mathbf{v}_n$ should be zero in the frame of reference in which the walls of the container are at rest. The superfluid component, on the other hand, follows (2.50). When the temperature is lowered below the λ-point, the quantization factor l in (2.50) is "locked" to an integer value so that the superfluid velocity $\mathbf{v}_s$ is closest to the initial liquid velocity before the cool down. With the above considerations in mind, let us consider the following experiment: we start with liquid He at a finite temperature above the λ-point, and rotate the cylinders with some small angular frequency ω. While continuously rotating the cylinders, we subsequently cool down the sample below the λ-point. The state of the normal component will not change, so it will continue to rotate together with the cylinders having a speed ωR. However, the superfluid velocity is constrained by (2.50). If $\omega \ll \hbar/(mR^2)$, l in equation (2.50) is going to "lock" to the value $l = 0$, in accordance to the previous argument, and the superfluid component will seize to rotate. In this experiment the angular momentum of the liquid is reduced by a factor $\rho_n(T)/\rho$ when the temperature is lowered below the λ-point, where $\rho_n(T)$ is the mass density of the normal component at temperature T, and ρ is the total density. If the total angular momentum is conserved in the experimental configuration, the container will start rotating faster as the temperature drops. This is a reversible change in the angular momentum of the liquid. If we now increase the temperature above the λ-point, the whole liquid will start rotating again. This effect is often referred to as *non-classical rotational inertia*, or Hess-Fairbank effect [32]. It is analogous to the Meissner effect in superconductors and serves as a manifestation of the equilibrium behaviour of the system.

A second experimental setup involving rotation would be the following: we

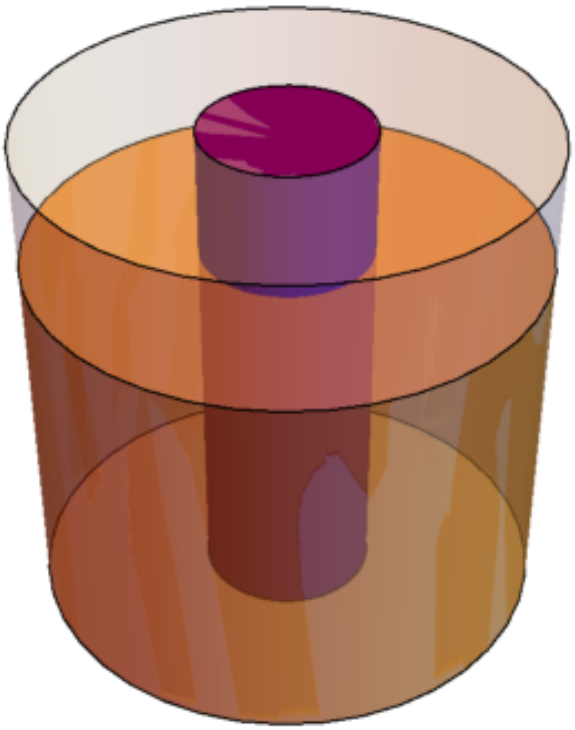

Figure 2.3: Cartoon for rotating liquid helium experiment. The liquid has a orange colour, and is confined between two concentric cylinders, so that it does not penetrate the central cylinder, which is shown in black. The cylinders can rotate around their axis.

start again with a liquid above the λ-point, but this time we spin the cylinders faster, so that the angular frequency is $\omega \gg \hbar/(mR^2)$. When we cool down the liquid while still subjecting it to rotation, a suitable integer value l will be established in equation (2.50), and the superfluid angular momentum will not change appreciably. At this point, after having reached a sufficiently low temperature, we suddenly stop rotating the cylinders. The velocity of the normal component will then decay fast to zero, but the superfluid component will keep rotating. Moreover, by sweeping the temperature up and down (but all the time keeping it below the λ-point), the value of the quantization constant l will be preserved, so the superfluid angular momentum will change. This is the phenomenon of *metastable superflow*, which is a manifestation of the long relaxation times associated with superfluid flow. Because

of the large number of atoms involved in the superfluid motion, a change of the quantization constant l is statistically highly improbable, hence the superfluid will continue rotating for effectively infinite time. As opposed to the Hess-Fairbank effect, this is not an equilibrium configuration.

2.1.5 Quantized vortices

The appearance of quantized vortices is one of the most unusual features of superfluids [33]. In this section and hereinafter, we will often omit the word "quantized". Since quantized vortices are the only vortices discussed in this dissertation, this convention cannot cause any confusion. As remarked in the discussion before (2.50), the superfluid circulation can be non-zero if a singularity (a point in which the order parameter $\Psi(\mathbf{r})$ vanishes) exists in the liquid. In a 3D geometry, such singularities form lines that either terminate at the boundaries of the liquid, or close upon themselves. In the former case they are called vortex lines, while in the latter they are called vortex rings.

The order parameter around a vortex can be calculated using the time-independent GPE (2.32) [17]. Let us consider an infinite superfluid with a vortex line along the z-axis. In a loop around the z-axis, the phase changes by an integer multiple of 2π. We can then write the order parameter in cylindrical coordinates as

$$\Psi(\mathbf{r}) = f(r)e^{il\phi}. \tag{2.51}$$

If we assume translational symmetry along the z-axis, the function $\Psi(\mathbf{r})$ does not depend on the co-ordinate z. Inserting this form into (2.32), and setting the external potential to zero, we find

$$-\frac{\hbar^2}{2m^*}\frac{1}{r}\frac{\partial}{\partial r}\left(r\frac{\partial f}{\partial r}\right) + \frac{\hbar^2}{2m^* r^2}l^2 f + gf^3 = \mu f. \tag{2.52}$$

The radial derivative $\frac{\partial f}{\partial r}$ and the term proportional to $1/r^2$ can be neglected far from the vortex, hence the function $f(r)$ approaches the value

$$f(r)_{r\to\infty} = \sqrt{\mu/g} \equiv f_0 \tag{2.53}$$

We can transform (2.52) to a dimensionless equation by dividing r with the healing length ξ defined in (2.36), and f with f_0. The equation can be then solved numeri-

cally. The solution of a single-quantized vortex ($l = 1$) is, to a good approximation,

$$f(r) = f_0 \frac{r}{\sqrt{2\xi^2 + r^2}} \Rightarrow \Psi(r, \phi) = f_0 \frac{r}{\sqrt{2\xi^2 + r^2}} e^{i\phi}. \tag{2.54}$$

Let us now take a close look at the qualitative features of the solution (2.54). The order parameter vanishes on the z-axis ($r = 0$), namely along the vortex line. The phase ϕ is undefined along the z-axis, which constitutes therefore a line of singularities. The amplitude of the order parameter Ψ is perturbed in a cylindrical region or radius ξ around the vortex line defining a region called *vortex core*. The phase of Ψ, however, is perturbed everywhere in space. In a contour around the vortex line, the phase will always change by 2π even if the contour is infinitely far from the vortex core. These qualitative features are always present, even in a strongly-interacting superfluid like He II, where the GPE is not a valid approximation.

A vortex line is a metastable entity. The ground state of a superfluid clearly does not contain any vortices. However, as the phase is perturbed everywhere around a vortex line, the disappearance of a vortex from inside the bulk of the liquid is statistically highly improbable. A vortex can only vanish by reaching the boundary, or by annihilating with an anti-vortex of the opposite circulation.

The energy per unit length of a vortex line can be calculated by an appropriate integration of the solution (2.54). A simpler and more instructive approach [33] is to write the velocity field around the vortex line:

$$v(r) = \frac{\Gamma}{2\pi r}. \tag{2.55}$$

If we neglect the core of the vortex and assume that the liquid extends up to radius R, the kinetic energy associated with a single vortex is (per unit length)

$$K = \int_{\xi}^{R} \frac{1}{2} \rho_s \left(\frac{\Gamma}{2\pi r} \right)^2 2\pi r dr = \frac{\rho_s \Gamma^2}{4\pi} \ln \left(\frac{R}{\xi} \right). \tag{2.56}$$

In the above expression, Γ is the total circulation lh/m , $l = 0, \pm 1, \pm 2, ...$ In a 3D geometry, the total energy of the vortex line is proportional to its length, so it increases linearly with the system size. On the contrary, in a 2D geometry, the vortex energy increases logarithmically with the system size, therefore the excitation is energetically more favourable. The profound implications of this logarithmic functional dependence will be discussed in section 2.2.4.

Let us consider a multiply-quantized vortex ($|l| > 1$). Relation 2.56 predicts

that such a singularity will be unstable, and will eventually dissociate into multiple singly-quantized vortices. For example, the kinetic energy of a doubly-quantized vortex ($l = 2$) is four times the energy of a singly-quantized vortex. Thus, it is energetically preferable for the vortex to split into two singly-quantized vortices.

Vortices are important in superfluidity since they modify the flow properties of the liquid. We have seen that supercurrents can be supported in the geometry of Figure 2.3. Suppose now that it is possible for a vortex line to nucleate along the edge of the inner cylinder and move towards the outer cylinder where it annihilates or vice-versa. This process changes the circulation by one quantum, and is called *phase slip*. Therefore, movement of vortices inside the bulk of a superfluid can cause dissipation. For a review of the theory of quantized vortices in atomic gases, see [34, 35], and for a guide to all pertinent experiments see [36].

Vortex-Anti-Vortex pairs

Consider a system of one vortex and one anti-vortex line, and assume that the lines are straight and parallel to each other at distance x. Following 2.56, a good approximation for the energy of this system is

$$K = 2\int_{\xi}^{x} \frac{1}{2}\rho_s \left(\frac{\Gamma}{2\pi r}\right)^2 2\pi r dr = \frac{\rho_s \Gamma^2}{2\pi} \ln\left(\frac{x}{\xi}\right). \tag{2.57}$$

Therefore, the vortex and anti-vortex attract each other with a mutual force

$$F(x) = -\frac{dK}{dx} = -\frac{\rho_s \Gamma^2}{2\pi x}. \tag{2.58}$$

As this is a Coulomb law attraction, the problem of an ensemble of vortices and anti-vortices in a plane can be reduced to the problem of an ensemble of charges. This idea was employed by Kosterlitz and Thouless.

Around a vortex, there is a rotating superfluid flow. Thus, in a system of a vortex and anti-vortex, the flow around the vortex drags the anti-vortex and vice versa. In the absence of any other forces, the pair moves along the direction perpendicular to the line connecting the vortex and anti-vortex with velocity $v = \Gamma/2\pi x$. In the case of two vortices, on the other hand, the system rotates with angular velocity $\omega = \Gamma/\pi x^2$.

2.2 Two dimensional Bose gas

In this section we present the theory of the two-dimensional Bose gas. We are predominantly interested in the behaviour of the correlation function, which we calculate for the homogeneous non-interacting and interacting gas. We also discuss the trapped non-interacting gas case, in which there is a crossover to a BEC-like state. We follow the pedagogical approach of [37] and [38]. The reader is referred to [39] for a review of more sophisticated theories and [6] for a review of some relevant experiments.

2.2.1 Uniform non-interacting two-dimensional Bose gas

Consider a uniform non-interacting two-dimensional Bose gas. The density of states for periodic boundary conditions is the constant $mL^2/(2\pi^2)$, where m is the particle mass and L is the linear dimension of the system. The total particle number is

$$N = N_0 + \frac{m^* L^2}{2\pi\hbar^2} \int_{\epsilon_0}^{\infty} \frac{d\epsilon}{e^{(\epsilon-\mu)/(k_B T)} - 1}. \tag{2.59}$$

When μ approaches the lowest energy ϵ_0, the integral in (2.59) diverges. Therefore, the critical particle number N_c is infinite, so that always $N_0/N \ll 1$, and no BEC occurs.

We define the phase-space density $D \equiv n\lambda_T^2$, where n is the particle density, and λ_T is the thermal de Broglie wavelength $\lambda_T = h/\sqrt{2\pi m k_B T}$. In a semi-classical approach, λ_T is the extent of the wave-packet required to describe each particle at a temperature T. D is a dimensionless number, which is a measure of the inter-particle separation relative to λ_T. When $D \ll 1$, the inter-particle separation is much larger than λ_T, so the single-particle wave-packets do not overlap, and the gas can be considered classical. Such a gas is also called non-degenerate. On the contrary, when $D > 1$ (degenerate gas), the single-particle wave-packets overlap, and quantum effects arise. In the rest of this section, we use D as a free parameter, instead of the temperature T or density n. From (2.59), assuming $N_0 = 0$, $\epsilon_0 = 0$

$$D = \int_0^{\infty} \frac{dx}{\zeta^{-1} e^x - 1} = \int_0^{\infty} \frac{\zeta e^{-x}}{1 - \zeta e^{-x}} dx = -\ln(1-\zeta) \tag{2.60}$$

$$\mu = k_B T \ln\left(1 - e^{n\lambda_T}\right) \tag{2.61}$$

We now use (2.24) to calculate the off-diagonal part of the one-body density matrix

$n^{(1)}(s)$. The momentum distribution function $n(\hbar\mathbf{k})$ is related to the occupation numbers n_k by

$$n(\hbar\mathbf{k}) = \left(\frac{L}{2\pi\hbar}\right)^2 n_{\mathbf{k}}, \tag{2.62}$$

therefore

$$n^{(1)}(\mathbf{s}) = \frac{1}{(2\pi)^2}\int n_{\mathbf{k}} e^{i\mathbf{k}\mathbf{s}} d\mathbf{k} \tag{2.63}$$

For a non-degenerate gas ($D \ll 1$), (2.60) gives $\zeta \approx D$, and the momentum distribution approaches the Maxwell-Boltzmann distribution

$$n_k = n\lambda_T^2 e^{-k^2\lambda_T^2/4\pi}. \tag{2.64}$$

From (2.63), we only find short-range correlations and $n^{(1)}(s)$ assumes a Gaussian form

$$n^{(1)}(s) = ne^{-\pi s^2/\lambda_T^2}. \tag{2.65}$$

For a degenerate gas ($D > 1$), $\beta \ll 1$. The high-energy states $\beta\epsilon_k \gg 1$ continue to follow the Maxwell-Boltzmann distribution, and are responsible for the Gaussian decay of $n^{(1)}(s)$ (2.65) up to distances λ_T. For the low-energy states ($\beta\epsilon_k \ll 1 \Leftrightarrow k^2 \ll 4\pi/\lambda_T^2$) instead, we have

$$n_k = \frac{1}{\zeta e^{\epsilon_k/k_BT} - 1} \simeq \frac{k_BT}{\mu + \epsilon_k} = \frac{4\pi}{\lambda_T^2}\frac{1}{k^2 + k_c^2}, \tag{2.66}$$

where $k_c = \sqrt{2m|\mu|/\hbar}$. Therefore, for $s \gg \lambda_T$, $n^{(1)}(s)$ decays exponentially

$$n^{(1)} \simeq \frac{\sqrt{2\pi}}{\lambda_T^2}\frac{e^{-k_cs}}{\sqrt{k_cs}}, \quad k_c^{-1} = \lambda_T e^{n\lambda_T^2/2}/\sqrt{4\pi}. \tag{2.67}$$

2.2.2 Uniform interacting two-dimensional Bose gas

Our derivation of the Gross-Pitaevskii equation in (2.32) depends on the interaction parameter g. We argued that this relation is valid only when the interaction is weak. The exact meaning of "weak interaction" depends on the system dimensionality. In a 2D geometry, for instance, we can define a dimensionless coupling constant $\tilde{g}$ as below

$$g = \frac{\hbar^2}{m^*}\tilde{g}. \tag{2.68}$$

We can gain some insight on the physical meaning of $\tilde{g}$ from the definition of the healing length in (2.36)

$$\xi = \frac{\hbar}{\sqrt{2m^* ng}} = \frac{1}{\sqrt{2\tilde{g}n}}. \tag{2.69}$$

In the ensuing discussion we argued that ξ is a length-scale over which obstacles are screened from the bulk of the condensate. If interactions are strong, screening is effective, and ξ is small. From (2.69), we see that the coupling constant $\tilde{g}$ determines the ratio of ξ over the inter-particle distance $1/\sqrt{n}$.

The values of $\tilde{g}$ for which the interaction energy of N particles is much smaller than the kinetic energy of N non-interacting particles equally distributed over the N lowest available states define the weak interaction limit. From that viewpoint, the weak interaction limit is

$$\tilde{g} \ll 2\pi. \tag{2.70}$$

At zero temperature, a weakly interacting gas is condensed and can be described by an order parameter $\Psi(\mathbf{r}) = n(\mathbf{r})e^{i\phi(\mathbf{r})}$. At non-zero temperature, both the amplitude $n(\mathbf{r})$ and phase $\phi(\mathbf{r})$ of $\Psi(\mathbf{r})$ exhibit thermal fluctuations. When the mean-field interaction energy gn is much larger than the thermal energy $k_B T$, or equivalently when the phase-space density $D \gg 2\pi/\tilde{g}$, amplitude fluctuations are suppressed. The interaction energy is then a constant, and the only important contribution to the system energy is the kinetic energy of the superfluid component

$$H = \int \frac{1}{2} m^* n_s |\mathbf{v}_s|^2 d\mathbf{r} = \frac{\hbar^2}{2m^*} n_s \int [\nabla\phi(\mathbf{r})]^2 d\mathbf{r}, \tag{2.71}$$

where we have used (2.47) for the superfluid velocity $\mathbf{v}_s$. Density fluctuations with a characteristic length-scale of ξ are totally neglected in the Hamiltonian (2.71). The expression also neglects higher energy modes, involving both density and phase fluctuations. These modes contribute to the off-diagonal part in the one-particle density matrix $n_{(1)}(\mathbf{r})$ at distances $r \leq \lambda_T$. Hence, (2.71) describes long-range interactions for distances $r \gg \xi, \lambda$.

We can then expand $\phi(\mathbf{r})$ in a Fourier series, assuming that each mode is thermally occupied. Hence, we obtain:

$$n^{(1)}(r) = \langle \Psi^*(\mathbf{r})\Psi(0)\rangle = n_s \left\langle e^{i[\phi(\mathbf{r})-\phi(0)]} \right\rangle. \tag{2.72}$$

This calculation makes use of the identity

$\langle \exp(iu)\rangle = \exp(-\langle u\rangle^2/2)$ for a random variable u with Gaussian distribu-

tion. The final result is a power law decay [37]

$$n^{(1)}(\mathbf{r}) = n_s \left(\frac{\xi}{r}\right)^{1/(n_s\lambda_T^2)}. \tag{2.73}$$

This expression suggests that $n^{(1)}(r)$ decays to zero even in infinitesimally small temperatures, as the distance r grows to infinity. Consequently, no long range order of the type we defined in (2.26) can be established.

We have proven (2.73) in the limit $D \to \infty$. From the above discussion, it is not clear for which values exactly of the phase-space density Hamiltonian(2.71) is valid, and therefore when we expect the power law decay (2.73). Also, result (2.73) only proves that there can be no conventional long range order in the interacting Bose gas, but it leaves the question of whether there is another phase transition open. To find out the answers to these questions, we also need to take into account vortex excitations, which, as it turns out, dominate the thermodynamics at low temperature.

2.2.3 The Hohenberg-Mermin-Wagner theorem

The density of single particle states (2.8) in a d dimensional system is proportional to $\epsilon^{d/2-1}$. Therefore, decreasing d leads to an increase in the density of states at low energies relative to that at higher energies. Consequently, if $d < 2$, the chemical potential remains sufficiently negative such that there is never macroscopic occupancy of the lowest state in the limit of a large particle numbers [40]. In a 2D system, the number of particles is given by the expression:

$$N = \sum_i \frac{1}{e^{(\epsilon_i-\mu)/k_BT} - 1}. \tag{2.74}$$

The sum can be replaced by an integral yielding the chemical potential:

$$\mu = k_BT \ln(1 - e^{-T_c/T}) = k_BT \ln(1 - e^{-\eta}). \tag{2.75}$$

The introduction of η at this point is illegitimate. The critical temperature at which quantum degeneracy manifests itself is:

$$T_c = \frac{2\pi\hbar^2 n_{2D}}{m k_B}, \tag{2.76}$$

where $n_{2D} = N/A$ is the number of particles per unit area.

Unlike the three-dimensional case, the lowest state warrants special treatment if $|\mu| \gg \hbar^2/mA$ since under these conditions the occupancy of the lowest level for $T \lesssim T_c$ is $N_0 \simeq k_B T/|\mu| \simeq e^{T_c/T}$. This becomes of the order of the total number of particles, N, only if $T \lesssim T_c/\ln(N)$ which is vanishingly small in the thermodynamic limit $N \to \infty$, $A \to \infty$, for $N/A \to$ constant. Therefore, the Hohenberg-Mermin-Wagner theorem tells that at any temperature different than zero, BEC for a uniform 2D system (2.26) cannot occur in the large system limit [40].

2.2.4 The Kosterlitz-Thouless transition

In the previous section, we saw that no conventional long range order can be established in an interacting Bose gas, since the correlation function $n^{(1)}(r)$ decays to zero as $r \to \infty$ at non-zero temperatures. Yet this result does not preclude the existence of a state with superfluid properties. In 1972, Kosterlitz and Thouless developed an elegant theory exploring the role of quantized vortices [41, 42]. The phase transition they discovered is now termed Kosterlitz-Thouless phase transition (KT transition), or Berezinskii-Kosterlitz-Thouless (BKT) phase transition after Berezinskii who proposed similar arguments close to that time [8, 43].

At low enough temperatures, the correlation function $n^{(1)}(r)$ decays slowly allowing for the superfluid properties to be locally observed. In particular, let us consider a contour which is small enough, so that the superfluid phase can be defined quasi-uniformly. The phase ϕ can only change by a multiple of 2π along the contour. A superfluid current will flow if $\Delta\phi = 0$, which decays when $\Delta\phi$ changes by 2π. This change can happen only when a quantized vortex moves across the contour, which is possible when free vortices are present in the system. We conclude that a state with free vortices is non-superfluid. On the other hand, vortices and anti-vortices assemble in clusters of zero total vorticity at very low temperatures. The total phase change $\Delta\phi$ remains constant and the super-currents do not dissipate when one cluster moves across the contour. This is the crux of the BKT transition. The following expression provides a first estimate of the BKT transition temperature

$$k_B T_{\mathrm{BKT}} = \frac{\pi \hbar^2 n_s}{2m^*}. \tag{2.77}$$

When $T < T_{\mathrm{BKT}}$ free vortices are not energetically permitted, whereas higher temperatures $T > T_{\mathrm{BKT}}$ favour the proliferation of free vortices. The BKT critical temperature (2.77) depends on the superfluid density n_s, which is not given a priori. Hemce, this equation is not useful for the computation of the critical temperature

with the system parameters given beforehand. However, an interesting result can be obtained from the alternative form

$$n_s \lambda_{T_{\rm BKT}}^2 = 4, \tag{2.78}$$

where $\lambda_{T_{\rm BKT}}$ is the de Broglie wavelength at the critical temperature. Since n_s can only increase with increasing temperature, we infer that n_s cannot have any value smaller than $4/\lambda_T^2$ in the superfluid phase. Of course, $n_s = 0$ in the normal (non-superfluid) phase. Indeed, Nelson and Kosterlitz predicted [44] that the BKT transition is of first order, since the superfluid density n_s exhibits a discontinuous jump when the transition temperature is crossed. Another consequence of (2.78) is that the exponent in the power law decay (2.73) is always smaller than 1/4.

In (2.58), we showed that vortices of opposite sign exert attractive Coulomb-like forces to each other. A similar energy argumentation can be employed to demonstrate that vortices of the same sign repel each other following the same law. Therefore, the problem of a 2D superfluid with an ensemble of vortices can be directly mapped to the problem of charged rods moving in the plane perpendicular to their axis [41]. The unbinding of vortices in the superfluid corresponds formally to the divergence of polarizability in the charged rod problem. More specifically, a small electric field is able to separate a positively-charged from a negatively-charged rod at infinite distance. Using the pair energy, the mean square separation between pairs due to thermal fluctuations can be written as

$$\left\langle r^2 \right\rangle = \frac{\int_\xi^\infty r^2 e^{-K/k_BT} 2\pi r\, dr}{\int_\xi^\infty e^{-K/k_BT} 2\pi r dr} = \frac{\xi^2}{2} \frac{k_BT - 2\frac{\pi\hbar^2 n_s}{2m^*}}{k_BT - \frac{\pi\hbar^2 n_s}{2m^*}}, \quad \text{for} \quad T < \frac{\pi\hbar^2 n_s}{2m^*}. \tag{2.79}$$

As we observe, the polarizability diverges indeed at the transition temperature (2.77).

For a more comprehensive treatment, we need to consider how the interaction between vortices is influenced by the presence of other pairs. Namely, the interaction between vortices at long distances is screened due to pairs of small size. This effect can be quantified via a distance-dependent dielectric constant in the Coulomb law, when considering the problem of charged rods. The energy of a rod dipole is

$$U = \int_\xi^\infty \frac{q^2}{4\pi\epsilon(r)}\, dr - qEr\cos\theta. \tag{2.80}$$

In the above expression, E is the externally applied electric field, q is the charge of each rod, and θ is the angle between the dipole and the electric field direction. The

polarizability of the pair can be subsequently calculated as

$$p(r) \equiv q \frac{\partial}{\partial E} \langle r \cos\theta \rangle \,. \tag{2.81}$$

The energy of large pairs (the charges at long distance) is affected by the polarization of small pairs (the charges at short distance). Here, in order to calculate the long-distance response, we must account self-consistently for the short-distance behaviour. The calculation [41] improves the estimate of the transition temperature $T_{\rm BKT}$. As we approach $T_{\rm BKT}$ from below, the dielectric function at large distances diverges:

$$\epsilon(r \to \infty)|_{T \to T_{\rm BKT}^-} \to \infty \tag{2.82}$$

As we increase T further above $T_{T_{\rm BKT}}$, the function diverges for progressively shorter distances r. The physical implication of this behaviour is that pairs of infinite size dissociate first, and as the temperature is further increased, pairs of smaller size unbind as well.

As we have discussed, relation (2.78) is not suitable for calculating the transition temperature for some given system parameters. In particular, it does not predict any dependence of $T_{\rm BKT}$ on the inter-particle interaction. Microscopic theories provide the following result for the critical phase-space density [39, 45–47]

$$D_{\rm BKT} = n\lambda^2_{T_{BKT}} = ln\left(\frac{C}{\tilde{g}}\right), \quad C = 380 \pm 3 \tag{2.83}$$

The Kosterlitz-Thouless theory does not depend on the microscopic details of the system under consideration. As far as the geometry is two-dimensional and the order parameter can be described by an in-plane vector, the same arguments hold [48] and the theory can be regarded as universal. The local order parameter in a superfluid is the corresponding wavefunction $\Psi(\mathbf{r}) = n_s(r)\exp[i\phi(r)]$, but since at low temperatures the amplitude fluctuations are frozen, the superfluid can be described exclusively by its phase $\phi(\mathbf{r})$ and the constant amplitude n_s. The phase $\phi(\mathbf{r})$ defines indeed an in-plane vector. The 2D XY model consists of a spin lattice, where spins are allowed to move only on the lattice plane. Hence, every lattice cite is characterized by the angle $\phi(\mathbf{R})$ of its spin. A 2D crystal can be described by the displacement vector of the atom at each lattice cite. In all the above cases, when interactions are included, the low-energy Hamiltonian is of the form (2.71), and vortex dislocations are stable at low temperature.

The KT theory has been studied experimentally in 4_{He} thin films [49, 50], Josephson junction arrays [51, 52], atomic hydrogen [53], and more recently in 2D atomic gases [54–57]. Although several of the thoeretical predictions could be tested, in none of these experiments was it possible to directly measure the correlation function $n^{(1)}(r)$. In Chapter 4, we present a our theoretical results where we numerically calculated the normalized correlation function $g^{(1)}(r)$ in a microcavity exciton polariton condensate. Although the theory developed in the current chapter cannot be applied directly to such non-equilibrium systems, it can still serve as a guide to understand the experimental data, and to point out the features arising from non-equilibrium dynamics.

Chapter 3

Microcavity exciton-polaritons

In the previous chapter we have introduced different concepts concerning Bose-gases as well as some relevant phenomena related to them, as BEC, BKT-phase transition and superfluidity. This chapter is devoted to the physics of a particular Bose-quasiparticle, the microcavity polaritons. The chapters is starting with an introduction to the concept of exciton in the bulk and in semiconductor devices. Then, it follows a description of the phenomenology of the interaction between cavity photons and quantum well excitons, which leads to the appearance of a new type of bosonic quasi-particle, the polariton. There are different ways in which polaritons can be created and, in the final part of this chapter, we study the creation of polaritons by coherently pumping. This scheme for creating polaritons, which is one the best for studying the spontaneous onset of macroscopic coherence in planar microcavity systems, is the so-called optical parametric oscillation (OPO) regime.

3.1 Excitons and polaritons, an historic overview

Quasiparticles are elementary particle-type excitations present in a vast number of different condensed matter system. Particularly, quasiparticle may present integer spin and, consequently, they may obey Bose-statistic. Therefore, bose-quasiparticle can condense and show all the rich phenomena described in the previous chapter.

This is the case of excitons, which are the bound pairs of electrons and holes, both half-integer particles, in semiconductors. Due to the bosonic nature of excitons, physicists began to speculate about their condensation in the early studies of excitons, in the 1960's. Thus, we find proposals for bulk semiconductors excitons [58–61], However, the short lifetime of these optically generated excitons has raised

a big barrier to observe their condensation [62, 63]. Later on, other schemes for observing excitons and their condensation were described, such as excitons appearing in quantum wells [64–66]. Due to the spatial separation between the electron and the hole, the exciton present a lifetime much longer than the earlier optically generated excitons.

From the earliest studies of excitons, physicists realized that the strong interaction between excitons and light has important and drastic consequences on the different physical properties both of the excitons and light, as for example, their exciton spectrum [67]. The strong coupling regime of the excitons with the photons is characterized by strong non-linear interactions that can lead to important collective behaviour. In this strong coupling-regime, the photon dressed with a cloud of excitons can be described as a new quasiparticle, the *polariton* [68, 69]. We mention that polaritons can appear in other scenarios, where light interact strongly with matter.

The study of polaritons in bulk semiconductors present different limitations to deal with. We particularly stress that the spectrum of the polaritons in three-dimensions is not bounded by below since there is no bulk photon with zero momentum and the polaritons were not present inside the luminescence cone. However, these limitations have been overcome from the 1990s by considering the strong interaction of excitons with cavity photons in heterostructures in reduced dimensions. In such scenarios, the cavity photons exhibit a non-zero effective mass since the spatial confinement by planar mirrors. Thus, polaritons were created in zero-spatial dimensions (quantum dots), one-spatial dimensions (quantum-wires) and two-spatial dimensions (quantum-wells).

Specially, we mention the work done by Weisbuch et al., [70], were is was shown the emergence of two-dimensional polaritons in a quantum wells, or microcavity-polaritons. The dispositive, which was a vertical-cavity surface-emitting laser (VCSEL) consisted on different quantum wells placed between two parallel planar distributed Bragg reflector (DBR).

This type of dispositives allows to explore a vast number of different interesting collective phenomena since the degree of control and tunability of different parameters of the system. Moreover, since the life-time of the polaritons is much shorter than the life-time of the excitons, the quantum state of the polaritons can be reconstructed from the emitted photons of the VCSEL, through their photoluminescence. This provides a direct study of a collective many-body quantum system with the well-developed tools in optical setups.

3.2 Excitons

As we already introduced in the previous section, an exciton is the bound electron-hole pair in semiconductors. Thus, at low densities, exciton are hydrogen-like bosonic particles with two important characteristic. First, the Bohr radius is large because excitons present a really small reduced mass ($\approx m_e/20$) and, secondly, their binding energy energy is small since the Coulomb interaction is significantly reduced by the dielectric constant presents in the semiconductor. The first of the first characteristic makes the excitons a suitable physical system for observing the condensation at high temperatures, i.e. order of 1 K. The comparison of excitons to hydrogens are shown in the Table 3.1. Excitons also form in an organic semiconductors where Coulumbic

	Excitons	Hydrogen
reduced mass	$\sim 0.058m_e$	$\sim 1.0m_e$
Bohr radius	$\sim 12nm$	$\sim 0.053nm$
binding energy	$\sim 5.0meV$	$\sim 13.6eV$

Table 3.1: Comparison between GaAs exciton parameters in the reduced mass approximation and those of the Hydrogen atom.

interactions are stronger than inorganic semiconductors due its the dielectric constant therefore excitons are tightly bound which result atomic scale object, Frenkel excitons.

3.2.1 Bulk semiconductor excitons

Schematics of an typical direct gap semiconductor band structure is shown in Figure. 3.1, where the locale minima of conducting and maximum of valence band are exactly at same momenta, consists of a filled conduction electron band separated from an empty valence electron band through a well defined gap E_{gap}. The absorption of a photon with energy close to the semiconductor gap can promoted an electron from the conduction to the valence band. The electron and hole appearing in the system , located at the valence and conduction band respectively, may created a bound state, the *exciton*, by minimizing their Coulomb attraction. As we already mentioned, in some semiconductor materials like *GaAs*, the binding energy of such a pair is small compare to the usual one between electrons, since the Coulomb interaction is screened by the valence electrons. These excitons are extended over many lattice spacings, which is one of the principal characteristic of the so-called Wannier-Mott

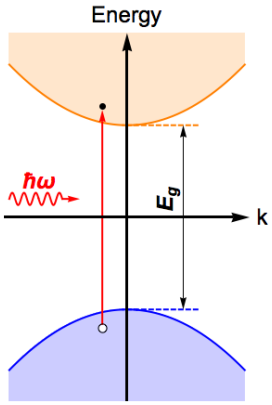

Figure 3.1: Schematics of an idealised bandstructure for a direct gap semiconductor which consist of a completely filled valence band (blue) and an empty conduction band (orange). The electron excitations in the direct gap semiconductors illustrated by the arrow, in the absence of electron-electron in teractions, where an electron is exciting from the valence band to the conduction band, leaving a positively charged hole in the valence band.

excitons, their dynamics can be described with the following effective Hamiltonian:

$$\hat{H}_{\mathrm{X}} = \frac{\mathbf{p}_h^2}{2m_h^*} + \frac{\mathbf{p}_e^2}{2m_e^*} - \frac{e^2}{4\pi\epsilon^*|\mathbf{r}_h - \mathbf{r}_e|}. \tag{3.1}$$

We observe that the electron and hole present effective masses m_e^* and m_h^* respectively, which are considered to be isotropic and with values given by the specific form of the conduction and valence dispersion relations. We observe also the effective dielectric constant ϵ^*, which considers the screening of the interaction with by the rest of the electron at the conduction band. As usual, we can calculated the effective mass m_X of the exciton with the relation $1/m_X = 1/m_e^* + m_h^*$; which, as we alredy mentioned, can be 20 times smaller than the electron mass for usual experimental setups. The eigenvalues of the Hamiltonian (3.1) can be obtained following the same techniques than in the hydrogem atom case. Then, the dispersion relation for the excitons reads as:

$$E_X(\mathbf{q}) = E_{\mathrm{gap}} - \frac{E_{Ry}}{n_X^2} + \frac{\hbar^2 q^2}{2m_X}, \tag{3.2}$$

where E_{gap} is the gap of the semiconductor, E_{Ry} is the excitonic Rydberg of binding for excitons and $n_X = 1, 2, ...$ is the principal quantum number. Therefore, we have a physical illustration about excitons in semiconductors which is shown in the Figure (3.2)

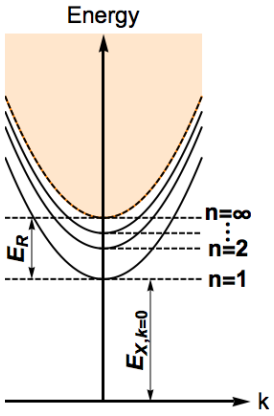

Figure 3.2: Cartoon of a hydrogen like discretized energy bands of excitons in a direct gap semiconductor given by equation (3.2). The most upper dashed line is the energy level of $E(\infty)$, is the minimum energy of the continuum state -upper bound of discrete energy level and which is equal to band gap E_g.

3.2.2 Quantum well excitons

As we already mentioned in the introduction of the current chapter, the consideration of the excitons in confined structures overcomes some of the obstacles presented in considering excitons in bulk semiconductors.

Particularly, this is the case of the two-dimensional quantum wells (QW). A QW is thin layered semiconductor sandwiched between other two semiconductor "barrier" layers of wider bandgap material (see Figure 3.3). In such plataforms, the energy levels of the excitons are quantized. Current advances in material growth techniques, specifically of molecular beam epitaxy, allow to obtain QW with thickness comparable to the exciton Bohr radius. In such cases, the dynamics of the excitons is confined to the QW plane. At first considered by Lozovik, Yudson and Shevchenko [64–66] the lifetime of the exciton can be significantly increased by confining electron and holes in separated two-dimensional layers, i.e. by considering the implementation of coupled quantum wells (see Figure 3.3). Indirect excitons, namely the ones formed in coupled quantum wells, exhibit more favourable properties towards condensation, as the strong dipole interaction between them, which prevents from the formation of excitations and stabilizes the system. Thus, a substantial effort has been done towards the study, characteritzation and control of indirect excitons [71].

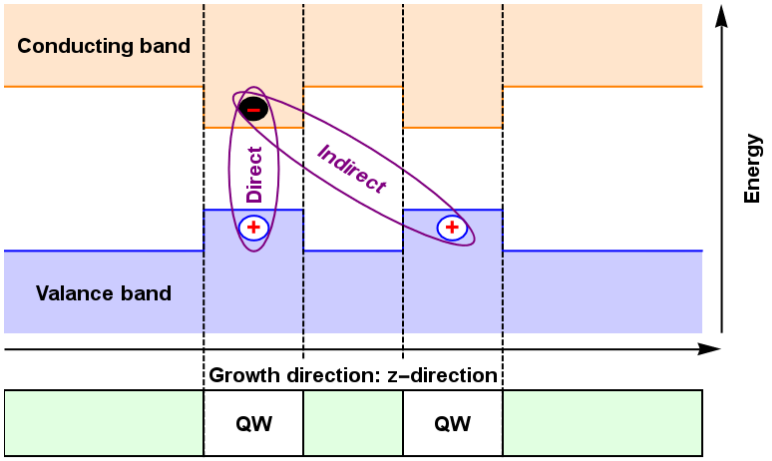

Figure 3.3: Scheme of excitons in coupled quantum wells. Coulombic electron and hole bound in the same wells are called direct excitons while if excitons are formed from electrons and holes located in different wells known as indirect excitons.

3.2.3 Quamtum well excitons coupling with light

The interaction between the QW excitons and the cavity photons conserves the total energy and the total in-plane momentum. Moreover, this coupling also conserves the total angular-momentum. Electron can have spin projection $\pm 1/2$ along the growth axis z, whereas the holes in the valence band present spin projection $\pm 3/2$ in such a direction. Therefore, the projection of the spin of the excitons in the z direction can take the values $\pm 1, \pm 2$. The ± 2 excitons are optically inactive, they do not couple to light since in this process angular momentum won't conserved, they are called dark excitons. Whereas the ± 1 excitons, the bright excitons, can couple to ± 1 polarized light, leading to polaritons.

3.3 Semiconductor microcavity

As introduced at the beginning of the chapter, the strong interaction between quantum well excitons and microcavity photons leads to the emergence of the microcavity-polaritons, for simplicity called polaritons hereinafter.

Optical cavities with micrometer dimensions, i.e. optical microcavities, have attracted much research attention for their role in integrated optical circuits. Microcavities are used for various applications, including the development of non-linear devices. Due to the current high degree of development in fabrication techniques,

microcavities with several geometries including photonic crystal resonators, microspheres are currently considered so far for a vast range of applications.

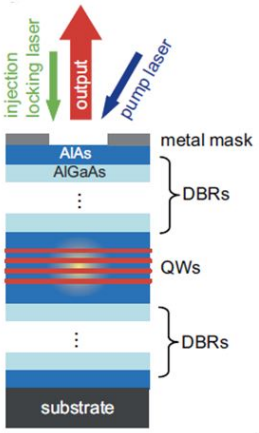

Figure 3.4: Semiconductor microcavities are nanostructures that consist of a planar Fabry-Perot cavity with one or more embedded quantum structures (wells, wires, dots etc), sandwiched between two Bragg mirrors.

Specifically in this thesis we are considering planar microcavities composed of two DBR which are placed face to face, forming a Fabry-Perot resonator. The DBR is a structure composed of multiple alternating layers of different materials, typically two, with different refractive index. The thickness of every layer is matched to be $\lambda_0/4$, where λ_0 is the desired reflected wavelength. Then, the reflected waves interfere constructively and, therefore, the transmission is forbidden in the perpendicular direction of the layers. Thus, there is a photonic band gap centered at λ_0.

Inside the microcavity, only the modes allowed for the DBR are transmitted through the resonator. This modes are confined in the z-direction, which is the perpendicular one to the DBR layers and they can oscillate free in the in-plane directions. Therefore, the resonator acts as a effective 2D-system.

The finite photon lifetime τ_C of the cavity is proportional to the quality factor Q of the mirror of the cavity:

$$\tau_C \sim Q \sim \frac{1}{\kappa_C}, \tag{3.3}$$

where κ_C is the width of the cavity mode, which is proportional to the photon scape rate. We mention that the κ_C can depend on the position due to the variations of the thickness of the DBR and cavity space [72].

The planar microcavity gives an non-zero effective mass for the cavity photon, which a crucial requirement for observing collective many-body quantum phenom-

ena in polaritons fluids [73]. The z-component of the optical modes allowed in the microcavity satisfy $k_z = N\pi/l_D$, where n is an integer number and l_D is the thickness of the spacer medium. Therefore, the dispersion relation for the cavity photons reads as:

$$E_C(k_\parallel) = \frac{\hbar c}{n_0}\sqrt{k_z^2 + k_\parallel^2} \simeq \frac{\hbar c}{n_0}k_z\left(1 + \frac{k_\parallel^2}{2k_z^2}\right) = \frac{\hbar c}{n_0}k_z + \frac{\hbar^2}{2m_C}k_\parallel^2, \tag{3.4}$$

where $n_0$is the refractive index of the spacer medium and we have expanded the $E_C(k_\parallel)$ for low momenta $k_\parallel$, obtaining a non-zero effective mass for the cavity photon:

$$m_C = \frac{\hbar k_z n_0}{c}. \tag{3.5}$$

3.4 Microcavity-polaritons

3.4.1 From exciton-photons to lower-upper polaritons

As we already introduced in Section 3.1, the strong coupling regime between the cavity photons and the excitons of the QWs embedded at the cavity spacer leads to the emergence of a bosonic quasi-particle, the polariton. Following the energy and momentum conservation at the in-plane betweent the excitons and the photons, we can describe the exciton-photon system as a system of two coupled oscillators [74]. Then, the Hamiltonian $\hat{H}_0$ for such a 2D system takes the form:

$$\hat{H}_0 = \sum_{\mathbf{k}}\left[\omega_C(\mathbf{k})\hat{a}_C^\dagger(\mathbf{k})\hat{a}_C(\mathbf{k}) + \omega_X(\mathbf{k})\hat{a}_X^\dagger(\mathbf{k})\hat{a}_X(\mathbf{k}) + \frac{\hbar\Omega_R}{2}\left(\hat{a}_C^\dagger(\mathbf{k})\hat{a}_X(\mathbf{k}) + \text{H.c.}\right)\right], \tag{3.6}$$

where $\mathbf{k} = (k_x, k_y) = k_\parallel$ is the in-plane momentum, $\hat{a}_C^\dagger, \hat{a}_C$ are the creation and annihilation operators respectively for the cavity photon-mode , $\hat{a}_X^\dagger, \hat{a}_X$ are the creation and annihilation operators respectively for the exciton mode and $\hbar\Omega_R/2$ is Rabi-coupling between photons and excitons and ω_C, ω_X are the dispersion relation for the photons and excitons respectively.

Then, we can express Hamiltonian (3.6) as:

$$\hat{H}_0 = \sum_{\mathbf{k}}\begin{pmatrix}\omega_X(\mathbf{k}) & \frac{\hbar\Omega_R}{2} \\ \frac{\hbar\Omega_R}{2} & \omega_C(\mathbf{k})\end{pmatrix}, \tag{3.7}$$

which can be diagonalize, obtaining the normal modes of the system, i.e. the *polaritons*:

$$\hat{H}_0(\mathbf{k}) = \sum_{\mathbf{k}} \left[\omega_{LP}(\mathbf{k}) \hat{a}^\dagger_{\mathbf{k}} \hat{a}_{\mathbf{k}} + \omega_{UP}(\mathbf{k}) \hat{b}^\dagger_{\mathbf{k}} \hat{b}_{\mathbf{k}} \right], \tag{3.8}$$

where $\hat{a}^\dagger, \hat{a}$ are the creation-annihilation operators for the *lower polaritons* and $\hat{b}^\dagger, \hat{b}$ are the creation-annihilation operators for the *upper polaritons*. The dispersion relations for such polaritons modes read as:

$$\omega_{LP}(\mathbf{k}) = \frac{1}{2}\left(\omega_X(\mathbf{k}) + \omega_C(\mathbf{k}) - \sqrt{(\omega_X(\mathbf{k}) - \omega_C(\mathbf{k}))^2 + (\hbar\Omega)^2} \right), \tag{3.9}$$

$$\omega_{UP}(\mathbf{k}) = \frac{1}{2}\left(\omega_X(\mathbf{k}) + \omega_C(\mathbf{k}) + \sqrt{(\omega_X(\mathbf{k}) - \omega_C(\mathbf{k}))^2 + (\hbar\Omega)^2} \right). \tag{3.10}$$

The exciton mass is much larger than the effective mass of the photon (typical values for them are $m_X \approx 0.05 m_e$ and $m_C \sim 10^{-5} m_e$), then, the dispersion relation of the exciton appears to be constant for the considered momenta $\mathbf{k}$:

$$\omega_X(\mathbf{k}) = \omega_X(0) + \frac{\hbar^2 \mathbf{k}^2}{2m_X} \approx \omega_X(0), \tag{3.11}$$

$$\omega_C(\mathbf{k}) = \omega_C(0) + \frac{\hbar^2 \mathbf{k}^2}{2m_C}, \tag{3.12}$$

$$\tag{3.13}$$

Then, the dispersion relation of the polariton (3.10) become:

$$\omega_{LP}(\mathbf{k}) = \frac{1}{2}\left(\frac{\hbar^2 \mathbf{k}^2}{2m_C} + \delta - \sqrt{\left(\frac{\hbar^2 \mathbf{k}^2}{2m_C} + \delta \right)^2 + (\hbar\Omega)^2} \right), \tag{3.14}$$

$$\omega_{UP}(\mathbf{k}) = \frac{1}{2}\left(\frac{\hbar^2 \mathbf{k}^2}{2m_C} + \delta + \sqrt{\left(\frac{\hbar^2 \mathbf{k}^2}{2m_C} + \delta \right)^2 + (\hbar\Omega)^2} \right), \tag{3.15}$$

where $\delta \equiv \omega_C(0) - \omega_X(0)$ is the detuning between the photons and the excitons and we have considered $\omega_X(0) = 0$. As an example, these dispersion relations are displayed at Fig. 3.5 for $\delta = 0$.

The detuning between the upper and lower polaritons for $\delta = 0$ at $\mathbf{k} = 0$ is given by the Rabi splitting $\hbar\Omega_R$, which was mesured first by Weisbuch et al. [**?**]

by studying the variation of the dispersion relation of the cavity photons along the microcavity. Photoluminescence measurements through angle-resolved techniques permit to mesure the dispersion relation of the polaritons, since the polariton momentum $\mathbf{k}$ is related to the cavity photon emission angle θ_{out} by $\mathbf{k} \sim \sin\theta_{\text{out}}$. As a pionner study with angle-resolved techniques we mention the work done by Houdre el al [75]

3.4.2 Hopfield coefficients and polariton effective masses

The matrix U for the change of basis between the exciton-photon basis to the lower-upper polariton basis takes the form:

$$\begin{pmatrix} \hat{a} \\ \hat{b} \end{pmatrix} = \begin{pmatrix} -C(\mathbf{k}) & X(\mathbf{k}) \\ X(\mathbf{k}) & C(\mathbf{k}) \end{pmatrix} \begin{pmatrix} \hat{a}_X(\mathbf{k}) \\ \hat{a}_C(\mathbf{k}) \end{pmatrix}, \tag{3.16}$$

where the $C(\mathbf{k}), X(\mathbf{k})$ are the Hopfield coefficients [1, 68**?**] which obey:

$$C(\mathbf{k})^2 + X(\mathbf{k})^2 = 1; \tag{3.17}$$

Specifically, $X(\mathbf{k})^2 = C(\mathbf{k})^2 = 1/2$.

The effective masses for the polaritons can be extracted from the parabolic approximation of the dispersion relations (3.15) at low momentum and considering a flat dispersion relation for the excitons:

$$m_{LP} = \frac{m_C^*}{C^2(0)}, \tag{3.18}$$

$$m_{UP} = \frac{m_C^*}{X^2(0)}. \tag{3.19}$$

If we consider typical values for inorganic cavities, as $GaAs$, for $\delta = 0$ we obtain that $m_{LP} \sim 10^{-5} m_e$. Thus, polaritons may provide suitable scenarios for observing condensation at reasonable high temperatures.

3.4.3 Strong and weak coupling regimes

As the different photon-matter system, the exciton-photon system exhibit two different regimes, namely weak-cupling and strong-coupling regimes (SC). In this thesis we are interested in the second one. In both regimes, excitons with a in-plane mo-

mentum $\mathbf{k}$ couple to a cavity photon with the same in-plane momentum, due to the momentum conservation at the xy-plane. At the SC regime, Rabi oscillations between the excitons and the cavity photons can occur provided that the characteristic time of this process is much faster than the decay of the excitons and the photons:

$$\frac{1}{\hbar\Omega_R} \ll \tau_X, \tau_C \quad \rightarrow \quad \hbar\Omega_R \gg \kappa_X, \kappa_C. \tag{3.20}$$

Then, in order to observe the SC regime, it is required to have cavities with a low rates of loses. Also the Rabi coupling is another crucial parameter, which reads as:

$$\Omega_R \propto \sqrt{\frac{f_{\text{osc}} N_{QW}}{l_D}}, \tag{3.21}$$

where f_{osc} is the QW oscillator strength for the excitons, l_D is the cavity lenght and N_{QW} is the number of QW. We mention that Ω_R is also proportional to the overlap between the wave-fucntion of the exciton and the cavity photons.

3.4.4 Exciton-exciton interactions and non-linearity in polaritons

There are two different main sources of non-linearities in the polariton system. The first is *saturation*, where there is a bleanching of Ω_R due to a screening of the oscillator strength f_{osc} (see Eq. (3.21)). This non-linear effect appears at really high exciton densities n_X, for example, at $n_X \propto 10^{11}$ cm^2 for typical non-organic cavities [76, 77].

The second source of non-linearity for polariton systems comes from the exciton-exciton interaction due to the elastic Coulomb scattering process. The Hamiltonian $\hat{H}_{XX}$ describing such interaction for initial momenta $\mathbf{k}_1$ and $\mathbf{k}_1$ reads as:

$$\hat{H}_{XX} = \frac{1}{2} \sum_{\mathbf{k},\mathbf{k}_1,\mathbf{k}_2} V_{XX}(\mathbf{q}, \mathbf{k}_1, \mathbf{k}_2) \hat{a}_X^\dagger(\mathbf{k}_1 + \mathbf{k}_1 - \mathbf{k}) \hat{a}_X^\dagger(\mathbf{k}) \hat{a}_X(\mathbf{k}_1) \hat{a}_X(\mathbf{k}_2), \tag{3.22}$$

where V_{XX} is the effective interaction potential. As a consequence of these interaction, the polariton energy shows a blue-shift.

As a consequence of these two different sources of non-linearities, the dynamical equations of the lower polariton field show repulsive interaction between co-circularly polarized lower polaritons.

3.5 Incoherent and Coherent pumping schemes

The polariton system is a intrinsically non-equilibrium system since the polaritons show a finite-life time due to the losses rate of the cavity photons and the excitons at the microcavity. Therefore, it is required a continuous injection of polaritons from an external source into the system to balance this losses.

There are fundamentally two different schemes for injecting polaritons into the system. The first one is called *incoherent pump* or *non-resonant scheme*. It consists of an incoherent injection of hot carriers, which eventually, through a complicated process which also involves phonon-exciton interaction [1] leads to the emergence of a macroscopic occupation of the low momentum lower polariton states. Different phenomenological models combining pumping and relaxation have been formulated for describing the dynamics of the polariton field emerging from the incoherent pump.

The second scheme for injecting polaritons into the system is the *resonant* or *coherent pump*. In that case, the external laser field is chosen in such a way that coherently injects photons into the system in resonance or close to it at the lower dispersion relation of the polaritons at a given momentum k_p. As a consequence, there is a macroscopic occupation of the polariton mode at such a momentum , which is called the pump field. This scheme is particularly appealing since it does not include complicated secondary processes and it can be theoretically described with a good accuracy. Moreover, this system is particularly rich since it may exhibit a phase transition, from a disorder state (pump only case) to an ordered state (with a macroscopic occupation of more states apart from the pump state) by tunning the strength of the external pump power.

Since the typical lifetime of the cavity photons is much smaller than the typical one of the excitons, the relatively short live of the polaritons appears as a consequence of the photonic component of the polariton. Therefore, there is a one to one correspondence between the quantum state of the polaritons and the emitted photons from the cavity. Thus, all the different phenomena related to the quantum collective behaviour of the polaritons and single polariton states can be extracted

applying well developed tools of optics, such as photoluminescene, to measurements of the photons emitted from the cavity.

3.6 The Optical Parametric Oscillation (OPO) regime

Within the coherent pumping configuration there can be two discern regimes:

- the regime where the only stable polariton state in the system is generated by pump itself.
- the regime where the continuously injecting polaritons into the pump state are not stable therefore subsequently undergo coherent stimulated scattering into the signal state (close to the normal direction) and the idler state (on the other side of the pump).

A continuous wave (cw) laser above a threshold pump strength can induce parametric scattering into the signal and idler states, in which case we refer to the OPO regime. In this regime two polaritons from the pump mode with wavevector and frequency $\{\mathbf{k}_p, \omega_p\}$ scatter into a lower energy signal mode $\{\mathbf{k}_s, \omega_s\}$ and a higher energy idler mode $\{\mathbf{k}_i, \omega_i\}$ in the parametric scattering process. This procedure is subject to energy and momentum conservation with the requirements:

$$2\mathbf{k}_p = \mathbf{k}_s + \mathbf{k}_i \tag{3.23}$$

$$2\omega_p = \omega_s + \omega_i. \tag{3.24}$$

The above conditions cannot be satisfied by any particle dispersion. For instance, parametric scattering is prohibited for particles following a quadratic dispersion law. Parametric scattering is allowed for polaritons subject to the requirement:

$$2\omega_{lp}(\mathbf{k}_p) = \omega_{lp}(\mathbf{k}_s) + \omega_{lp}(|2\mathbf{k}_p - \mathbf{k}_s|). \tag{3.25}$$

If $\mathbf{k}_s = 0$, then the wavevectors of pump and idler are uniquely selected. The value of the pumping angle in this case is also referred to as the "magic angle", located close to the inflection point of the lower polariton dispersion branch. However, for a generic signal wavevector $\mathbf{k}_s = (k_x, k_y)$, and a fixed pump angle $\mathbf{k}_p$ in the x-direction, say, the final states allowed in the parametric scattering process describe an eight-like pattern in momentum space [78].

The OPO regime was realized in the first configuration used to experimentally study the spontaneous occurrence of macroscopic coherence in the polariton gas and the collective dynamics of coherent polariton fluids in planar microcavity systems [79]. Scattering processes in bosonic systems can be stimulated by an existing population in the final states, here represented by the signal and idler modes. For a pump intensity strong enough for the stimulated scattering rate to overcome losses, a new stationary regime with a macroscopic occupation of single signal and idler modes is reached. As a result, a pair of coherent signal and idler beams is emitted with an narrow distribution in the energy and in-plane wave-vector [10, 80].

There are strong analogies between the parametric oscillation operation and Bose-Einstein condensation transition which are apparent in the Penrose-Onsager criterion that the correlation function is non-zero [79]:

$$\lim_{|\mathbf{r}-\mathbf{r}'|} \langle \mathbf{E}_s^\dagger(\mathbf{r}) \mathbf{E}_s(\mathbf{r}') \rangle \neq 0 \tag{3.26}$$

as seen in the experimental results [81] and the numerical simulations [82].

Polariton parametric effects in planar microcavities have been addressed on the basis of a three-mode approximation involving a set of coupled nonlinear differential equations for the time evolution of the lower polariton field amplitudes in the pump, signal and idler modes [83–86]. The three mode approximation is limited to spatially homogeneous geometries and does not provide a criterion for determining the specific modes $\mathbf{k}_{s,i}$ taking part in the OPO operation. Na ively, one could perform a local density approximation around the $\mathbf{k}_{s,i}$ modes for which parametric gain is the strongest. However, $\mathbf{k}_{s,i}$ depend on the pump, signal and idler intensities as well, and the theory has to be formulated self-consistently [79].

3.7 The driven-dissipative Gross-Pitaevskii equation

To be more concrete, we now develop the model with which we describe the parametrically pumped system and the method by which we account for quantum fluctuations. In what follows, we consider the excitonic ψ_{x} and photonic ψ_{c} components of the polariton field which depend on the 2D spatial coordinates, $\mathbf{r} = (x, y)$, and

time t. The system Hamiltonian (before adding the decay and pumping process) is:

$$H_{\mathrm{S}} = \int d\mathbf{r} \Big[-\psi_{\mathrm{c}}^{\dagger} \tfrac{\hbar^2\nabla^2}{2m_{\mathrm{c}}} \psi_{\mathrm{c}} - \psi_{\mathrm{x}}^{\dagger} \tfrac{\hbar^2\nabla^2}{2m_{\mathrm{x}}} \psi_{\mathrm{x}} + \frac{g_{\mathrm{x}}}{2} |\psi_{\mathrm{x}}|^4 + \frac{\hbar\Omega_{\mathrm{R}}}{2} \left(\psi_{\mathrm{x}}^{\dagger}\psi_{\mathrm{c}} + \psi_{\mathrm{c}}^{\dagger}\psi_{\mathrm{x}} \right) \Big] ,$$

where g_{x} is the strength of the exciton-exciton interaction, Ω_{R} of the exciton-photon interaction (the Rabi splitting), and m_{x} and m_{c} are masses of exciton and photon respectively. The parametric drive and incoherent decay can be expressed by system-bath Hamiltonian

$$H_{\mathrm{SB}} = \int d\mathbf{r}\ F(\mathbf{r},t)(\psi_{\mathrm{c}}^{\dagger} + \psi_{\mathrm{c}}) + \sum_{k,\ell} \zeta_k^{\ell} (\psi_{\ell}^{\dagger} B_k^{\ell} + B_k^{\ell\dagger} \psi_{\ell}) + \sum_{k,\ell} \omega_k^{\ell} B_k^{\ell\dagger} B_k^{\ell} \quad ;$$

where $\ell \in \{\mathrm{x}, \mathrm{c}\}$ and $B_k, B_k^{\dagger}$ are standard bath's bosonic annihilation and creation operators with momentum k and frequency ω_k, describing excitonic and photonic decay processes, while the coherent pump is in general given by

$$F_p = f_p(\mathbf{r}) e^{i(\mathbf{k}_p \cdot \mathbf{r} - \omega_p t)}. \tag{3.27}$$

but we have uniform spatial profiles for the pump so,

$$f_p(\mathbf{r}) = f_p \tag{3.28}$$

Using standard methods to eliminate the environment [87], in the mean-field approximation the dynamic equations of motion describing the exciton and photon fields become

$$i\hbar\partial_t \begin{pmatrix} \psi_X \\ \psi_C \end{pmatrix} = \begin{pmatrix} 0 \\ F_p \end{pmatrix} + \Big[\hbar \begin{pmatrix} \omega_X(0) - \frac{\hbar\nabla^2}{2m_X} & \frac{\Omega_R}{2} \\ \frac{\Omega_R}{2} & \omega_C(0) - \frac{\hbar\nabla^2}{2m_C} \end{pmatrix} + \begin{pmatrix} g_X|\psi_X|^2 - i\kappa_X & 0 \\ 0 & -i\kappa_C \end{pmatrix} \Big] \begin{pmatrix} \psi_X \\ \psi_C \end{pmatrix} . \tag{3.29}$$

As the exciton mass is orders of magnitude heavier than photons, we can ignore the exciton dispersion and set $\hbar\omega_X(0) = 0$. Thus we get

$$i\hbar\partial_t \begin{pmatrix} \psi_X \\ \psi_C \end{pmatrix} = \begin{pmatrix} 0 \\ F_p \end{pmatrix} + \left[\hbar \begin{pmatrix} 0 & \frac{\Omega_R}{2} \\ \frac{\Omega_R}{2} & \delta - \frac{\hbar\nabla^2}{2m_C} \end{pmatrix} + \begin{pmatrix} g_X|\psi_X|^2 - i\kappa_X & 0 \\ 0 & -i\kappa_C \end{pmatrix} \right] \begin{pmatrix} \psi_X \\ \psi_C \end{pmatrix} \tag{3.30}$$

where $\delta = \omega_C(0) - \omega_X(0)$ and for a simplicity we will always set $\delta = 0$. and show rich and complex superfluid phenomena[88, 89]. Seeking steady-state solutions to these equations possessing signal, pump, and idler modes for different pump powers, one can determine a phase diagram for the OPO regime, as displayed in the inset in figure [4.13].

3.8 Stability of Polaritons in the OPO regime

The mean field description of polaritons by coupled GPEs for quantum well excitons and cavity photons has led to a successful interpretation of many superfluid phenomena. On the other hand, the OPO stability and the conditions under which OPO switches on and off can be found analytically employing with three mode approximations. For that reason, it is simpler to perform a basis transformation in the equation (3.30) from exciton and photon basis into the lower- and upper-polariton basis, as described by (3.16). It is also advantageous to work in the momentum space through the transformations

$$\psi_X(\mathbf{r}, t) = e^{i\omega t} \sum_{\mathbf{k}} e^{i\mathbf{k}\cdot\mathbf{r}} \psi_{X,\mathbf{k}}$$

$$\psi_C(\mathbf{r}, t) = e^{i\omega t} \sum_{\mathbf{k}} e^{i\mathbf{k}\cdot\mathbf{r}} \psi_{C,\mathbf{k}}.$$

We can subsequently rotate the basis

$$\begin{pmatrix} \psi_{X,\mathbf{k}} \\ \psi_{C,\mathbf{k}} \end{pmatrix} = \begin{pmatrix} \cos\theta_{\mathbf{k}} & -\sin\theta_{\mathbf{k}} \\ \sin\theta_{\mathbf{k}} & \cos\theta_{\mathbf{k}} \end{pmatrix} \begin{pmatrix} \psi_{LP,\mathbf{k}} \\ \psi_{UP,\mathbf{k}} \end{pmatrix}. \tag{3.31}$$

In the above relations we neglect contributions from the upper-polariton branch and assume that the Rabi splitting is larger than all other energy scales featuring in the problem. Hence, the lower- and upper-polariton branches are not mixed together by the nonlinear terms. The mean field equations of motion for excitons and photons (3.30) can be restricted to a single classical field, involving the lower-polaritons ψ_{LP}

as below:

$$i\hbar\partial_t\psi_{LP,\mathbf{k}} = \hbar\left(\omega_{LP}(\mathbf{k}) - i\kappa_{LP}(\mathbf{k})\right)\psi_{LP,\mathbf{k}} + \sum_{\mathbf{k}_1,\mathbf{k}_2} g_{\mathbf{k}\mathbf{k}_1,\mathbf{k}_2}\psi^*_{LP,\mathbf{k}_1+\mathbf{k}_2-\mathbf{k}}\psi_{LP,\mathbf{k}_1}\psi_{LP,\mathbf{k}_2} + \tilde{F}_p, \tag{3.32}$$

where the decay rate of the lower-polariton branch is given by the expression

$$\kappa_{LP}(\mathbf{k}) = \kappa_X \cos^2\theta_{\mathbf{k}} + \kappa_C \sin^2\theta_{\mathbf{k}} \tag{3.33}$$

and the momentum dependent polariton-polariton non-linear interaction strength can be found as

$$g_{\mathbf{k}\mathbf{k}_1,\mathbf{k}_2} = g_X \cos\theta_{\mathbf{k}} \cos\theta_{|\mathbf{k}_1+\mathbf{k}_2-\mathbf{k}|} \cos\theta_{\mathbf{k}_1} \cos\theta_{\mathbf{k}_2}. \tag{3.34}$$

For a homogeneous case the pump profile is given by

$$\tilde{F}_p = \sin\theta_{\mathbf{k}} f_p e^{-i\omega t}\delta_{\mathbf{k},\mathbf{k}_p}. \tag{3.35}$$

We will now investigate the solutions of equation (3.32) where only the pump polariton mode is occupied. These solutions assume the exact form:

$$\psi_{LP}(\mathbf{r},t) = Pe^{i(\mathbf{k}_p\cdot\mathbf{r}-\omega_p t)} \quad \Longrightarrow \quad \psi_{LP,\mathbf{k}}(t) = P\delta_{\mathbf{k},\mathbf{k}_p}e^{-i\omega_p t}, \tag{3.36}$$

where P is the complex amplitude satisfying

$$\left(\omega_{LP}(\mathbf{k}_p) - \omega_p - i\kappa_{LP}(\mathbf{k}_p) + g_X\cos^4\theta_{\mathbf{k}_p}|P|^2\right)P + \sin\theta_{\mathbf{k}_p} f_p = 0. \tag{3.37}$$

In the above relation, the nonlinear term, $g_X\cos^4\theta_{\mathbf{k}_p}|P|^2$ represents the self-interaction renormalising the effective detuning of the injected polaritons. The presence of this term results in the blue-shift of the corresponding dispersion due to self-interactions:

$$\Delta_p = \omega_p - \omega_{LP}(\mathbf{k}_p) - g_X\cos^4\theta_{\mathbf{k}_p}|P|^2. \tag{3.38}$$

The cubic equation for the complex amplitude P (3.37) admits two qualitatively different solutions depending on the detuning, namely whether the pump is blue or red-shifted with respect to the lower-polariton dispersion. For instance, if the detuning is

$$\omega_p - \omega_{LP}(\mathbf{k}_p) > \sqrt{3}\kappa_{LP}(\mathbf{k}_p), \tag{3.39}$$

then the corresponding solution has extrema, resulting in a characteristic S curve for $|P|^2$ as a function of pump-power, f_p. This is shown in Figure 3.5. Hence, the system exhibits bistable behaviour.

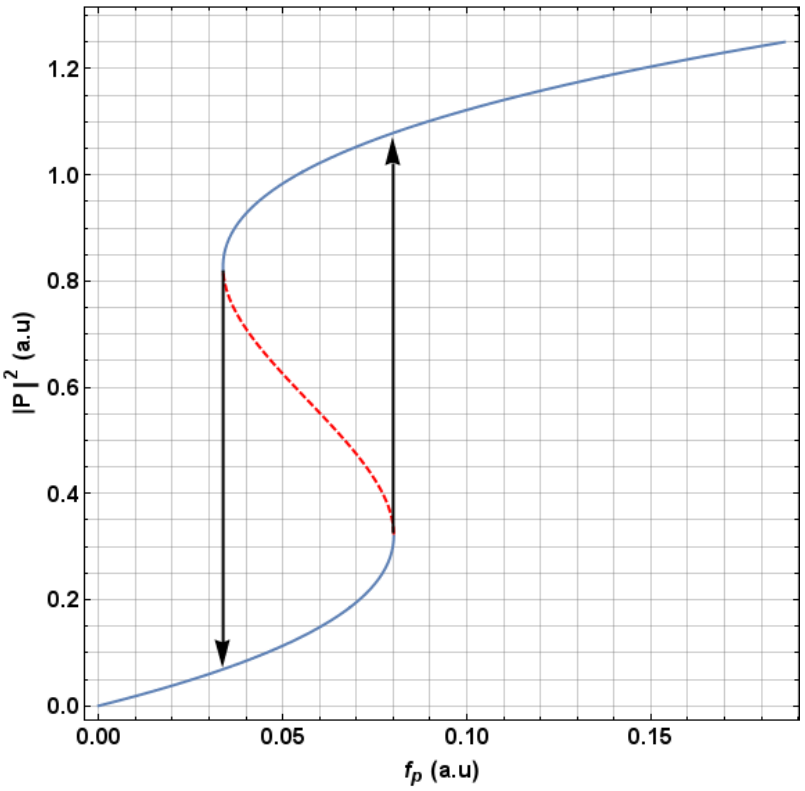

Figure 3.5: The S curve: Pump-polariton population as a function of the pump-power. The red dashed line represents the unstable region.

Because the branch with negative slope is unstable, the polariton density in the pump-only mode follows a hysteresis behaviour: by increasing the pump intensity, the pump-only mode eventually jumps abruptly into the upper branch, while if the intensity is then lowered, the polariton population decreases and jumps back down to the lower branch. Optical bistability in microcavity polaritons has been observed in [90, 91], evidencing a hysteresis cycle of the polaritonic emission as a function of the pump intensity.

If instead the detuning is

$$\omega_p - \omega_{LP}(\mathbf{k}_p) \leq \sqrt{3}\kappa_{LP}(\mathbf{k}_p) \tag{3.40}$$

the system is in the optical limiter regime, in which the population $|P|^2$ grows

monotonically as a function of the pump intensity f_p.

The dynamical stability of the pump-only solution (6.12) can be ensured by allowing states other than the pump (namely, the signal and idler states) to be perturbatively populated via parametric scattering processes:

$$\psi_{LP,\mathbf{k}}(t) = S\delta_{\mathbf{k},\mathbf{k}_s}e^{-i\omega_s t} + P\delta_{\mathbf{k},\mathbf{k}_p}e^{-i\omega_p t} + I\delta_{\mathbf{k},\mathbf{k}_i}e^{-i\omega_i t}, \tag{3.41}$$

where $\{\mathbf{k}_s = \mathbf{k}_p - \mathbf{q}, \quad \omega_s = \omega_p - \omega\}$ and $\{\mathbf{k}_i = \mathbf{k}_p + \mathbf{q}, \quad \omega_i = \omega_p + \omega\}$ depending on whether the time evolution of these states grows exponentially in time or not. Expanding to the first order in S and I, one obtains an eigenvalue problem for the amplitudes S and I [85, 92, 93]:

$$\begin{pmatrix} \omega - \Delta_s - i\kappa_{LP}(\mathbf{k}_s) & g_X \cos\theta_{\mathbf{k}_s}\cos^2\theta_{\mathbf{k}_p}\cos\theta_{\mathbf{k}_i}P^2 \\ g_X \cos\theta_{\mathbf{k}_s}\cos^2\theta_{\mathbf{k}_p}\cos\theta_{\mathbf{k}_i}P^{*2} & -\omega - \Delta_i + i\kappa_{LP}(\mathbf{k}_i) \end{pmatrix} \begin{pmatrix} S \\ I \end{pmatrix} = 0, \tag{3.42}$$

where

$$\Delta_s = \omega_p - \omega_{LP}(\mathbf{k}_s) - 2g_X \cos^2\theta_{\mathbf{k}_s}\cos^2\theta_{\mathbf{k}_p}|P|^2$$

and

$$\Delta_i = \omega_p - \omega_{LP}(\mathbf{k}_i) - 2g_X \cos^2\theta_{\mathbf{k}_i}\cos^2\theta_{\mathbf{k}_p}|P|^2$$

. The complex eigenvalues ω can be obtained under the requirement that the determinant of the matrix in (3.42) is zero. The dynamical stability is established if $Im\{\omega\} > 0$. Therefore, the threshold for instability in the pump-only solution (3.36) can be found by imposing the condition $Im\{\omega\} = 0$. Fixing the pump wavevector ($\mathbf{k}_p$ and energy ω_p) and the signal wavevector $\mathbf{k}_s$ (as well as the exciton and photon lifetimes, κ_X and κ_C), leads to a criterion for identifying the boundaries of the instability region, i.e. the lowest and highest values of the LP population $|P|^2$ for which the pump-only solution is unstable. As shown in [85, 92, 93], one can classify the instability as a single mode instability when $\mathbf{q} = 0$ and hence the Kerr instability with $\mathbf{k}_p = \mathbf{k}_s = \mathbf{k}_i$. In particular, the negative slope branch of the bistability curve (dashed line in Figure 3.5) is always single mode unstable [85, 93]. If instead $\mathbf{q} \neq 0$, the instability is parametric-like. In that case, the total extent of the instability region with different values of $\mathbf{k}_s$ is significantly larger than the sole branch with negative slope.

The OPO state does not require a bistable behaviour and can equally turn on in the optical limiter case. It is possible to plot a "phase diagram" [92] of the pump energy ω_p as function of the pump wavevector $\mathbf{k}_p$, depicting the regions where

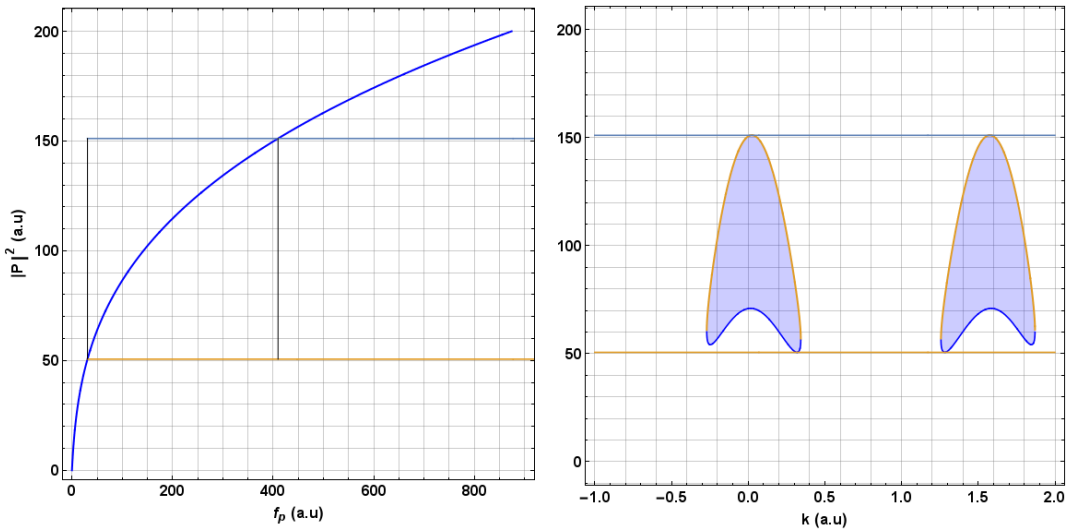

Figure 3.6: **Right panel**. The blue line: Population of pump mode as a function of pump-power in the optical limiter regime. The orange (light blue) line: Pump mode population at the lower (upper) OPO threshold. Black vertical lines: Upper and lower threshold pump-powers. **Left panel**. Population of pump mode as a function of signal momenta. In the shaded regions, pump-only states are unstable.

a pump-only solution is always stable, the regions where the OPO switches on, and a regime where only a Kerr-type instability can occur instead. Following this construction, it was shown in [92] that the "magic angle" for the pump has no particular significance. Rather, OPO conditions can be found for all angles larger than a critical value, $\theta_p > \theta_c$ (10° for the parameters of [92]), as has been also confirmed experimentally in [86, 94]. In addition, the energy renormalisation of the polariton dispersion due to interactions shifts the emission angles for the signal always closer to $\theta_s \sim 0$ [86, 92]. This is also verified by the numerical simulations we have carried out.

The method described above implies negligible populations of the signal S and the idler I modes, and therefore, it allows to find the conditions for the OPO threshold.

3.9 Stochastic approach to polariton dynamics

Building upon the Gross-Pitaevskii equations (3.30) or (3.32) to account for the quantum and thermal fluctuations of the quantum field $\hat{\Psi}_{LP}$ is a very arduous task in the general case. A number of different methods have been recently developed to

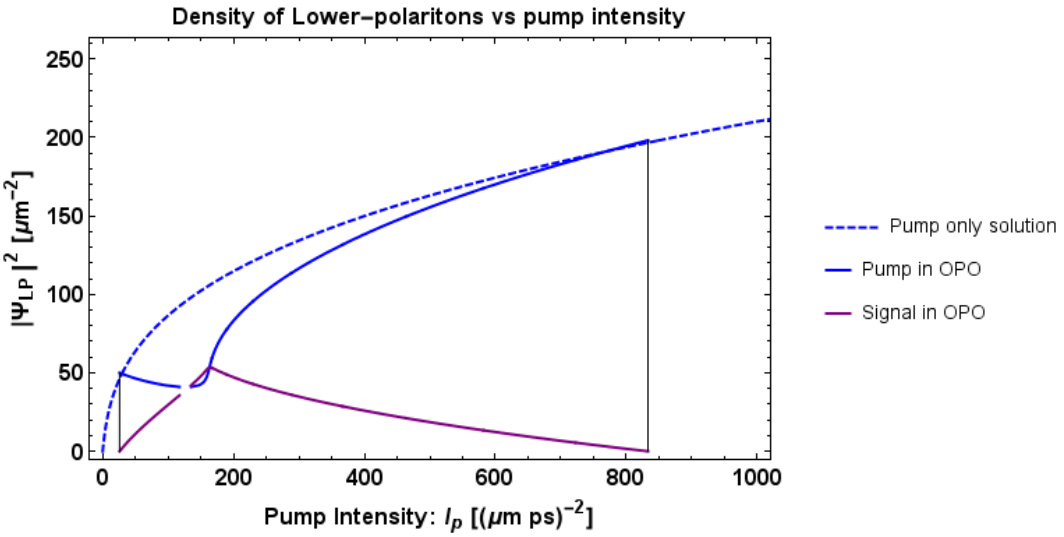

Figure 3.7: Mean field OPO phase diagram. Blue dashed-stable pump-only states. Blue solid-unstable pump-only states. Purple-Population of signale mode. Black vertical-Upper and lower threshold, same lines as in Figure 3.6.

tackle this problem in different regions, with the Path Integral Monte Carlo methods for the thermal equilibrium state [95], diagrammatic techniques [96, 97] density matrix renormalization group techniques for the both the ground state and the temporal dynamics [98] amongst the most representative examples.

In this section we will review some phase space techniques originally developed in quantum optics and recently employed in the study of quantum fluids of atoms and photons. The crux is to represent the state of the quantum field as a quasi-probability distribution function on an appropriate classical phase space, and describe the time-evolution of the field in terms of a Fokker-Planck partial differential equation (FPE) which can be subsequently mapped onto a stochastic partial differential equation. An introductory treatment of the quantum field phase space representations can be found in [99].

A crucial feature is the positivity of the quasi-probability distribution function and the time-evolution be described by a FPE in view of efficient numerical simulations [100]

$$\frac{\partial P(\mathbf{r},t)}{\partial t} = -\sum_{i=1}^{M} \frac{\partial}{\partial r_i}\left[F_i(\mathbf{r},t)P(\mathbf{r},t)\right] + \frac{1}{2}\sum_{i,j=1}^{M} \frac{\partial^2}{\partial r_i \partial r_j}\left[D_{i,j}(\mathbf{r},t)P(\mathbf{r},t)\right], \qquad (3.43)$$

with a drift force $\mathbf{F}$ and a positive definite diffusion matrix D. We define here the

quasi-probability distribution $P(\mathbf{r},t)$ on a M-dimensional space with real spatial co-ordinates r_i. The probability distributions for complex quantities are straightforwardly formulated by treating the real and imaginary parts as independent real variables. For a positive definite diffusion matrix D, the FPE can be mapped onto a system of M stochastic differential equations according to the rules of Ito calculus [101] as below

$$dr_i = F_i(\mathbf{r},t)dt + dW_i \tag{3.44}$$

with a Wiener noise subject to

$$dW_i dW_j = D_{i,j}(\mathbf{r},t)dt. \tag{3.45}$$

These equations can be efficiently simulated by considering the statistical average over many different realizations of the Brownian motion.

In most cases of actual interest this is unfortunately not possible either due to a non positive-definite diffusion matrix D or due to the presence of additional terms with higher order partial derivatives of P in the right-hand side of (3.43): for the system of interacting bosons we are here investigating, non-positive diffusion terms appear in the time-evolution of P and Q representations, while third order derivative terms feature in the time-evolution of the Wigner function [102].

In the following we will concentrate on the Wigner representation that has proven to be most useful in calculations of practical interest. For simplicity, we restrict ourselves to the coherent pumping case for which there exists a self-contained Hamiltonian description [82]. In order to extend to the incoherent pumping case we are in need of some modelling for the relaxation mechanisms taking place in the experimental device: the first endeavour in that direction has been recently reported in [103]. Typical applications of the Wigner representation require the quantum field discretisation on a d dimensional discrete lattice of N^d points confined inside an integration box of side L. In this configuration, the Wigner distribution is a function of the N^d complex amplitudes $\psi_i = \psi(\mathbf{r}_i)$ of the field at the lattice positions $\mathbf{r}_i$. Its time-evolution is governed by the FPE-like equation

$$\begin{aligned}\frac{\partial W}{\partial t} = & -\sum_i \frac{\partial}{\partial \psi_i}\left[F_i\{\psi\}W\{\psi\}\right] - \sum_i \frac{\partial}{\partial \psi_i^*}\left[F_i\{\psi\}W\{\psi\}\right] + \frac{\kappa_{LP}}{\Delta V}\frac{\partial^2 W\{\psi\}}{\partial \psi_i^* \partial \psi_i} \\ & + i\frac{g_{LP}}{4\Delta V^2}\frac{\partial^2}{\partial \psi_i^* \partial \psi_i}\left[\frac{\partial}{\partial \psi_i^*}\left(\psi_i^* W\{\psi\}\right) - \frac{\partial}{\partial \psi_i}\left(\psi_i W\{\psi\}\right)\right]\end{aligned} \tag{3.46}$$

where $\Delta V = (L/N)^d$ is the volume of the elementary cell of the discrete lattice. The drift force term on the $\mathbf{r}_i$ site $F_i\{\psi\} = F_i\{\psi\}(\mathbf{r} = \mathbf{r}_i)$ involves a deterministic evolution of the field very similar to the right-hand side of (3.30) or (3.32).

We define the derivatives with respect to the complex field variable ψ as

$$\frac{\partial}{\partial\psi} = \frac{1}{2}\left(\frac{\partial}{\partial \mathrm{Re}[\psi]} - i\frac{\partial}{\partial \mathrm{Im}[\psi]}\right), \qquad \frac{\partial}{\partial\psi^*} = \frac{1}{2}\left(\frac{\partial}{\partial \mathrm{Re}[\psi]} + i\frac{\partial}{\partial \mathrm{Im}[\psi]}\right).$$

The second-order derivative term is always positive and can be straightforwardly mapped onto a noise term with local spatial correlations. On the other hand, the third order derivative terms can not be included in a standard stochastic differential equation of the form (3.45).

The main practical interest of the Wigner representation arises from the different scaling of the various terms featuring in (3.46) within the dilute gas limit $\psi \to \infty$, $g_{LP} \to 0$ at a constant interaction energy $g_{LP}|\psi|^2$. In this limit, the presence of noise causes a statistical fluctuation of the field ψ around its mean field value, on the order of $\Delta\psi \propto 1/\sqrt{\Delta V}$. The characteristic magnitude of the third order derivative term is roughly estimated accordingly to be on the order of $g_{LP}/\Delta V$. This estimate is compared to the diffusion term which is of the order of κ_{LP}. Provided

$$\kappa_{LP} \gg g_{LP}/\Delta V, \tag{3.47}$$

we anticipate that accurate results for a nonequilibrium gas of photons can be obtained by truncated Wigner calculations. In this procedure we completely neglect third order derivative terms and as a result the stochastic partial differential equation can be written in the form:

$$d\psi(\mathbf{r},t) = F\{\psi\}(\mathbf{r})dt + \sqrt{\frac{\kappa_{LP}}{2\Delta V}}dW(\mathbf{r},t), \tag{3.48}$$

involving a complex Gaussian noise term dW of zero mean that satisfies

$$\langle dW_i(\mathbf{r},t)dW_j^*(\mathbf{r}',t)\rangle = dt\delta_{\mathbf{r},\mathbf{r}'}. \tag{3.49}$$

Under the condition (3.47), the non-classical correlations due to the third-order derivative term decay fast owing to the losses and the classical noise associated with κ_{LP}: in particular, the magnitude of the classical noise is the "appropriate" one to simulate accurately the quantum dynamics on a computer. In [104], it was shown

how the truncated Wigner approach has been proven able to capture the quantum fluctuations at least at the level of Bogoliubov theory.

Chapter 4

Non-Equilibrium BKT transition in Polaritons

4.1 Introduction

Physical systems in two (or fewer) dimensions cannot exhibit a true long-ranged order at finite temperature due to the HMW theorem which prohibits such systems form spontaneously breaking a continuous symmetry. This is because the Goldstone mode associated with such a broken symmetry is massless and hence is infrared divergent in low dimensions. The fluctuations due to the Goldstone modes are therefore always so strong as to be able to "shake apart" any possible long-ranged order. The Berezinskii-Kosterlitz-Thouless (BKT) mechanism provides a loophole to the HMW theorem by which two-dimensional systems can exhibit a quasi-long-ranged order,where correlations decay as a power law at large distances, which breaks a global $U(1)$ symmetry. In a wide class of systems, Kosterlitz and Thouless showed that topological defects, such as vortices in superfluids or dislocations in crystals, possess an *unbinding* transition, using a simple argument in which one compares the energy cost of introducing such a defect with the entropy due to the number of places it could be centered. Such topological defects, by their very nature, cannot be smoothly deformed away and so the Goldstone mode produced by breaking the $U(1)$ symmetry has no effect on them. By examining how the presence of topological defects renormalizes bare system parameters one can then show that the binding transition induces an ordering transition on the system as a whole.

In the archetypal example of the classical 2D-XY model, $H_{XY} = J\sum_{<i,j>}\cos(\theta_i -$

θ_j), one finds a critical temperature $k_B T_{\mathrm{BKT}}/J = \pi/2$, above which the system shows short range correlations – $\langle \cos(\theta_m - \theta_n) \rangle \sim \exp^{-r_{mn}/\xi}$ where $\xi \sim 1/\ln T$ – but below which the system develops a quasi-long-ranged order – $\langle \cos(\theta_m - \theta_n) \rangle \sim r_{mn}^{-k_B T/(2\pi J)}$. One notices an upper bound on the algebraic decay here as the exponent cannot exceed its value at T_{BKT}, i.e. $1/4$. A proper self consistent treatment of the BKT critical temperature would include the renormalization of T_{BKT} itself, however this could only serve to *decrease* the critical temperature so that $1/4$ remains a strict upper bound on the exponent.

The BKT transition is relevant for a wide range of physical systems, perhaps the most celebrated examples are those in the context of superfluids and superconductors, where despite the absence of a true long range order and a true condensate in two dimensions a clear superfluid behaviour has been experimentally observed in the quasi-ordered phase [49]. Indeed, it has been shown experimentally [54] that the transition from a normal to a superfluid phase in an ultra-cold gas of bosonic atoms is of the BKT type despite weak interactions and harmonic trapping potentials. This was far from obvious as the harmonic trapping modifies the density of states to allow in principle Bose-Einstein condensation and a true condensate in an non-interacting system [2, 38].

All these considerations are applicable to equilibrium closed systems, where it can be shown that the phase with free vortices or bound vortex-anti-vortex pairs lowers the free energy. However, in recent years a new class of two-dimensional quantum systems emerged: strongly driven and highly dissipative interacting many-body light-matter systems such as for example polaritons in semiconductor microcavities [73], cold atoms in optical cavities *cite* or cavity arrays [105, 106]. Due to the strongly dissipative nature of the photonic part those systems are strongly driven to sustain a non-equilibrium steady state. And indeed a transition from normal to superfluid phase in the driven polariton systems has been observed and superfluid properties of the ordered phase explored [107–111].

Being strongly driven, the system no longer obeys the principle of free energy minimisation and so it is not obvious whether the transition between the normal and superfluid phase as the density of particles is increased is of the BKT type i.e due to vortex-antivortex pairs unbinding. Current experiments are not yet able to image at the single shot level and so are not sufficiently sensitive to detect randomly moving

vortices. Algebraic decay of correlations was reported from the shot averaged data [112], however, a larger exponent of that power-law that it is possible in equilibrium posed questions to the mechanism of the transition. On the theory side, by mapping the complex Ginzburg-Landau equation describing long-wavelength condensate dynamics onto the anisotropic Kardar-Parisi-Zhang (KPZ) equation, Altman et al [113] concluded that although no algebraic order is possible in a truly infinite system, the KPZ length scale is certainly much larger than any reasonable system size in the case of microcavity polaritons.

Using particularity convenient example of parametrically driven polariton system in the non-equilibrium steady-state we show that despite the presence of a strong drive, dissipation and non-equilibrium the transition from the normal to the superfluid phase in this light-matter interacting system is of a BKT type i.e governed by binding and dissociation of vortex-antivortex pairs as a function of increasing particle density. Despite the presence of a strong drive and non-thermal distribution the transition and the ordered/disordered phases bare a lot of similarities to their equilibrium counterpart. However, as early experiments suggested, we find that a larger exponent of the power-law decay of correlations, before vortices unbind and destroy the quasi-long-range order leading to exponential decay, is possible. This suggests that the external drive, decay and associated noise favours excitations of collective excitations, the Goldstone phase modes, which lead to faster spatial decay, over vortices which would destroy the quasi-order all together. This externally over-shaken but not stirred quantum fluid constitutes an interesting new laboratory to explore non-equilibrium phases of matter.

Outline of the chapter: In this supplementary information we provide a more detailed account of some of the technical issues arising from our numerical methods, which are not of sufficiently general interest to warrant a discussion in the main text, but which are germane to the validity of our conclusions. In particular, we discuss the filtering we perform in order to isolate the signal state, and the loss in resolution this incurs, and we describe various tests we have undertaken in order to ensure that the results we present are properly converged.

4.2 Parameters and numerical convergences.

We simulate the stochastic evolution of equation (3.48) with the XMDS2 software framework [114] using a fixed-step 4th order Runge-Kutta algorithm. The algorithm tested against 9th order Runge-Kutta as well as Semi-Implicit fixed-step, with three and five iterations, algorithms and chosen because of its fast and equally reliable with other algorithms. From the point of view of numerics it is always convenient to work with dimensionless equations. Therefore, we will rescale our equations of motion and throughout in this subsection we will use the dimensionless units and mark ($'$).

4.2.1 Rescaling and parameters.

In order to reduce unnecessary numerical costs of the simulations we rewrite the equations (3.30) and (3.48) with rescaling energies by $\hbar\Omega_R/2$ and measuring time in $(\Omega_R/2)^{-1}$ units, so all variables and parameters can be replaced by its dimensionless version:

$$i\partial_{t'}\begin{pmatrix}\psi'_X\\ \psi'_C\end{pmatrix}=\begin{pmatrix}0\\ F'\end{pmatrix}+\left[\begin{pmatrix}0 & 1\\ 1 & -\nabla'^2\end{pmatrix}+\begin{pmatrix}|\psi'_X|^2-i\kappa'_X & 0\\ 0 & -i\kappa'_C\end{pmatrix}\right]\begin{pmatrix}\psi'_X\\ \psi'_C\end{pmatrix}. \quad (4.1)$$

and

$$id\begin{pmatrix}\psi'_X\\ \psi'_C\end{pmatrix}=\left\{\begin{pmatrix}0\\ F'\end{pmatrix}+\left[\begin{pmatrix}0 & 1\\ 1 & -\nabla'^2\end{pmatrix}+\begin{pmatrix}|\psi'_X|^2-\frac{g'_X}{\Delta V'}-i\kappa'_X & 0\\ 0 & -i\kappa'_C\end{pmatrix}\right]\begin{pmatrix}\psi'_X\\ \psi'_C\end{pmatrix}\right\}dt' + \sqrt{\frac{g'_X}{2\Delta V'}}\begin{pmatrix}\sqrt{\kappa'_X}dW'_X\\ \sqrt{\kappa'_C}dW'_C\end{pmatrix}. \quad (4.2)$$

Here we rescaled:
$t=(2/\Omega_R)t'$, $\psi_{X,C}=\sqrt{\frac{\hbar\Omega_R}{2g_X}}\psi'_{X,C}$, $F=\left(\frac{\hbar\Omega_R}{2}\sqrt{\frac{\hbar\Omega_R}{2g_x}}\right)F'$, $\kappa_{C,X}=\left(\frac{\hbar\Omega_R}{2}\right)\kappa'_{C,X}$, $\mathbf{r}=\ell_C\mathbf{r}'$, $\Delta V=\ell_C^2\Delta V'$ and $g_X=\left((\hbar\Omega_R/2)\ell_C^2\right)g'_X$ where $\ell_C=\sqrt{\frac{\hbar}{m_C\Omega_R}}$ is the healing length.

In line with experimental observation [109], the Rabi frequency is chosen to be $\hbar\Omega=4.4$meV, the mass of the microcavity photons is taken to be $m_C=2.3\times10^{-5}m_e$, where m_e is the electron mass, the mass of the excitons is much greater than this so we may take $m_X^{-1}\to 0$, the exciton and photon decay rates as $\kappa_X=\kappa_C=0.1$ meV, and the exciton-exciton interaction strength $g_X=0.002$ meVμm^2

[115].

variables	rescaled variables	parameters	rescaled parameters
time (t)	$(2/\Omega_R)t' \simeq (0.3ps)t'$	$m_C = 2.3 \times 10^{-5} m_e$	
		$\hbar\Omega_R \simeq 4.4meV$	$(\hbar\Omega_R)' \simeq 2$
length (L)	$\ell_c L' \simeq (0.868\mu m)L'$	$\hbar\omega_p \simeq -1.0meV$	$(\hbar\omega_p)' \simeq -0.454545$
		$l_c \simeq 0.868\mu m$	$\ell_c' \simeq 1$
field (ψ)	$\sqrt{\frac{\hbar\Omega_R}{2g_X}}\psi' \simeq (33.166\mu m^{-1})\psi'$	$\kappa_C \simeq 0.1meV$	$\kappa_C' \simeq 0.045454545$
		$\kappa_X \simeq 0.1meV$	$\kappa_X' \simeq 0.045454545$
pump (F)	$\left(\frac{\hbar\Omega_R}{2}\sqrt{\frac{\hbar\Omega_R}{2g_x}}\right) F' \simeq (72.966\frac{meV}{\mu m})F'$	$k_p \simeq 1.6\mu m^{-1}$	$k_p' \simeq 1.39127674658977$
		$g_x \simeq 0.002meV\mu m^2$	$g_x' \simeq 0.00121$

Table 4.1: Characteristics for each of the GaAs quantum wells and for the microcavity, useful constants and conversion factors of rescaled dimensionless experimental parameters.

To optimize parametric scattering from the pump to the signal and idler states, the momentum of the pump is fixed above the inflection point of the lower polariton spectrum at $\mathbf{k}_p = (k_p, 0)$ where $k_p = 1.6\mu\text{m}^{-1}$, with a frequency $\hbar\omega_p = \hbar\omega_X(0) - 1.0\text{meV}$ which amounts to pumping just below the LP spectrum. Finally all variables and parameters in real and rescaled units are summarized in the Table 4.1.

4.2.2 Numerical convergences with respect to the chosen box and grid.

In order to satisfy the condition (3.47), whilst maintaining sufficient resolution and a large enough range in momentum to completely contain the idler state, the simulation is performed on a 2D grid of $N_x \times N_y = 280 \times 280$ points on a box $L_x \times L_y = 280\ell_c \times 280\ell_c$ with a lattice spacing of $a = \ell_c = 0.866\mu\text{m}$, so that

$$2\kappa_{X,C} \gg g_x/\Delta V \Longrightarrow 0.2 > 0.00265455,$$

and the range in momentum is

$$k_{\max} = \pi/a \approx 3.62\mu\text{m}^{-1} > k_{\text{idler}}.$$

Noise consistence and step-size.

Strength of the Wiener noise terms in the equations (3.48) and (4.2)s are

determined by decay rates and the fixed step-size of the numerical integration. Therefore, the step-size one has to be correctly fixed which can be tested with no pump case, when there is no pump total density of photons in average should be zero. The average density is given by

$$\left\langle \psi_C'^*(\mathbf{r})\psi_C'(\mathbf{r})\right\rangle - \frac{g_x'}{2\Delta V'} = 0 \Longrightarrow \left\langle \psi_C'^*(\mathbf{r})\psi_C'(\mathbf{r})\right\rangle = 6.05\times 10^{-4}. \tag{4.3}$$

If our time step-size is too large to resolve the dynamics the solution grows exponentially. Eventually it becomes infinite and integration involves both add and subtract operations, so very soon after we get NaN's, not a number. In Figure 4.1 we show the noise consistence with time step $dt' = 0.01$ where the dashed-red line is the $\frac{g_x'}{2\Delta V'}$.

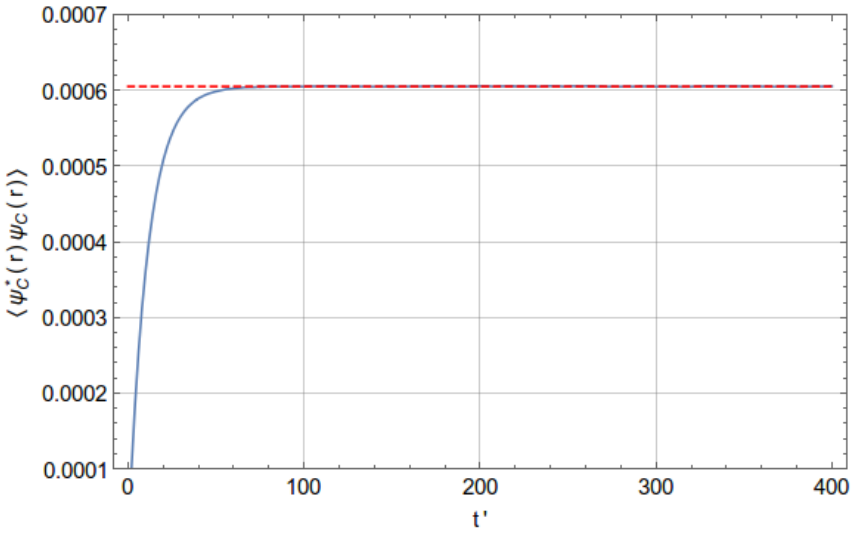

Figure 4.1: Noise consistence. Taken 96 realizations and the step-size of the integration is $dt' = 0.01$.

Convergence in box size and number of points in the grid.

The numerical convergences of the results obtained with the chosen box size and the grid, $N_x \times N_y = 280 \times 280$ and box $\{-L_x', L_x'\} \times \{-L_y', L_y'\}$ with $L_y' = L_x' = 140.0$, are tested for the case of the pump strength $f_p' = 0.071$. Parameters governing the resolution in space, the one in momentum and the extension of the box in momentum space $\left(\{-k_{x:\max}', k_{x:\max}'\} \times \{-k_{y:\max}', k_{y:\max}'\}\right)$

are given by

$$\Delta L'_{x,y} = \frac{2L'_{x,y}}{N_{x,y}} \qquad \Delta k'_{x,y} = \frac{2\pi}{2L'_{x,y}} \qquad k'_{x,y:\max} = \frac{\pi}{\Delta L'_{x,y}} = \frac{\pi N_{x,y}}{2L'_{x,y}} \,. \tag{4.4}$$

For the chosen box and the grid the resolution in space is $\Delta L'_{x,y} = 1.0$ while the resolution in momentum space is $\Delta k'_{x,y} = \pi/140.0$. Therefore the extension of the box in momentum space is $k'_{x,y:\max} = \pi$; this number has to be big enough to contain the idler momenta in order to have stimulated scattering.

In order to check convergence in space, we have chosen two different grids, $N_{x,y} = 256$ and $N_{x,y} = 320$, with same box size so that the resolution in momentum space did not change but the resolution in space, $\Delta L'_{x,y} = 1.094$ and $\Delta L'_{x,y} = 0.875$ respectively, is changed.

To check convergence in momentum space, instead we have forced to choose $N_{x,y} = 560$ and $L'_{x,y} = 280.0$ to pump exactly at the same point in the momentum space so that is now we have twice better resolution in momentum space while the resolution in space has not changed. The comparison among different grids and box sizes shown in Figure 4.2.

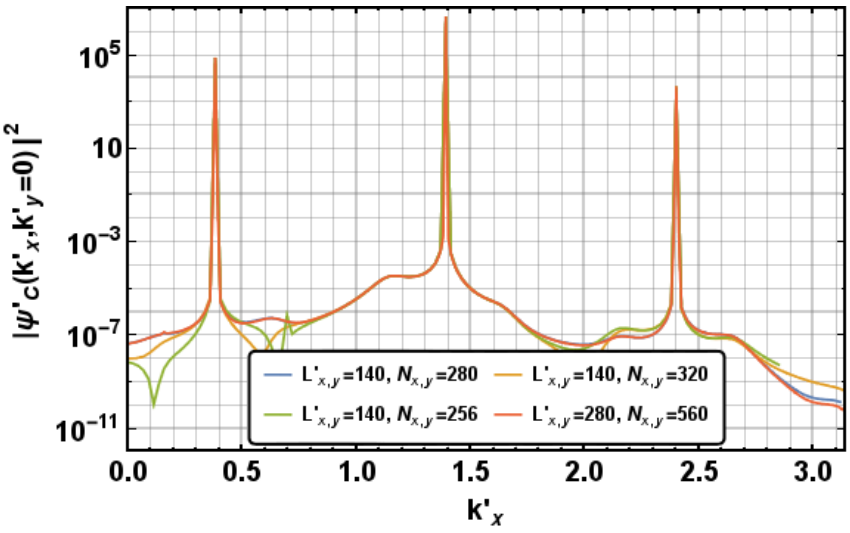

Figure 4.2: The numerical convergence on different grids.

4.3 Simulations and results

Polaritons are coherent superpositions of excitons and photons in a semiconductor microcavity [9]. They have a finite lifetime, so their steady-state is intrinsically non-equilibrium: continuous re-population from an external source is required to balance photonic losses. In the optical parametric oscillator (OPO) regime [10, 80], polaritons are resonantly injected into a pump state by a coherent laser field, before undergoing parametric scattering to signal and idler states (see illustration in Figure 4.5). The sum of the phases of the signal and idler is locked by the pump, but their relative phase is otherwise free. Any explicit choice by the system would break U (1) gauge symmetry a feature which implies the appearance of a Goldstone mode [116]. Another popular pumping scheme is incoherent injection of hot carriers, which relax down to the polariton ground state by exciton formation and interactions with the lattice phonons [1, 9]. However, the incoherently pumped polariton system is challenging to model due to the complicated and not yet fully understood processes of pumping and relaxation. As a result, one is typically forced to use phenomenological models [117] which often suffer from spurious divergences. From this point of view, the parametric pumping scheme is particularly appealing, as an ab initio theoretical description can be developed in terms of a system Hamiltonian [102], and its predictions can be directly compared to experiment.

One important distinction between the OPO system and more commonly studied superfluid systems is that, in order to study the condensate at the signal (or idler), we have to filter the full emission $\psi_C(\mathbf{r}, t)$ in such a way as to omit contributions with momentum outside a set radius about the signal (idler) states in $\mathbf{k}-$space. This applies both to the theory and the experimental data. Experimentally, the signal is isolated through spectral filtering. For our purposes, we define

$$\psi_{s,p,i}(\mathbf{r}, t) = \sum_{|\mathbf{k}-\mathbf{k}_{s,p,i}|<\tilde{k}_{s,p,i}} \psi_{C,\mathbf{k}}(t) e^{i\mathbf{k}\cdot\mathbf{r}}, \tag{4.5}$$

where $\mathbf{k}_{s,p,i}$ is the momentum of the signal, pump and idler states respectively and $\tilde{k}_{s,p,i}$ is the filtering radius. We fix the filtering radius to be $\tilde{k}_{s,p,i} = \frac{1}{2}|\mathbf{k}_{s,i} - \mathbf{k}_p|$ and choose to operate in the frame of reference co-moving with the signal (idler) so that the (physically irrelevant) background current does not show in the data. The filtering reveals the phase-freedom of the signal (idler) state at the expense of spatial resolution. Note, that this limits our ability to distinguish vortex-antivortex

pairs with a separation less than a distance $\pi/\tilde{k}_l$, which for our chosen parameters is $\approx 2.708\mu$m. However, such extremely close vortex-antivortex pairs do not affect the spatial correlations of the field at large distances.

4.3.1 Mean-field simulation.

As we discussed in the section 3 the properties of OPO are well described in mean-field approximation. These solutions are dynamically stable so that the mean-field solution provides accurate predictions for the coherent part of the equation (4.2), and therefore emission from microcavity, e.g., positions of signal and idler, *figure for mean-field vs stochastics*. At mean-field level, parametric processes lock the sum of the phases of signal and idler fields $\psi_{s,i}$ to that of the external pump, while allowing a global $U(1)$ gauge symmetry for their phase difference to be spontaneously broken into the OPO phase — a feature which implies the appearance of a Goldstone mode [116].

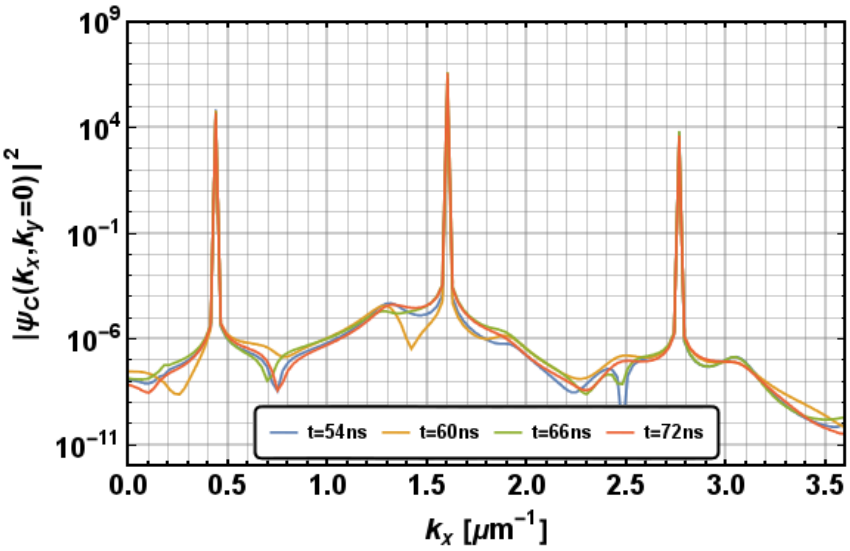

Figure 4.3: Mean-field steady state: convergence in time.

In this work, the mean-field prediction for the threshold pump power f_p^{th} will be used as a guideline in the choice of pump powers to be used in the numerical calculations and the mean-field steady states are used as initial states of stochastic

evolutions. The mean-field onset of OPO is shown in the inset of Fig. 4.4, where the mean-field densities of both pump and signal are plotted as a function of the increasing pump power f_p.

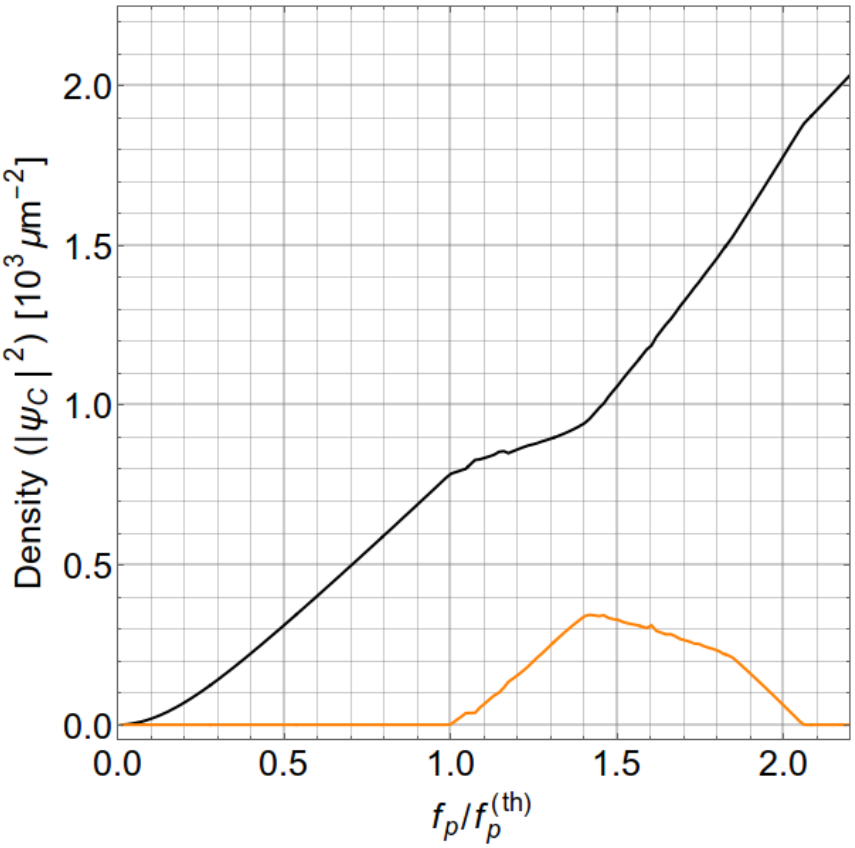

Figure 4.4: OPO in MF regime

4.3.2 Wigner simulation.

In order to study the system across the phase-transition, where phase fluctuations can be large, we need to go much beyond the mean-field and second order expansion [*cite*], which has also shown to be not sufficient by the RG analysis [118], and be able to include arbitrary large phase fluctuations and topological defects. We make use of the phase-space techniques, originally developed in the quantum optical context [102, 119] and applied with success to quantum fluids of atoms and photons [82, 120]. Briefly, the idea is to represent the state of the quantum field as a probability distribution function on a suitable phase space (in this case the Wigner function) and

describe the time evolution of the field by a Fokker-Planck-like partial differential equation on a spatial grid [121]. The resulting equation for the probability distribution contains third order terms controlled by the parameters $g_{\rm x}/(\kappa_\ell dV)$, where dV is the lattice spacing. In the limit $g_{\rm x}/\kappa_\ell \ll dV$ we can truncate the equation at second order and represent as a stochastic partial differential equation [122]. For more detailed derivation see Chapter 3.9. Note, that the truncation is controlled by a small parameter, which is the ratio between the interaction strength g_X and the decay rate κ and thus, remarkably, the presence of loss and pump terms suppresses some of the difficulties of the truncated Wigner method encounter in the context of cold atoms and guarantees its accuracy [73]. Alternatively, equation (4.2) may be derived by constructing the Keldysh path integral for $H = H_S + H_{SB}$, integrating out the quadratic bath terms, and keeping only the RG relevant terms [118].

We reconstruct the steady-state Wigner distribution by letting the system evolve to its steady state under the monochromatic pump, and then taking a large number of independent noise realisations. The stochastic averages over the configurations of different functions of the fields provide the expectation value of the corresponding symmetrically ordered operators. In Figure 4.5 we show the signal, pump and idler modes in the spectrum $\psi(\omega, kx, ky = 0)$ as calculated by evolving equation (4.2) for a single stochastic path into its steady state and taking the Fourier transform in space and time once the steady state has been reached. We illustrate the emission filtered about the signal, pump and idler, showing that, although no vortices exist in the pump state, vortices are present in the signal and idler states. In the specific case illustrated we are in the vicinity of the OPO threshold and so the phase-locking between the signal and idler states is weak, hence the unequal numbers of vortices. Note, that the density of polaritons in the idler state is much smaller then in the signal and they experience the same level of noise, thus there is a much larger number of V-AV pairs in the idler in comparison to the signal.

The color map in this figure shows $|\tilde{\psi}_{\rm c}(\omega, k_x, k_y = 0)|^2$, i.e. the Fourier transform of the photon field, on a logarithmic scale. The color scale is artificially cut off to highlight some lower intensity features (otherwise the pump completely dominates), this makes the pump, signal and idler peaks appear broad in energy where they are, in reality, very narrow in both energy and momentum. The power of the pump is the only remaining free parameter with with we can probe the system. Having determined the threshold pump power for the onset of OPO, we vary the pump around

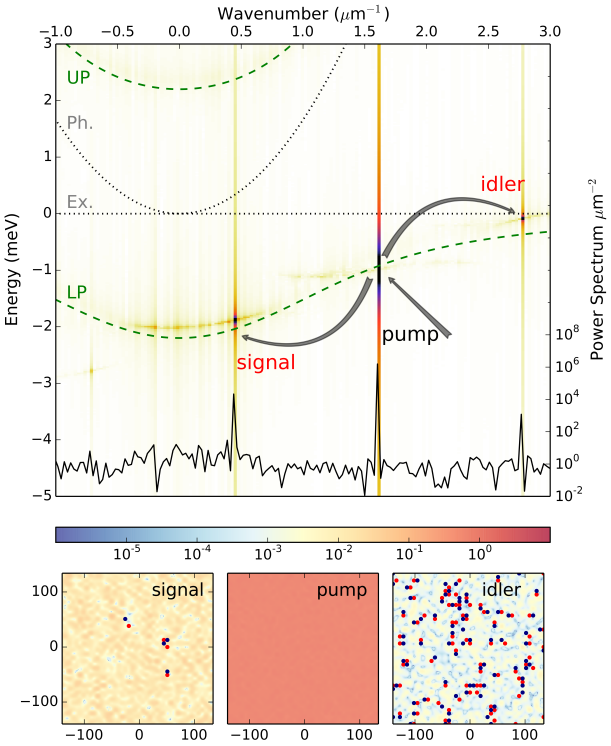

Figure 4.5: Above: Representative spectrum $|\tilde{\psi}(\omega, k_x, k_y = 0)|^2$ in the OPO regime taken from a stochastic simulation with a pump power $f_p = 1.02436 f_p^{\text{th}}$, where f_p^{th} is the mean-field OPO threshold, plotted on a logarithmic scale. Arrows show the incident pump modes being scattered into the signal and idler states. In the spectrum we observe a significant population of these states. The dashed green lines show the theoretical upper and lower polariton spectra and the dotted black lines show the spectra of the cavity photon and the exciton. The full black line shows the time-averaged power spectrum, $\langle|\tilde{\psi}(t, k_x, k_y = 0)|^2\rangle$, of the system, highlighting the strong occupation of the pump, signal and idler modes. Below: the intensities of the signal $|\tilde{\psi}_s(t, x, y)|^2$, pump $|\tilde{\psi}_p(t, x, y)|^2$ and idler $|\tilde{\psi}_i(t, x, y)|^2$ modes in this simulation taken at a representative time frame t. Occupations are shown with respect to the pump so that the maximum intensity of the pump mode is rescaled 1.0. Blue and red dots show vortices and anti-vortices respectively.

this value to investigate the nature of the transition. All results are averaged over 96 stochastic realizations, this number (see supplementary material) having been seen to be sufficient to ensure reasonable convergence of the measured quantities.

In order to rule out any dependence on the chosen initial conditions, we have considered four extremely different cases: empty cavity with random noise initial conditions and adiabatic increase of the external pump power strength; mean-field condensate initial conditions; either random or mean-field initial conditions in the presence of an unpumped region at the edges of the numerical box, so to model a sort of vortex-antivortex reservoir. In the bellow the different initial state dynamics, and their physical interpretation for each of these four different initial conditions, are carefully described; in all four cases we always reach the very same steady-state regime, i.e., all noise averaged observable quantities discussed in the following lead to the same result — this could not be a priori assumed for a non-linear system.

Number of stochastic realisations

The realisation-averaged results presented in the this chapter have been averaged over 96 realisations taken from independent stochastic paths as we assessed this to be sufficiently many to give a reliably converged result. In Fig. 4.6 we show the first order correlation function $g^{(1)}(x)$ for $f_p = 1.017 f_p^{\mathrm{th}}$, averaged over different numbers of realisations (96, 192, 288, 384 and 480). We conclude that 96 is sufficient to determine the nature of the correlations. Furthermore, the average number of vortices also does not change significantly (no more than ± 0.5) beyond 96 realisations, and so this number is sufficient to ensure consistent results in both the smooth and topological sectors of the model.

Convergence in time to a steady state

In order to assess when a time evolution has reached its steady state we consider the average (over realisations) of both the signal density, $|\psi_{\mathrm{s}}|^2$, and the number of vortices. In Figs. 4.7 and 4.8 we show the evolution of these quantities toward a steady state, assuming the initial condition wherein the system is allowed to reach its mean field steady state (at time $t = 0$) and stochastic processes are adiabatically switched on. In practice this means that the noise terms are multiplied by a ramp function

$$r(t) = \frac{1}{2}\left[\tanh\left(\frac{t - t_0}{t_r}\right) + 1\right]$$

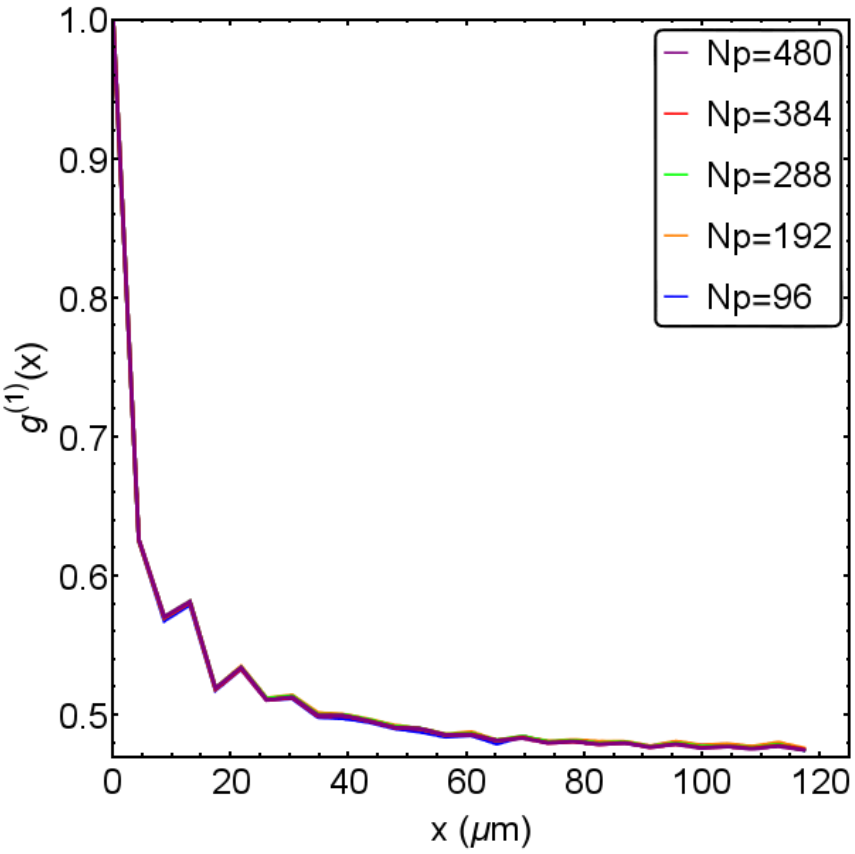

Figure 4.6: The strength of the pump is fixed at $f_p = 1.017 f_p^{\text{th}}$, and each simulation is run well into the steady state. We calculate the correlation function averaged over 96, 192, 288, 384 and 480 realisations and observe no significant improvement in the convergence past 96 realisations.

such that the noise is slowly increases from 0, achieving half its maximum at t_0, at a rate determined by t_r. For the empty cavity with noise initial condition, in which the pump is adiabatically increased, it is the pump term that is multiplied by this ramp function. We choose $t_0 = 450$ps and $t_r = 150$ps as these prove to give a fairly rapid convergence to the steady state. It is, however, important to note that the steady state is unique and does not depend upon the specific values of t_0 and t_r we choose nor on the initial conditions, which we start the dynamics from. In all cases the steady state is reached within around twenty nanoseconds. The slowest convergence occurs in the vicinity of the BKT transition. This critical slowing of the dynamics is to be anticipated given the divergence of the correlation length as the transition is approached.

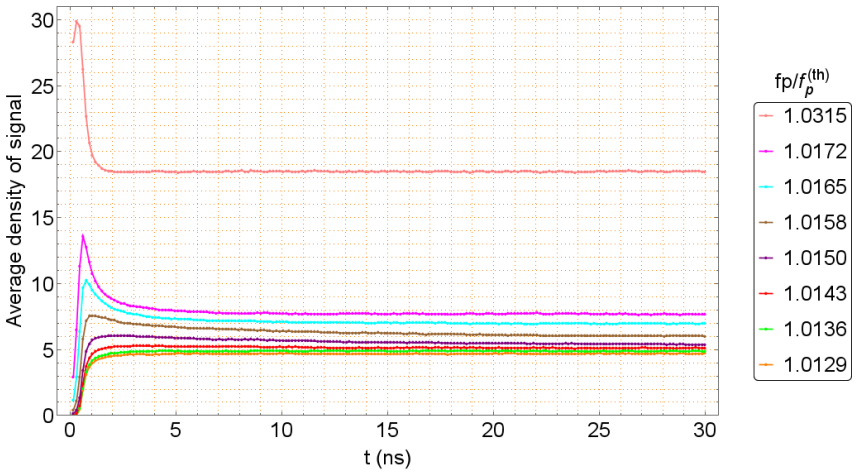

Figure 4.7: Here we show $|\psi_s|^2$ evolving in time for a range of pump powers. The initial jump in the signal occupation is induced by the introduction of stochastic processes, and dies away as the system resolves toward its non-equilibrium steady state.

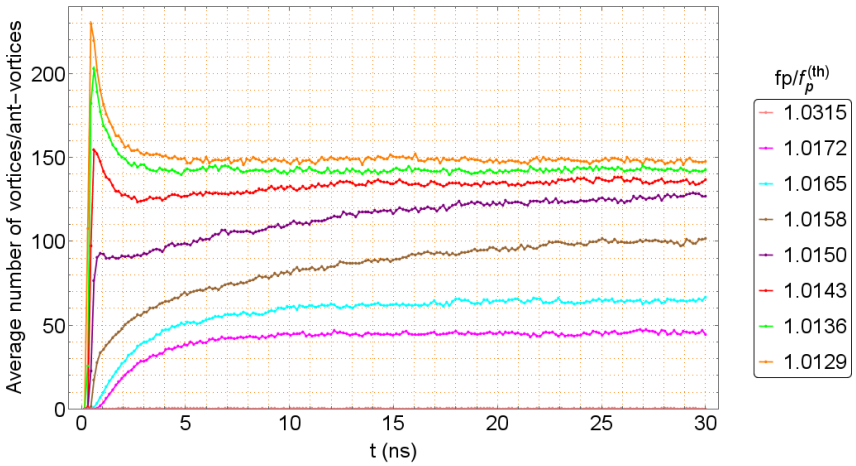

Figure 4.8: Here we show the average number of vortices in the system evolving in time for a range of pump powers. The introduction of stochastic processes increases the number of vortices (which is always zero in the spatially homogeneous mean field steady-state), which then evolves toward its steady state value through pair creation and annihilation events.

Realisations from independent stochastic paths vs. independent time snapshots in a single path

In Fig. 4.9 we show the number of vortices for a broad range of pump powers across the transition averaged over realisations taken from independent stochastic paths

(red dots) and from multiple snapshots over time (blue dots) once the steady-state is reached. Averaging over time within the steady state is a less numerically intensive approach, and shows an excellent agreement with the average over realisations even in the critical region. In practice, averaging over time is computationally efficient away from the critical region, where the steady state is reached quickly and memory is quickly lost during the time evolution. Around the critical region it takes a significant time to reach a steady state and then to decorrelate the snapshots, so averaging over stochastic paths becomes more computationally effective.

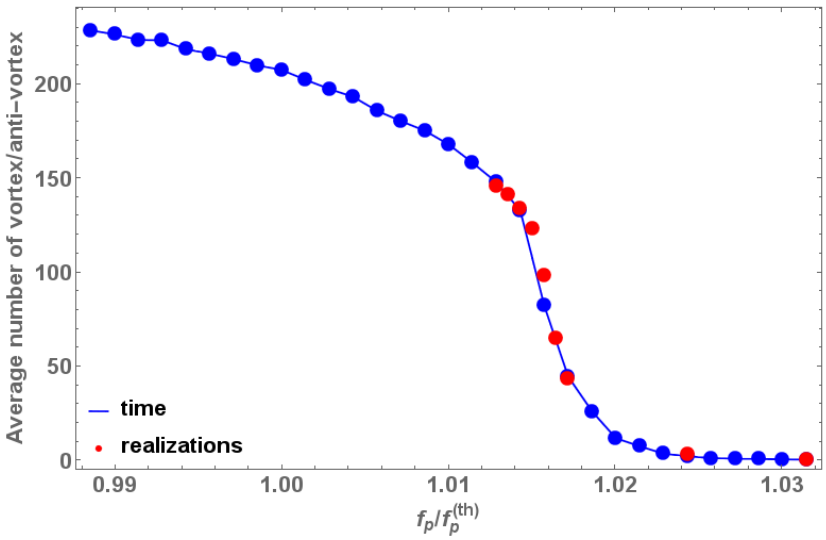

Figure 4.9: The red dots show number of vortices averaged over many stochastic paths. The blue dots show the number of vortices averaged over the final 500 frames, running from 15ns to 30ns, of a single stochastic path, once the system has converged to a steady state. We observe an excellent agreement between these two approaches and so away from the critical region we can consider the (less numerically intensive) average over time.

Dependence on different initial conditions

We have investigated a number of physically diverse initial conditions in order to rule out dependence of the final steady state on the starting configuration. To initiate our simulations we either adiabatically increase the pump strength atop a white noise background or adiabatically increase the strength of the stochastic terms starting from the mean field steady state. We also wish to eliminate the possible effects of trapped vortices, and so in addition to simulations with a uniform pump region we

have performed simulations, where a small strip around the numerical integration box is left un-pumped so as to act as a source/sink for vortices. The four distinct initial conditions we consider are therefore those classified in the following table:

	Increasing Pump	Increasing Noise
No Reservoir	Scheme A	Scheme B
Reservoir	Scheme D	Scheme C

In schemes A and D, there are initially very many vortices, which then proceed to annihilate with one another so that the overall vorticity tends to decrease toward the steady state. In schemes B and C there are no vortices at the outset but as stochastic processes shake the system the vorticity increases toward the steady state. Therefore even before the true steady state is reached, we can treat schemes A and D as upper bounds for the vorticity and schemes B and C as lower bounds. In schemes C and D we incorporate a reservoir (region with no drive and thus of very low density) of width 34.72nm along the two sides of the numerical integration box parallel to k_p, which we then exclude from calculations of the vorticity, signal density, and correlations. The width of the reservoir does not change the result except in that it needs to be wide enough that the condensate has room to decay away to zero.

In Figure 4.10 we show the evolution towards the steady state for all four of these schemes with a pump power $f_p = 1.017 f_p^{\mathrm{th}}$. We plot the vortex density (top panel) as well as dynamics of vortices (bottom panel, where blue and red dots show positions of V and AV cores) for each scheme (A, B, C and D starting from the left). We see that every scheme converges fairly rapidly towards the same steady state. From the animations it is evident that the vortices always appear in pairs but that these pairs are not always tightly bound. It was not a priori obvious that all four schemes should lead to the same steady state but we take this as evidence that the physical process leading to the steady state is universal for this system. We observe that the schemes incorporating an empty reservoir converge more quickly to the steady state than their counterparts without a reservoir. Nevertheless we present data for scheme B because the reservoirs have no counterpart in the traditional BKT transition to which we wish to compare our results.

4.3.3 Vortex unbinding.

Vortices are counted by summing the phase difference, modulo 2π, along each link around every elementary plaquette on the filtered grid. In the absence of a topologi-

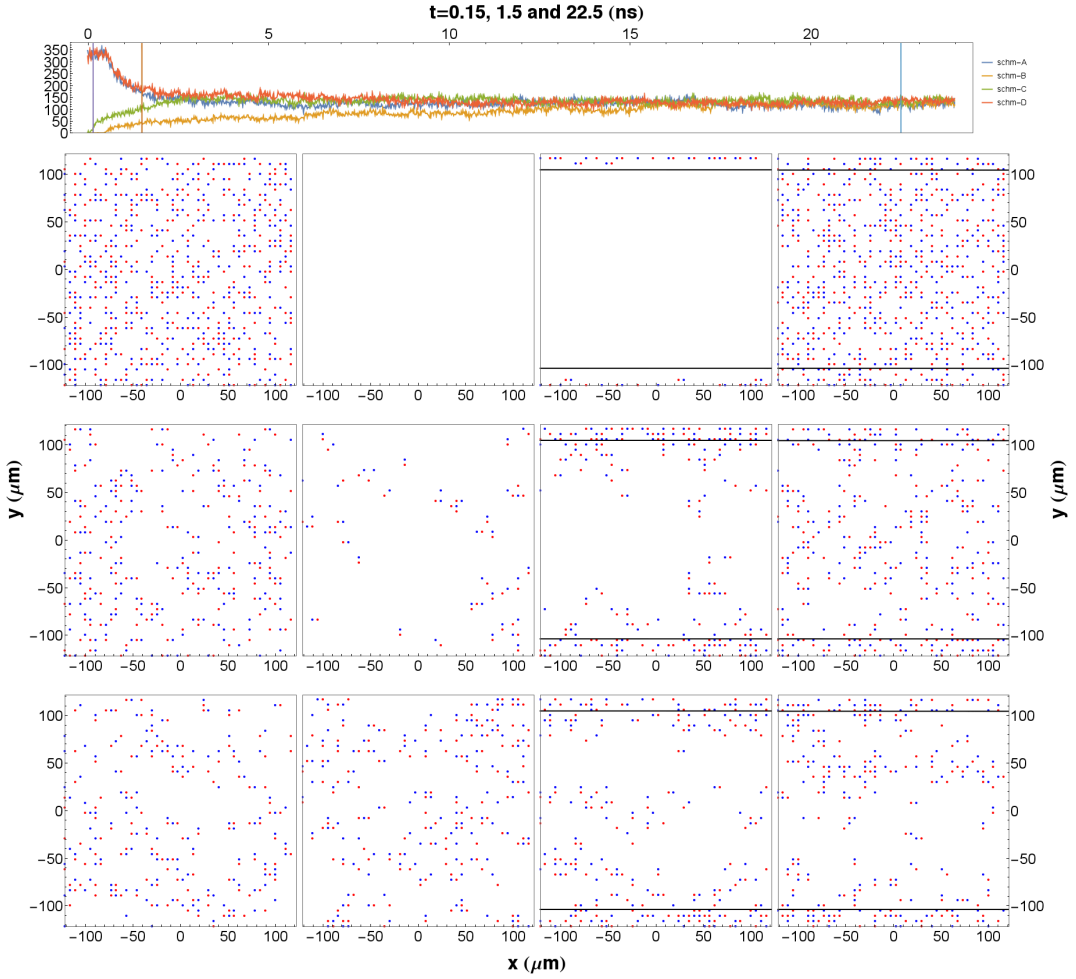

Figure 4.10: The strength of the pump is fixed at $f_p = 1.017 f_p^{\text{th}}$, and each simulation is run well into the steady state. We calculate the correlation function averaged over 96, 192, 288, 384 and 480 realisations and observe no significant improvement in the convergence past 96 realisations.

cal defect this sum will be zero, if the sum is 2π we determine there to be a vortex at the center of that plaquette, if the sum is -2π we count an anti-vortex. The number of vortices is averaged over each stochastic path and we consider the average number of vortices to be converged in time when its variation is less the 5%. It is by no means *a priori* obvious that these four initial conditions should lead to the same steady state and so we are very fortunate that they all converge to the same value for every observable we consider. (This is discussed further in the supplementary information).

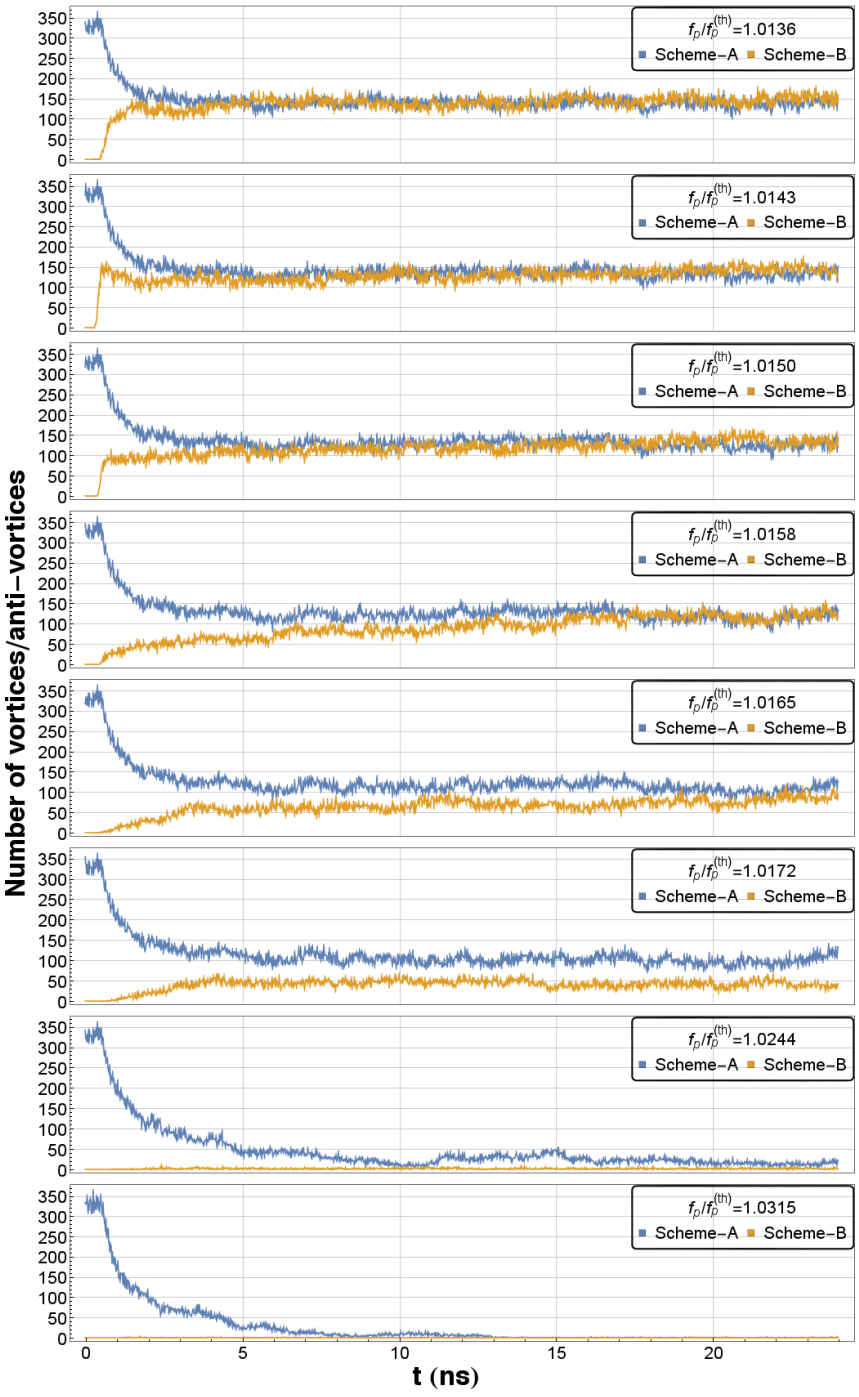

Figure 4.11: The numerical convergence on different grids.

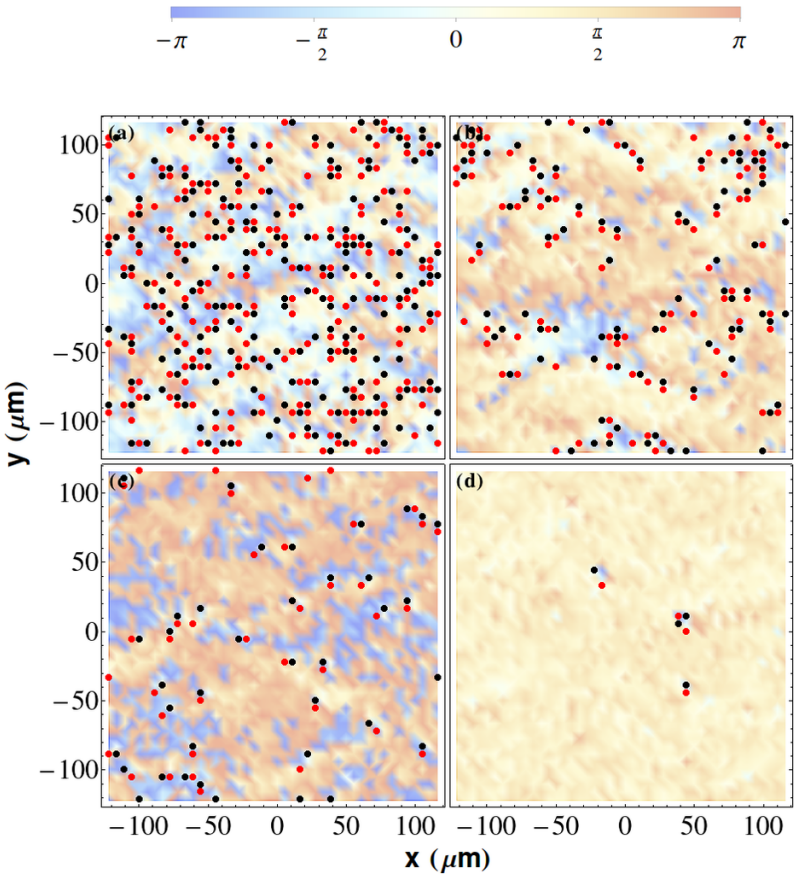

Figure 4.12: The phase of the signal (color-map) and the vortices and anti-vortices seen therein (blue and red dots respectively) for pump powers: (a) $f_p = 1.00287 f_p^{\rm th}$, (b) $f_p = 1.01648 f_p^{\rm th}$, (c) $f_p = 1.01719 f_p^{\rm th}$, and (d) $f_p = 1.02436 f_p^{\rm th}$; where $f_p^{\rm th}$ is the mean field OPO threshold. Between these values we observe the number of vortices decreasing dramatically and the distance between them increasing, indicating the presence of a vortex unbinding transition. These sample data are taken at a late stage in the dynamics, once the system has reached its steady state for a given pump strength.

For the most part we consider only quantities which are averaged over may realizations, however at a single shot level (and only at a single shot level) we can observe vortices in the phase of $\psi_{\rm s}$. In Figure 4.12 we show four representative examples of the vortices in the signal for different pump powers chosen to straddle the OPO threshold. Each frame shows a snapshot of the system after the steady-state in the averaged data has been reached for different strength of the drive. Here already we can see a qualitative change with increasing pump power: from a dense "plasma"

of vortices and antivortices at low powers to few vortex-antivortex pairs at larger powers, to eventually a complete luck of any vorticity in the system (not shown).

By varying the power of the pump whilst keeping all other parameters fixed, we are able to construct a phase diagram of the OPO system. In the first instance we consider the the intensity of the signal (see Figure 4.13), as a point of comparison we also show the intensity as calculated in the mean field approximation. At the threshold pump power the signal is "switched on" with the intensity of the signal in the mean field approximation jumping from zero to some finite value, i.e. a condensate forms. We observe that the mean-field transition from the normal state to the OPO condensate is shifted and smoothed by the introduction of fluctuations. Pursuing the analogy with the equilibrium BKT transition, we investigate the number of vortices present in the signal. We observe a steep drop in the number of vortices associated with the OPO transition.

We also consider the distance between nearest neighbouring vortices of the same and opposite winding number. For each vortex we measure the distance to the nearest vortex, r_{VV}, and the nearest anti-vortex, r_{VA}, likewise for each anti-vortex we measure the distance to the nearest anti-vortex, r_{AA} and vortex r_{AV}, averaging over individual vortices and stochastic realizations, the symmetrized ratio $b = \left\langle \frac{r_{VV}+r_{AA}}{r_{VA}+r_{AV}} \right\rangle$ gives us an intuitive measure of vortex unbinding as we will have $b \to 1$ for an unbound vortex plasma and $b \to 0$ when the vortices form tightly bound pairs. We observe a dramatic drop in b at the OPO transition, indicating that the vortices are indeed binding.

It is worth noting that the crossover region displayed in Figure 4.13 is very narrow indeed, to highlight this we include as an inset the phase diagram calculated in the mean field approximation to show just how small the region around threshold we are here studying is. This explains why experimental studies have had such difficulty in investigating the power law decay of correlation functions in this system [123, 124]. In the experiment, however, we expect this region to be somewhat additionally broaden by fluctuations due to imperfection of the pumping laser.

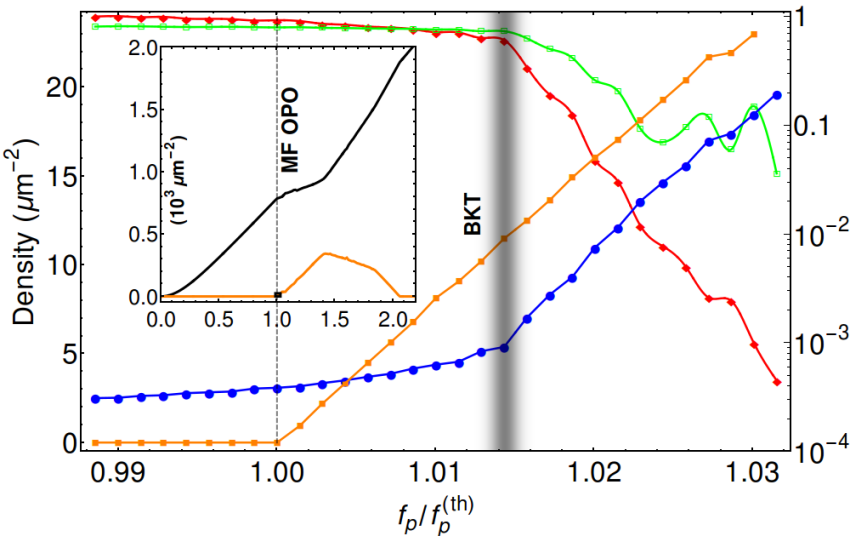

Figure 4.13: The orange lines in main and inset show the mean-field density of the signal. The blue line is total signal density in stochastic approach. The red line is average number of vortices in signal rescaled by its maximum value, $N_{\max} = 222.8$. The green line is ratio of average distances between nearest neighbouring vortex-vortex and vortex-anti-vortex pairs. The gray dashed and solid (but very thick and transparent) vertical lines are demarcate the OPO mean-field and BKT transitions respectively. Inset: The mean-field phase diagram. The tiny rectangle near to $f_p/f_p^{\text{th}} = 1.0$ represents the region of the main figure. The black line here shows the occupation of the pump state. The pump powers in horizontal axes are normalized by f_p^{th} and signal densities rescaled by $10^3 \mu m^{-2}$.

4.3.4 Spatial correlation function

The correlation function which is of interest to us in analysing the BKT transition is the (normalized) first-order correlation function

$$g_s^{(1)}(\mathbf{r}) = \frac{\langle \psi_s^*(\mathbf{r}+\mathbf{R})\psi_s(\mathbf{R})\rangle}{\sqrt{\langle \psi_s^*(\mathbf{r})\psi_s(\mathbf{r})\rangle \langle \psi_s^*(\mathbf{r}+\mathbf{R})\psi_s(\mathbf{r}+\mathbf{R})\rangle}} \tag{4.6}$$

where the subscript s on the field denotes that this is filtered around the signal. The averaging denoted by $\langle \dots \rangle$ is taken over both the set of stochastic paths being sampled and the auxiliary coordinate $\mathbf{R}$. This is essentially the noise-averaged autocorrelation function of the filtered field ψ_s and can be computed efficiently in $\mathbf{k}-$space. When the signal is strong, the density fluctuations will, on average, be

weak so we can write $\psi_s(\mathbf{r}) = \sqrt{\rho_0 + \delta\rho(\mathbf{r})}\exp i\varphi(\mathbf{r})$ and see that

$$g_s^{(1)}(\mathbf{r}) \sim \left\langle e^{i\varphi(\mathbf{r})}e^{-i\varphi(\mathbf{r}+\mathbf{R})}\right\rangle + \mathcal{O}(\delta\rho/\rho_0)$$

which highlights the connection to the classical BKT transition. Indeed either the filtered field ψ_s or its normalized counterpart $\exp i\varphi$ can be used the calculate the $g^{(1)}$ with only minor numerical discrepancies, for completeness we opt to work with ψ_s. The ordering transition can be seen within $g^{(1)}$ as a crossover in the long-distance behaviour between a exponential decay, $g^{(1)}(\mathbf{r}) \sim e^{-r/\xi}$, in the disorder phase, and algebraic decay $g^{(1)}(\mathbf{r}) \sim (r/r_0)^{-\alpha}$ in the (quasi-)ordered phase. We therefore attempt to fit the tail of the calculated correlation function to both of these functional forms. Next we consider the first order spatial correlations of the field, averaged over all realisations of the noise. The behaviour of the first order correlation function $g^{(1)}(x)$, whether it decays as an exponential or as a power law, is determined by fitting the tail of the data to each functional form and taking the better fit of the two. The fitting is illustrated in Fig. 4.14. For pump powers close but above the critical region it is clear that the power-law fits the data better (which is also confirmed by a larger correlation coefficient), while below the critical region the exponential fit is closer to the data. For stronger pump powers, away from the transition, $g^{(1)}(x)$ is practically constant on these length-scales (as reported in experiments and discussed in the main text).

As shown in figure 4.15, we observe a crossover in the long distance behaviour of the signal's spatial correlation function, coinciding with the OPO threshold, between exponential and algebraic decay. In contradiction with the equilibrium BKT transition, but in agreement with previous experimental observations [112], we see that the exponent in the algebraic decay in the correlated regime can exceed the upper value of 1/4. For example, for a pump power of 1.0136 times the mean field threshold, which is just within the ordered regime, has an exponent of 1.23. Note that in experiments of Roumpos and Yamamoto exponents in the range $0.9 - 1.2$ has been observed.

In calculating the correlation functions, as in calculating the number of vortices, we need to allow the evolution of the system to progress long enough that a steady state is reached. To assess whether the system has reached a steady state we cal-

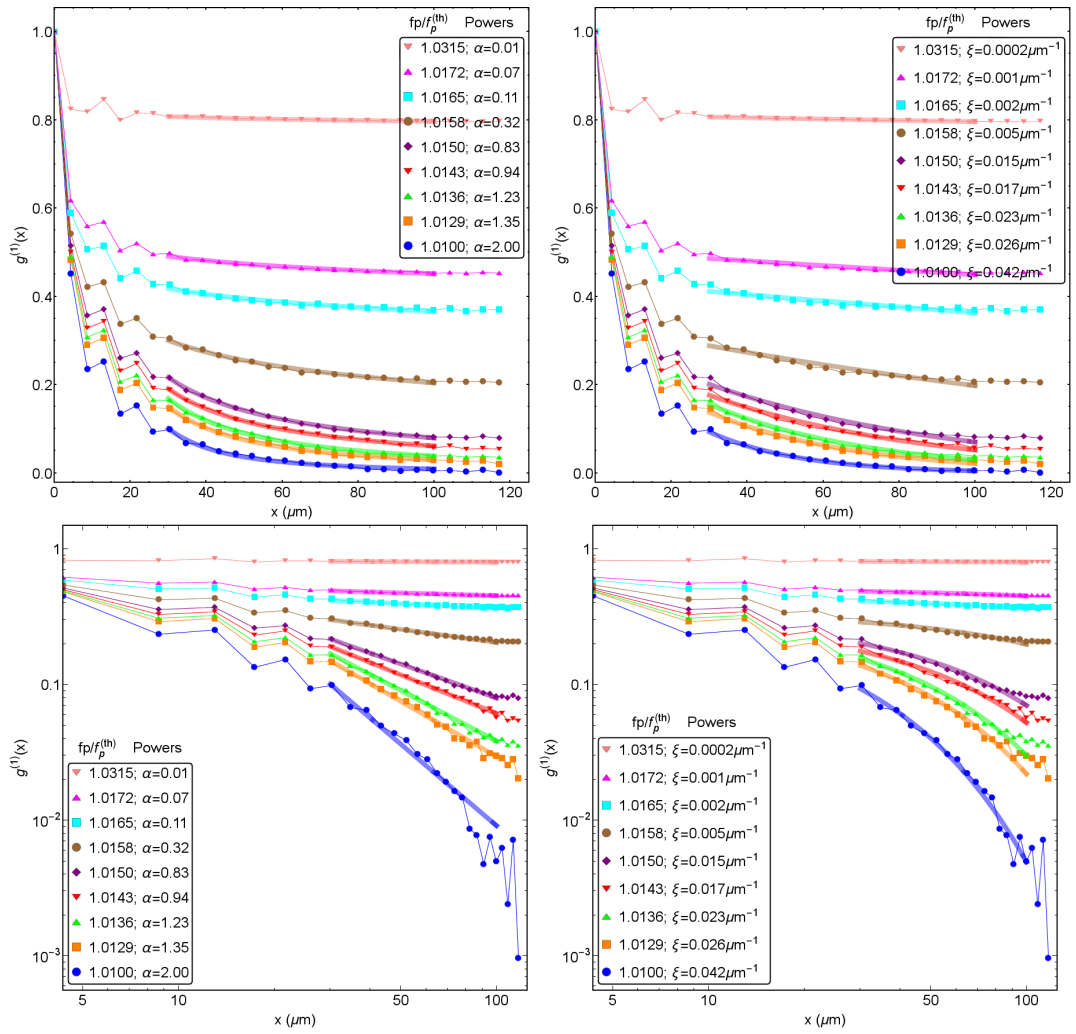

Figure 4.14: Here we show both the algebraic (left) and exponential (right) fits to the correlation function on a full linear scale (above) and on an exponential scale (below). The fitting to the data is taken over the range $30\mu\text{m} < x < 100\mu\text{m}$. This domain needs to avoid both the region close to origin with short-range correlations and the edges, where the behaviour might be influenced by periodic boundary conditions.

culate observable quantities and wait until there is no longer a significant variation. One observation which came out of this procedure is that the convergence in the vorticity is much quicker than that in the correlation exponent. We can interpret this as indicating that the fluctuations due to external drive and decay preferentially affect the collective excitations above topological excitations making the vortex sector more dynamically stable. Also in the near vicinity of the transition, the convergence

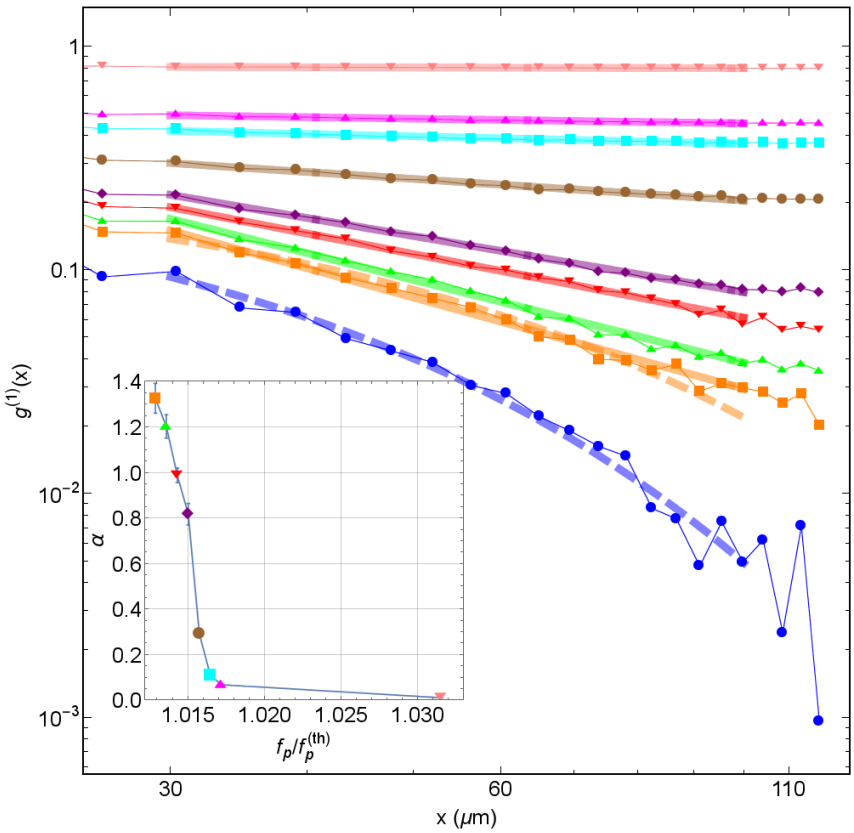

Figure 4.15: Main panel: Long-range spatial dependence of $g^{(1)}(\mathbf{r})$ for different pump powers $f_p/f_p^{\rm th}$ close to the mean-field pump threshold (the symbols are the same ones as in the inset and correspond to the same values of $f_p/f_p^{\rm th}$). Thick solid (thick dashed) lines are power-law (exponential) fitting, from which values of the exponent α are derived. The $f_p/f_p^{\rm th} = 1.0129$ case (orange squares) is a marginal case where both algebraic and exponential fits apply almost equally well, signalling the BKT transition region. Inset: Power-law algebraic decay exponent α for different pump powers $f_p/f_p^{\rm th}$; error bars are standard deviations of the time-average.

in both the correlation functions and the vortices is dramatically slowed down. This critical slowing is a common feature of dynamical phase transitions.

Chapter 5

Conclusions and future works

In this chapter, we present a brief summary of the conclusions for this dissertation and briefly report ongoing works related to the our findings.

5.1 Summary

In this dissertation by considering microcavity polaritons in the optical parametric oscillator regime as the prototype of a driven-dissipative system, and using methods able to account for large fluctuations and topological defects, we have shown that a mechanism analogous to the BKT transition, which governs the equilibrium phase transitions in two dimensions, occurs out of equilibrium for a driven-dissipative system of experimentally realistic size. Notwithstanding the novelty and significance of this result, there are a number of novel features which warrant special discussion as they are peculiar to the non-equilibrium phase transition. We have shown that the exponent of algebraic decay in the quasi-long-range ordered phase exceeds what would be attainable in equilibrium. This recovers a recent observation [123], and strongly suggests that indeed a non-equilibrium BKT may have been seen there. Moreover, our findings imply that before topological defects destroy the order, the quasi-ordered phase can somehow sustain a higher level of smooth collective excitations in a dissipative-driven non-equilibrium system than in thermal equilibrium scenario. There are several open questions which stem from our work: Is there a non-equilibrium universal upper bound for the α exponent? What would it depend on and would it smoothly connect to the equilibrium case?

Although for realistic experimental conditions, we have found that the region for BKT physics, before the pump power is strong enough to induce perfect spatial

coherence over the entire system size, is indeed narrow, we believe our work will encourage further experimental investigations in the direction of studying the non-equilibrium BKT phenomena. Even though the small size of the critical region has so far hindered its direct experimental study, our calculations indicate that the macroscopic coherence observed in past polariton experiments [1, 9, 10, 73, 80, 124, 125] results from a non-equilibrium phase transition of the BKT rather than the BEC kind.

5.2 Other projects related to the outcome of the thesis

5.2.1 Coherence properties of extended 2D polariton condensates

The recent experimental studies in the OPO regime [124] experienced noticeable difficulties in investigating the power-law decay of the first-order correlation function across the transition. We do indeed find that the pump strength interval over which power-law decay can be clearly seen is extremely small, and the system quickly enters a regime where coherence extends over the entire system size, as measured in Ref. [124]. Therefore, in order to clearly observe power-law decay one has to go close to threshold and need larger systems.

Our experimental collaborators at Nanotechnology Institute, CNR, Lecce (Italy) attempted to perform the corresponding experiment of the thesis results. Unfortunately, they have faced experimental difficulties for both approaches, e.g., in the experiment it is difficult to have spatially "large" condensates in OPO regime since first the space-energy mode fragmentation and second the influence of the pump laser effects. Also, it is very challenging to explore close to the threshold since density grows too fast.

Because of this difficulties in experiment we have decided to give up from OPO regime and implemented incoherently pumped scheme. With in this scheme we are able to get large enough spot in experiment, see Figure 5.1, and got similar power-law decays in both experiment and numerical simulation with phenomenological model. This is on going project and we have only so preliminary results at the moment.

5.2.2 Multi-component quasi-condensates

In order to analyse the quasi-condensate at signal mode, we have filtered the full emission, full photonic component, in such a way that signal component is singled out. However, there are four such quasi-condensates, namely at signal and idler

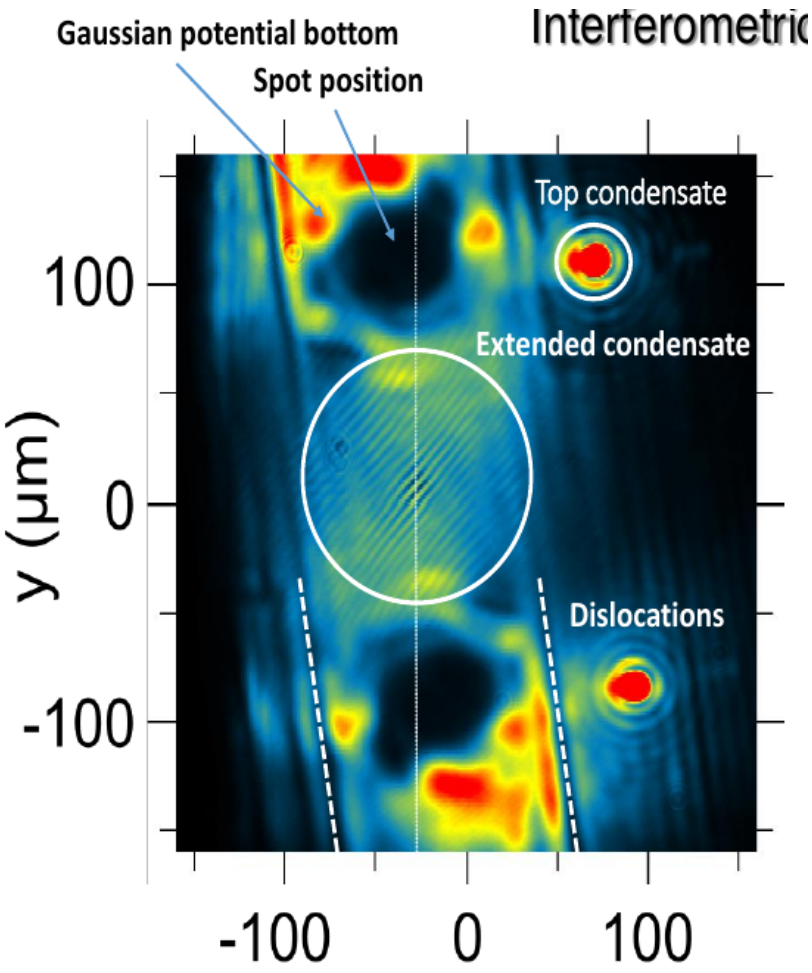

Figure 5.1: Extended condensate in incoherently excited polaritons.

modes of each photonic and excitonic components. Therefore, it is interesting to know that results of this thesis would be same or not for all these four components, in other words, are these components independ from each other or have some correlations. This is not easy question to answer intuitively since on the one hand signal and idler phases are locked in the mean field level but on the other hand, density of idler is much weaker than the signal so the fluctuations easily break the perfect phase locking between them which results more vortices in idler than signal.
Our analyses shows that, see Figure 5.2, the phase transition occur exactly at same point, have same threshold, for all components. For a completeness, we have performed same analyse for upper OPO threshold.

Interestingly, despite of different coherence overall we found that spatial cor-

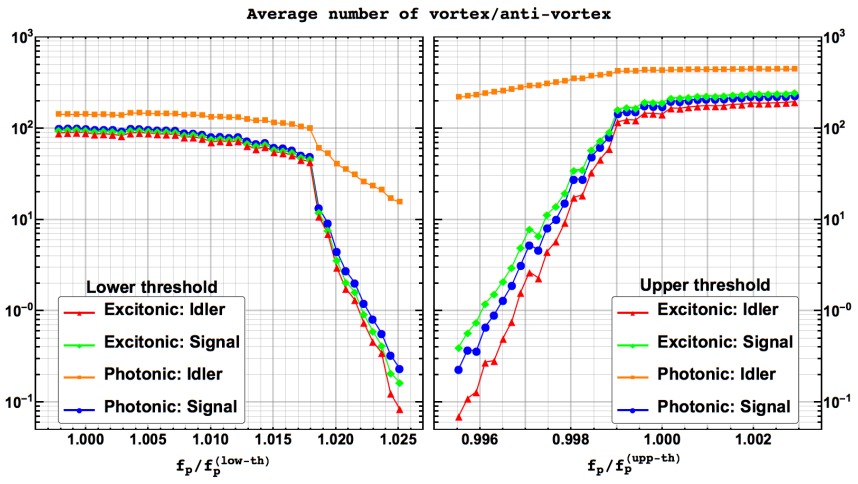

Figure 5.2: Average number of vortice across the phase transition. *Left*: accross lower OPO threshold. *Right*: accross upper OPO threshold.

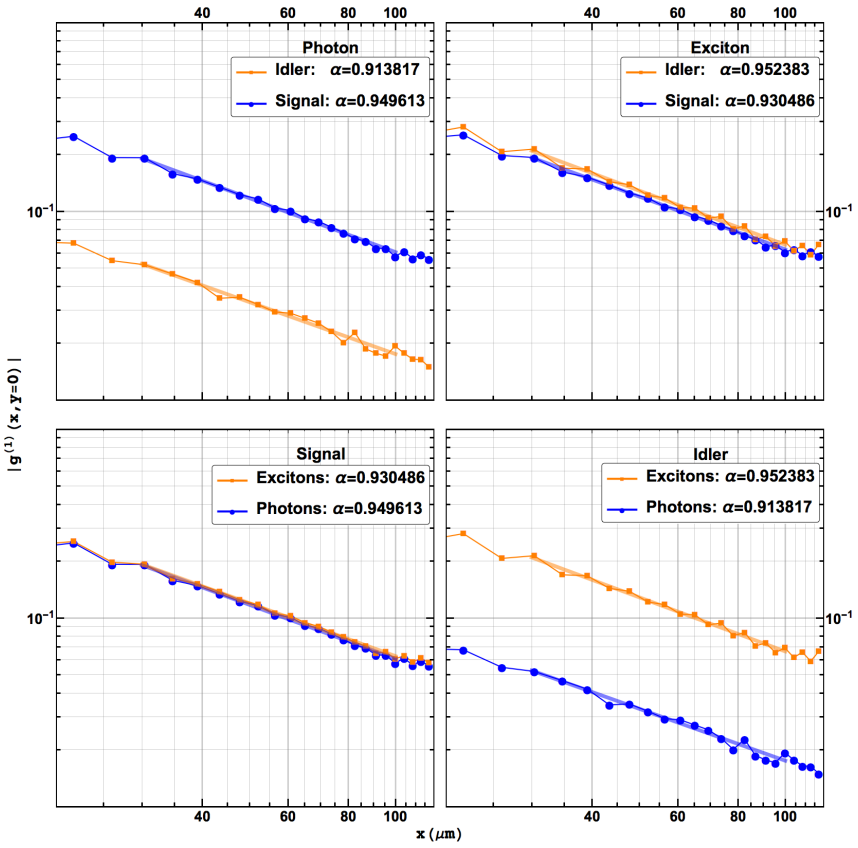

Figure 5.3: First order spatial correlation function of the four components.

relation functions have similar power of power-law decay for the four components, see 5.3.

5.2.3 Vortex and half-vortex dynamics in a nonlinear spinor quantum fluid

As mentioned in section 3.2.3 polariton spin could be ± 1 so have two-component spin structure, spinor. Therefore, the important question is which type of vortex is responsible for the BKT type of phase transition which we seen in this thesis, full-vortex or half-vortex? For what does mean by full- and half-vortex, see Figure 5.4.

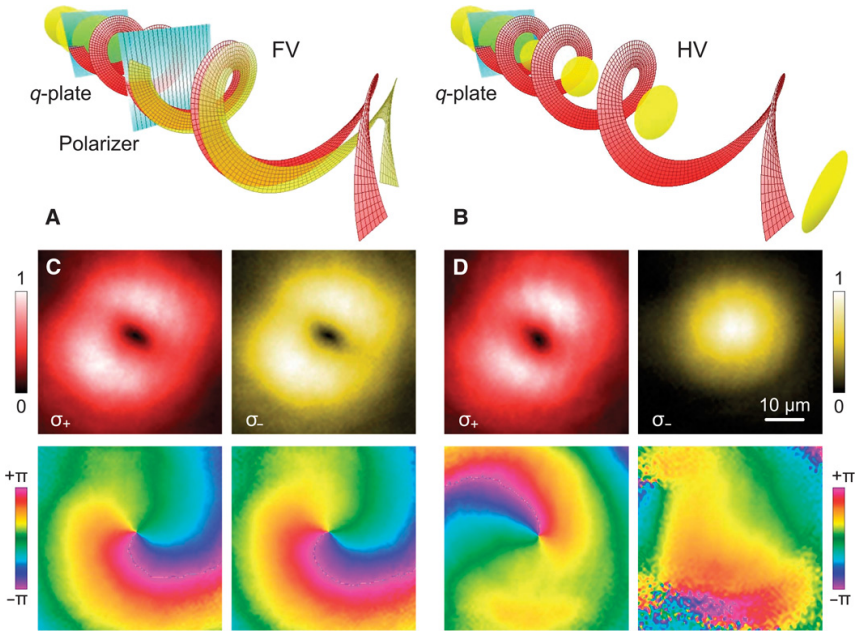

Figure 5.4: *Left*: Full vortex - vortex in each circular polarizations. *Right* half vortex - vortex in only one circular polarization, such that in the linear polarization basis, they have a half-integer winding number for both the phase and field direction.

First step to answer the above question was stability of hydrodynamic vortex in polariton fluids and results are published in

- L. Dominici, G. Dagvadorj, J. M. Fellows, D. Ballarini, M. De Giorgi, F. M. Marchetti, B. Piccirillo, L. Marrucci, A. Bramati, 6 G. Gigli, M. H. Szymaska, D. Sanvitto, Vortex and half-vortex dynamics in a nonlinear spinor quantum fluid, Science Advances, 2015;1:e1500807, January 2016

5.2.4 Spinor polariton quasi-condensate

More sophisticated approach to answer the question is perform similar simulation as we did in the thesis but including the splitting between TE and TM:

$$i\hbar d\phi_\pm = \left\{ \left[-i\kappa_\phi + g\left(|\phi_\pm|^2 - \frac{1}{dV} \right) \right] \phi_\pm + \frac{\hbar\Omega_R}{2}\psi_\pm + \alpha|\phi_\mp|^2\phi_\pm \right\} dt + i\hbar\sqrt{\frac{\kappa_\phi}{2\hbar dV}}dW_\pm^\phi \tag{5.1}$$

$$i\hbar d\psi_\pm = \left\{ \left(-\frac{\hbar^2}{2m_\psi}\nabla^2 - i\kappa_\psi \right) \psi_\pm + \frac{\hbar\Omega_R}{2}\phi_\pm + \beta\left(\frac{\partial}{\partial x} \mp i\frac{\partial}{\partial y} \right) \psi_\mp + F_\pm \right\} dt + i\hbar\sqrt{\frac{\kappa_\psi}{2\hbar dV}}dW_\pm^\psi \,,$$

From our simulation, we concluded the half-vortices are the elementary excitation so responsible for the BKT type of phase transition in polariton fluids, see Figure 5.5.

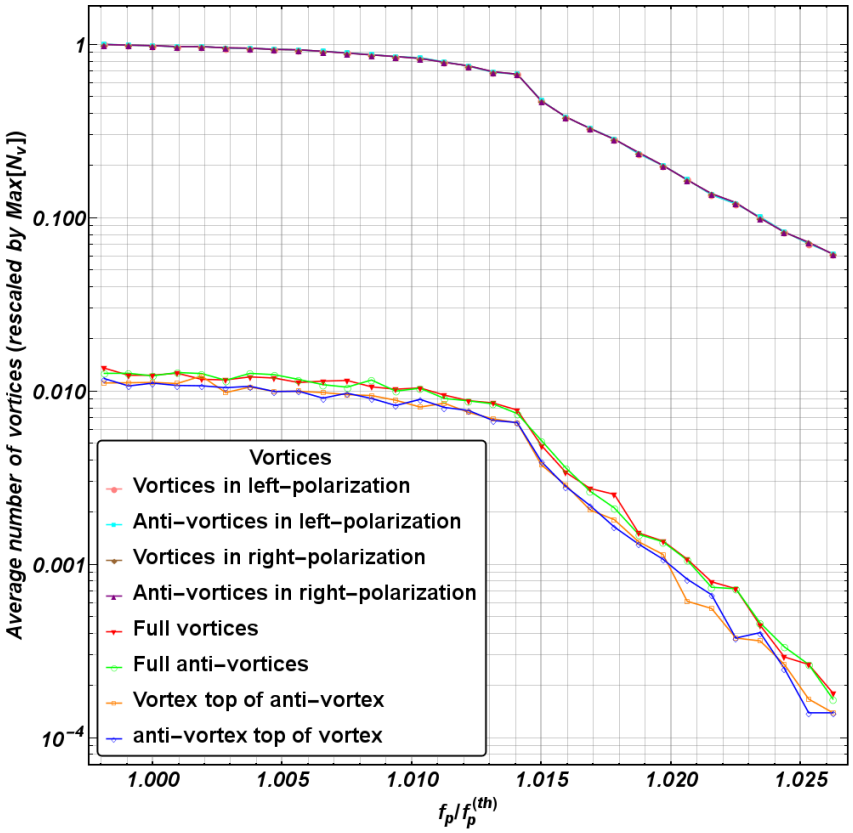

Figure 5.5: Average number of full- and half-vortices accross the phase transition.

5.2.5 Phase ordering dynamics

An other interesting dynamics is phase ordering dynamics. We quench the system infinitely fast from the disorder phase to the ordered phase where the final steady state is free of vortex.

After infinitely fast quench we record number of vortices and how coherence establishing in time from which we get the characteristic lengths L(t), see Figure 5.6.

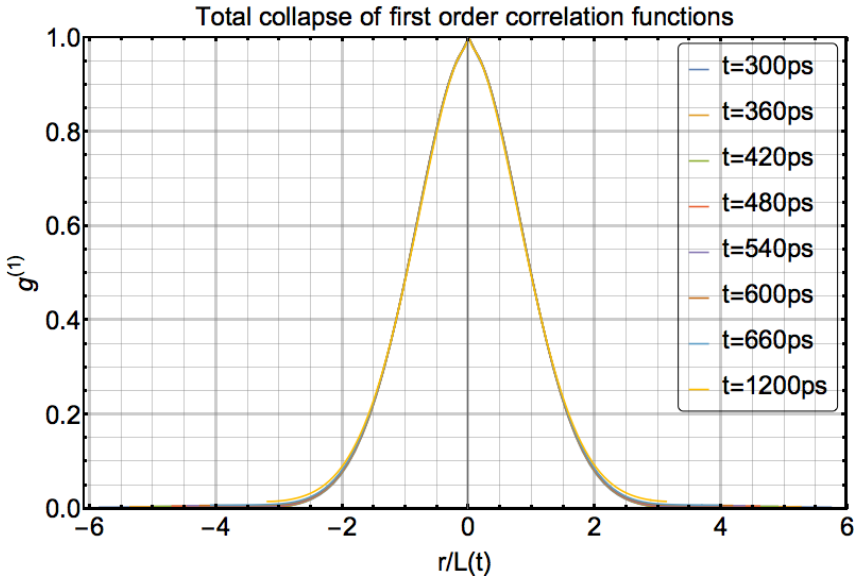

Figure 5.6: Collapse of spatial correlation function at different time moment.

In the correlation function collapsed region system well exhibit the XY model which has logarithmic correction to the diffusive law.

From both characteristic lengths and number of vortices we got dynamical critical exponent z=2, see Figure 5.7.

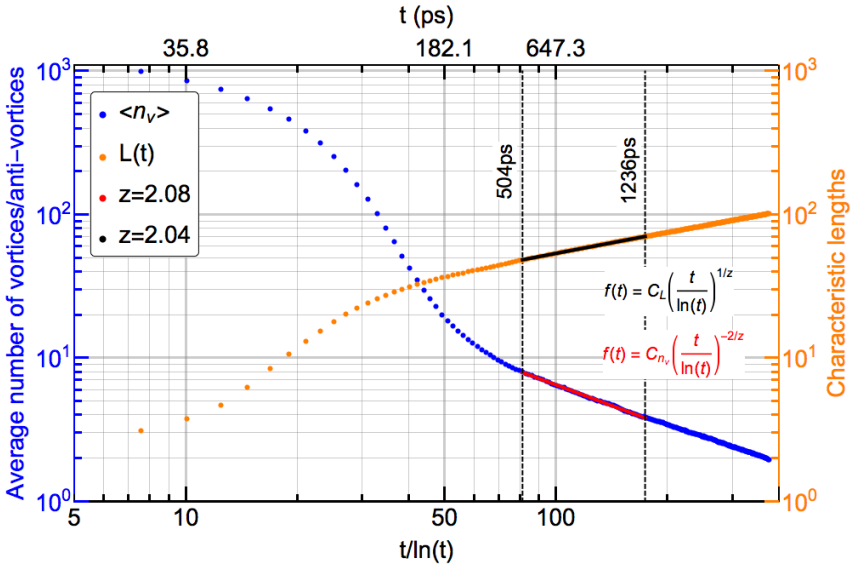

Figure 5.7: Dynamics of phase ordering.

5.2.6 Signature of Kibble-Zurek mechanism in Polaritons

If we have finite quench instead of infinity fast one we see the signature of the Kibble-Zurek mechanism across the same BKT type of phase transition as we seen in the thesis.

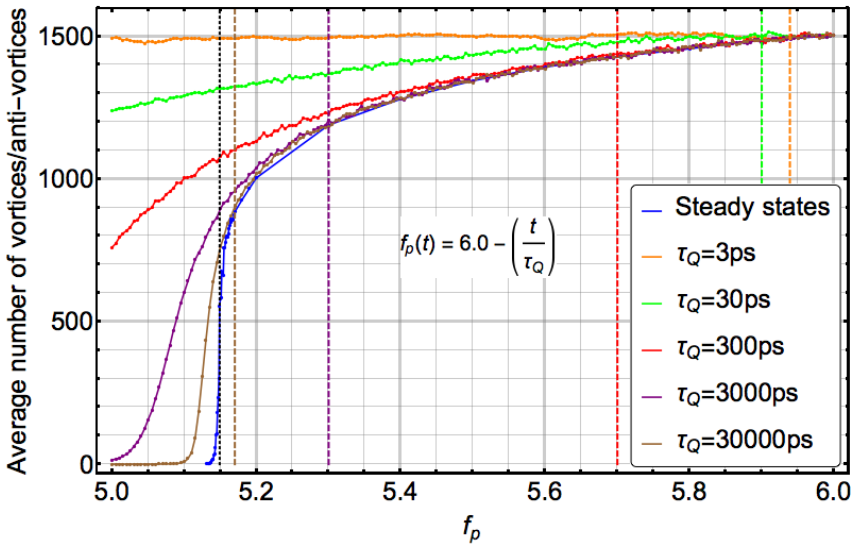

Figure 5.8: Average number of vortices for different quench times.

Bibliography

[1] Hui Deng, Hartmut Haug, and Yoshihisa Yamamoto. Exciton-polariton Bose-Einstein condensation. *Rev. Mod. Phys*, 82(2):1489–1537, May 2010. ISSN 0034-6861.

[2] L.P. Pitaevskii and S. Stringari. *Bose-Einstein Condensation*. International Series of Monographs on Physics. Clarendon Press, 2003. ISBN 9780198507192.

[3] Fritz London. The λ-phenomenon of liquid helium and the Bose-Einstein degeneracy. *Nature*, 141:643, 1938.

[4] M. H. Anderson, J. R. Ensher, M. R. Matthews, C. E. Wieman, and E. A. Cornell. Observation of Bose-Einstein condensation in a dilute atomic vapor. *Science*, 269(0):198, July 1995.

[5] D. G. Fried, T. C. Killian, L. Willmann, D. Landhuis, S. C. Moss, D. Kleppner, and T. J. Greytak. Bose-Einstein Condensation of Atomic Hydrogen. *Phys. Rev. Lett*, 81:3811–3814, Nov 1998.

[6] I Bloch, J. Dalibard, and W. Zwerger. Many-body physics with ultracold gases. *Rev. Mod. Phys*, 80(3):885–964, 2008.

[7] Jonathan Keeling and Natalia G Berloff. Exciton-polariton condensation. *Contemporary Physics*, 52(2):131–151, 2011.

[8] V. L. Berezinskii. Destruction of long-range order in one-dimensional and two-dimensional systems having a continuous symmetry group. II. Classical systems. *Soviet Physics JETP.,*, 34(3):610–616, 1972.

[9] J Kasprzak, M Richard, S Kundermann, a Baas, P Jeambrun, J M J Keeling, F M Marchetti, Marzena Hanna Szymanska, R André, J L Staehli, V Savona, P B Littlewood, B Deveaud, and Le Si Dang. Bose-Einstein condensation of

exciton polaritons. *Nature*, 443(7110):409–14, September 2006. ISSN 1476-4687.

[10] R. Stevenson, V. Astratov, M. Skolnick, D. Whittaker, M. Emam-Ismail, a. Tartakovskii, P. Savvidis, J. Baumberg, and J. Roberts. Continuous Wave Observation of Massive Polariton Redistribution by Stimulated Scattering in Semiconductor Microcavities. *Phys. Rev. Lett*, 85(17):3680–3683, October 2000. ISSN 0031-9007.

[11] A Einstein. Quantentheorie des einatomigen idealen Gases. *Sitzungber. Preuss. Akad. Wiss.*, 1(2):3–14, 1925.

[12] Fritz London. On the Bose-Einstein condensation. *Physical Review*, 54(11): 947, 1938.

[13] P Kapitza. Viscosity of liquid helium below the $\lambda-$point. *Nature*, 141:74, 1938.

[14] J. F. Allen and A Misener. Flow of liquid helium II. *Nature*, 141:75, 1938.

[15] K. B. Davis, M.-O. Mewes, M. R. Andrews, N. J. van Druten, D. S. Durfee, D. M. Kurn, and W. Ketterle. Bose-Einstein condensation in a gas of sodium atoms. *Phys. Rev. Lett*, 75(22):3969, November 1995.

[16] L. D. Landau. ON THE THEORY OF PHASE TRANSITIONS. *Zh. Eksp. Teor. Fiz*, 7:19–32, 1937.

[17] C.J. Pethick and H. Smith. *Bose-Einstein Condensation in Dilute Gases*. Cambridge Univ Press, 2008.

[18] L. Tisza. Transport Phenomena in Helium II. *Nature*, 141:913, 1938.

[19] R. P. Feynman. Superfluidity and Superconductivity. *Reviews of Modern Physics.*, 29:205, 1957. doi: http://dx.doi.org/10.1103/RevModPhys.29.205.

[20] D. R. Tilley and J. Tilley. *Superfluidity and superconductivity*. Institude of Physics Publishing, 1990.

[21] L. D. Landau. The theory of superfluidity of Helium II. *J. Phys. USSR*, 5:71, 1941.

[22] D. de Klerk and R. P. Hudson. Second sound propagation bellow 1°K. *Phys. Rev.*, 93(1):28–37, 1954.

[23] R. P. Feynman. Atomic Theory of Liquid Helium near absolute zero. *Phys. Rev.*, 91:1301–1308, 1953. doi: 10.1103/PhysRev.91.1301.

[24] R. P. Feynman. Atomic Theory of the Two-Fluid Model of Liquid Helium. *Phys. Rev.*, 94:262–277, 1954. doi: 10.1103/PhysRev.94.262.

[25] R. P. Feynman. Chapter II Application of Quantum Mechanics to Liquid Helium. *Prog. Low Temp. Phys., Progress in Low Temperature Physics*, 1: 17–53, 1955.

[26] R. P. Feynman and M. Cohen. Energy Spectrum of the Excitations in Liquid Helium. *Phys. Rev.*, 102:1189–1204, 1956. doi: 10.1103/PhysRev.102.1189.

[27] R. A. Cowley and A. D. B. Woods. Inelastic Scattering of Thermal Neutrons from Liquid Helium. *Can. J. Phys.*,, 49:177200.

[28] N. Bogolubov. On The Theory of Superfluidity. *J. Phys. USSR*, 11:23–32, 1947.

[29] R. Ozeri, N. Katz, J. Steinhauer, and N. Davidson. Colloquium: Bulk Bogoliubov excitations in Bose-Einstein condensate. *Reviews of Modern Physics*, 77 (1):187–205, 2005. doi: 10.1103/RevModPhys.77.187.

[30] A. J. Legget. Superfluidity. *Rev. Mod. Phys.*, 71(2):S318–S323, 1999. doi: 10.1103/RevModPhys.71.S318.

[31] D. R. Allum, P. V. E. McClintock, and A. Phillips. The Breakdown of Superfluidity in Liquid ^4He: An Experimental Test of Landaus Theory. *Phil. Trans. R. Soc. A.*, 284(1320):179–224, 1977.

[32] G. B. Hess and W. M. Fairbank. Measurements of Angular Momentum in Superfluid Helium. *Phys. Rev. Lett*, 19(5):216–218, 1967.

[33] R. J Donnelly. Quantized Vortices in Helium II. 1991.

[34] A. L. Fetter and A. A. Svidzinsky. Vortices in a trapped dilute Bose-Einstein condensate. *J. Phys: Condens. Matter,*, 13:R135, 2001. doi: 10.1088/09538984/13/12/201.

[35] A. L Fetter. Vortices and dynamics in trapped Bose-Einstein condensates. *Journal of Low Temperature Physics*, pages 1–15, 2010. doi: 10.1007/s10909-010-0202-7.

[36] B. P. Anderson. Resource article: Experiments with vortices in superfluid atomic gases. *Journal of Low Temperature Physics*, pages 1–29, 2010. doi: :10.1007/s10909-010-0224-1.

[37] Z. Hadzibabic and J. Dalibard. Two-dimensional Bose fluids: An atomic physics perscpective. 2009.

[38] D. S. Petrov, D. M. Gangardt, and G. V. Shlyapnikov. Low-dimensional trapped gases. *J. Phys. IV France*, 116:5–44, October 2004.

[39] A. Posazhennikova. Colloquium: Weakly interacting, dilute Bose gases in 2D. *Reviews of Modern Physics*, 78(4):11111134, 2006. doi: 10.1103/RevModPhys.78.1111.

[40] C. J. Pethink and H. Smith. *Bose-Einstein condensation in dilute gases*. Cambridge University Press, 2nd edition, 2008.

[41] J. M. Kosterlitz and D. J. Thouless. Long range order and metastability in two-dimensional solids and superfluids. *J. Phys. C: Solid State Phys.,*, 5(11): L124–L126, 1972.

[42] J. M. Kosterlitz and D. J. Thouless. Ordering, metastability and phase transitions in two-dimensional systems. *J. Phys. C: Solid State Phys.,*, 6(7):1181–1203, 1973.

[43] V. L. Berezinskii. Destruction of long-range order in one-dimensional and two-dimensional systems having a continuous symmetry group. I. Classical systems. *Soviet Physics JETP.*, 32(3):493–500, 1971.

[44] David R. Nelson and J. M. Kosterlitz. Universal Jump in the Superfluid Density of Two-Dimensional Superfluids. *Phys. Rev. Lett*, 39:1201–1205, Nov 1977. doi: 10.1103/PhysRevLett.39.1201.

[45] Daniel S. Fisher and P. C. Hohenberg. Dilute Bose gas in two dimensions. *Phys. Rev. B*, 37:4936–4943, Apr 1988. doi: 10.1103/PhysRevB.37.4936.

[46] N. Prokof'ev, O. Ruebenacker, and B. Svistunov. Critical point of a weakly interacting two-dimensional Bose gas. *Phys. Rev. Lett*, 87(27):270402, 2001. doi: 10.1103/PhysRevLett.87.270402.

[47] N. Prokof'ev and B. Svistunov. Two-dimensional weakly interacting Bose gas in the fluctuation region. *Phys. Rev. A*, 66(4):043608, 2002. doi: 10.1103/PhysRevA.66.043608.

[48] Paul M Chaikin and Tom C Lubensky. *Principles of condensed matter physics*, volume 1. Cambridge Univ Press, 2000.

[49] DJ Bishop and JD Reppy. Study of the Superfluid Transition in Two-Dimensional ^{4}He Films. *Phys. Rev. Lett*, 40(26):1727–1730, 1978.

[50] DJ Bishop and JD Reppy. Study of the superfluid transition in two-dimensional films. ^{4}He. *Phys. Rev. B*, 22(11):5171–5185, 1980.

[51] D. J. Resnick, J. C. Garland, J. T. Boyd, S. Shoemaker, and R. S. Newrock. Kosterlitz-Thouless transition in proximity-coupled superconducting arrays. *Phys. Rev. Lett*, 47(21):1542–1545, 1981.

[52] H. A. Rijken H. S. J. van der Zant and J. E. Mooij. Phase transition of frustrated two-dimensional Josephson junction arrays. *J. Low Temp. Phys.*, 82(1/2):6792, 1991.

[53] I. S. Yasnikov I. I. Lukashevich A. I. Safonov, S. A. Vasilyev and S. Jaakkola. Observation of quasicondensate in two-dimensional atomic hydrogen. *Phys. Rev. Lett*, 81(21):45454548, 1998.

[54] Zoran Hadzibabic, Peter Krüger, Marc Cheneau, Baptiste Battelier, and Jean Dalibard. Berezinskii-Kosterlitz-Thouless crossover in a trapped atomic gas. *Nature*, 441(7097):1118–21, June 2006. ISSN 1476-4687.

[55] V. Schweikhard, S. Tung, and E. A. Cornell. Vortex proliferation in the Berezinskii-Kosterlitz-Thouless regime on a two-dimensional lattice of Bose-Einstein condensates. *Phys. Rev. Lett*, 93(3):030401, 2007.

[56] D. Lobser L. Xia S. Tung, G. Lamporesi and E. A. Cornell. Observation of the presuperfluid regime in a two-dimensional Bose gas. *Phys. Rev. Lett*, 105 (23):230408, 2010.

[57] A. Ramanathan K. Helmerson P. Cladé, C. Ryu and W. D. Phillips. Observation of a 2D Bose gas: From thermal to quasicondensate to superfluid. *Phys. Rev. Lett*, 102(17):170401, 2009.

[58] J. M. Blatt, K. W. Böer, and W. Brandt. Bose-Einstein condensation of excitons. *Phys. Rev.*, 126:1691, 1962.

[59] S. A. Moskalenko. Reversible optico-hydrodynamic phenomena in a non-ideal exciton gas. *Sov. Phys.-Sol. State*, 4:199, 1962.

[60] L. V. Keldysh and Y. V. Kopaev. Possible instability of the semimetallic state toward coulomb interaction. *Sov. Phys.-Sol. State*, 6:2219, 1965.

[61] L. V. Keldysh and A. N. Kozlov. Collective properties of excitons in semiconductors. *Sov. Phys.-JETP*, 27:521, 1968.

[62] D. Snoke. Spontaneous Bose coherence of excitons and polaritons. *Science*, 298, 2002.

[63] L. V. Butov. Exciton condensation in coupled quantum wells. *Solid State Communications*, 127:89–98, 2003.

[64] Y. E. Lozovik and V. I. Yudson. Feasibility of superfluidity of paired spatially separated electrons and holes; a new superconductivity mechanism. *Sov. Phys.-JETP Lett.*, 22, 1975.

[65] Y. E. Lozovik and V. I. Yudson. A new mechanism for superconducitivity: paring between spatially separated electrons and holes. *Sov. Phys.-JETP Lett.*, 44, 1976.

[66] S. I. Shevchenko. Theory of superconductivity of systems with pairing of spatially separated electrons and holes. *Sov. J. Low. Temp. Phys.*, 2, 1976.

[67] S.I. Pekar. *Journ. Exp. Teor. Fiz.*, 33:1022, 1957.

[68] J. J. Hopfield. Theory of the contribution of excitons to the complex dielectric constant of crystals. *Physical Review*, 112(5):1555–1567, July 1958.

[69] V.M. Agranovich. *Optika i Spectr.*, 5(11), 1957.

[70] C. Weisbuch, M. Nishioka, A. Ishikawa, and Y. Arakawa. Observation of the coupled exciton-photon mode splitting in a semiconductor quantum microcavity. *Phys. Rev. Lett*, 69:3314, 1992.

[71] L. V. Butov. Condensation and pattern formation in cold exciton gases in coupled quantum wells. *J. Phys.: Condens. Matter*, 16, 2004.

[72] M. Gurioli, F. Bogani, D. S. Wiersma, Ph. Roussignol, G. Cassabois, G. Khitrova, and H. Gibbs. Experimental study of disorder in a semiconductor microcavity. *Phys. Rev. B*, 64:165309, Oct 2001. doi: 10.1103/PhysRevB.64.165309.

[73] I. Carusotto and C. Ciuti. Quantum fluids of light. *Rev. Mod. Phys*, May 2013.

[74] V. Savona, C. Piermarocchi, A. Quattropani, P. Schwendimann, and F. Tassone. Optical properties of microcavity polaritons. *Phase Transitions*, 68: 169–279, 2010.

[75] R. et al Houdré. Measurement of Cavity-Polariton dispersion curve from Angle-Resolved photoluminescence experiments. *Phys. Rev. Lett*, 73:2043, 1994.

[76] G. et al. Rochat. Excitonic bloch equations for a two-dimensional system of interacting excitons. *Phys. Rev. B*, 61:13856, 2000.

[77] C. Ciuti, P. Schwendimann, and A. Quattropani. Theory of polariton parametric interactions in semiconductor microcavities. *Semiconductor Science and Technology*, 18:s279, 2003.

[78] F. M. Marchetti and M. H Szymańska. *Vortices in polariton OPO superfluids*, volume Springer Series in Solid-State Sciences, chapter Exciton Polaritons in Microcavities: New Frontiers. Springer-Verlag, 2012.

[79] I. Carusotto and C. Ciuti. Quantum fluids of light. *Rev. Mod. Phys.*, 85: 299–366, Feb 2013. doi: 10.1103/RevModPhys.85.299.

[80] J. Baumberg, P. Savvidis, R. Stevenson, a. Tartakovskii, M. Skolnick, D. Whittaker, and J. Roberts. Parametric oscillation in a vertical microcavity: A polariton condensate or micro-optical parametric oscillation. *Phys. Rev. B*, 62 (24):R16247–R16250, December 2000. ISSN 0163-1829.

[81] A Baas, J.-Ph. Karr, M. Romanelli, A. Bramati, and E. Giacobino. Quantum Degeneracy of Microcavity Polaritons. *Phys. Rev. Lett*, 96:176401, May 2006.

[82] Iacopo Carusotto and Cristiano Ciuti. Spontaneous microcavity-polariton coherence across the parametric threshold: Quantum Monte Carlo studies. *Phys. Rev. B*, 72(12):125335, 2005.

[83] C. Ciuti, P. Schwendimann, B. Deveaud, and A. Quattropani. Theory of the angle-resonant polariton amplifier. *Phys. Rev. B*, 62:R4825, 2000.

[84] D. M. Whittaker. Classical treatment of parametric processes in a strong-coupling planar microcavity. *Phys. Rev. B*, 63:193305, 2001.

[85] D. M. Whittaker. Effects of polariton-energy renormalization in the microcavity optical parametric oscillator. *Phys. Rev. B*, 71(11):115301, 2005.

[86] N. A. Gippius, S. G. Tikhodeev, V. D. Kulakovskii, D. N. Krizhanovskii, and A. I. Tartakovskii. Nonlinear dynamics of polariton scattering in semiconductor microcavity: Bistability vs. stimulated scattering. *Europhysics Letters*, 67(6): 997, 2004.

[87] Marzena Hanna Szymańska, Jonathan Keeling, and Peter B Littlewood. Mean-field theory and fluctuation spectrum of a pumped decaying Bose-Fermi system across the quantum condensation transition. *Phys. Rev. B*, 75(19):195331, May 2007.

[88] MH Szymańska, FM Marchetti, and Daniele Sanvitto. Propagating wave packets and quantized currents in coherently driven polariton superfluids. *Phys. Rev. Lett*, 105(23):236402, 2010.

[89] FM Marchetti, Marzena Hanna Szymanska, C. Tejedor, and D. M. Whittaker. *Phys. Rev. Lett*, (6), August . ISSN 0031-9007.

[90] A Baas, J.-Ph. Karr, M. Romanelli, A. Bramati, and E. Giacobino. Optical bistability in semiconductor microcavities in the nondegenerate parametric oscillation regime:Analogy with the optical parametric oscillator. *Phys. Rev. B*, 70:161307, 2004.

[91] L. Cavigli and M. Gurioli. Optical bistability and laserlike emission in a semiconductor microcavity. *Phys. Rev. B*, 71:035317, January 2005.

[92] C. Ciuti and I. Carusotto. Quantum fluid effects and parametric instabilities in microcavities. *Phys. Status Solidi B*, 244:2224, 2005.

[93] M. Wouters and I. Carusotto. Parametric oscillation threshold of semiconductor microcavities in the strong coupling regime. *Phys. Rev. B*, 75:075332, 2007. doi: 10.1103/PhysRevB.75.075332.

[94] R. Butté, M.S. Skolnick, D.M. Whittaker, D. Bajoni, and J.S. Roberts. Dependence of stimulated scattering in semiconductor microcavities on pump power, angle, and energy. *Phys. Rev. B*, 68, 2003.

[95] D. M. Ceperley. *Rev. Mod. Phys*, 67:279, Aug 1995. doi: 10.1103/PhysRevA.90.023633.

[96] K. V. Houcke, E. Kozik, N. Prokov'ef, and B. Svistunov. *Phys. Procedia*, 6:95, 2010.

[97] N. Prokof'ev and B. Svistunov. *Phys. Rev. B*, 77:125101, 2008.

[98] U. Schollwöck. *Reviews of Modern Physics*, 77:259, 2005.

[99] C. W. Gardiner and P. Zoller. *Quantum noise.* Springer-Verlag, Berlin, 2004.

[100] H. Risken. *The Fokker-Planck Equation: Methods of Solutions and Applications.* Springer-Verlag, Berlin, 1996.

[101] C. W. Gardiner. *Handbook of Stochastic Methods.* Springer-Verlag, Berlin, 1985.

[102] K Vogel and H Risken. Quasiprobability distributions in dispersive optical bistability. *Phys. Rev. A*, 39(9):4675–4683, 1989.

[103] M. Wouters and V. Savona. Stochastic classical field model for polariton condensates. *Phys. Rev. B*, 79, Apr 2009.

[104] A. Sinatra, C. Lobo, and Y. Castin. *J. Phys. B*, 35:3559, 2002.

[105] I. Carusotto, D. Gerace, H. Tureci, S. De Liberato, C. Ciuti, and a. Imamolu. Fermionized Photons in an Array of Driven Dissipative Nonlinear Cavities. *Phys. Rev. Lett*, 103(3):033601, July 2009. ISSN 0031-9007.

[106] Michael J. Hartmann, Fernando G. S. L. Brandao, and Martin B. Plenio. Quantum Many-Body Phenomena in Coupled Cavity Arrays. *Laser and Photonic Reviews*, 2(6):527—-556, August 2008.

[107] A. Amo, Jérôme Lefrère, Simon Pigeon, Claire Adrados, Cristiano Ciuti, Iacopo Carusotto, Romuald Houdré, Elisabeth Giacobino, and A. Bramati. Superfluidity of polaritons in semiconductor microcavities. *Nature Physics*, 5(11): 805–810, September 2009. ISSN 1745-2473.

[108] A. Amo, D Sanvitto, F P Laussy, D Ballarini, E del Valle, M D Martin, a Lemaître, J Bloch, D N Krizhanovskii, M S Skolnick, C Tejedor, and L Viña. Collective fluid dynamics of a polariton condensate in a semiconductor microcavity. *Nature*, 457(7227):291–5, January 2009. ISSN 1476-4687.

[109] D Sanvitto, F. M. Marchetti, Marzena Hanna Szymanska, G. Tosi, M. Baudisch, F. P. Laussy, D. N. Krizhanovskii, M. S. Skolnick, L. Marrucci, Aristide Lemaître, J. Bloch, C. Tejedor, and L. Viña. Persistent currents and quantized vortices in a polariton superfluid. *Nature Physics*, 6(7):527–533, May 2010. ISSN 1745-2473.

[110] Marchetti, F. M. and Szymańska, M. H. and Tejedor, C. and Whittaker, D. M. Spontaneous and Triggered Vortices in Polariton Optical-Parametric-Oscillator Superfluids. *Phys. Rev. Lett*, 105(6):063902, August 2010. ISSN 0031-9007.

[111] G. Tosi, F. M. Marchetti, D Sanvitto, C. Antón, Marzena Hanna Szymanska, A. Berceanu, C. Tejedor, L. Marrucci, Aristide Lemaître, J. Bloch, and L. Viña. Onset and Dynamics of Vortex-Antivortex Pairs in Polariton Optical Parametric Oscillator Superfluids. *Phys. Rev. Lett*, 107(3):036401, July 2011. ISSN 0031-9007.

[112] Georgios Roumpos and Yoshihisa Yamamoto. The Berezinskii–Kosterlitz–Thouless Phase Transition in Exciton–Polariton Condensates. In *Exciton Polaritons in Microcavities*, pages 85–146. Springer, 2012.

[113] Ehud Altman, Lukas M. Sieberer, Leiming Chen, Sebastian Diehl, and John Toner. Two-dimensional superfluidity of exciton-polaritons requires strong anisotropy. November 2013.

[114] G. R. Dennis, J. J. Hope, and M. T. Johnsson. XMDS2: Fast, scalable simulation of coupled stochastic partial differential equations. *Computer Physics Communications*, 184(1):201–208, April 2012.

[115] Lydie Ferrier et al. Interactions in Confined Polariton Condensates. *Phys. Rev. Lett*, 106:126401, Mar 2011. doi: 10.1103/PhysRevLett.106.126401.

[116] Michiel Wouters and Iacopo Carusotto. Goldstone mode of optical parametric oscillators in planar semiconductor microcavities in the strong-coupling regime. *Phys. Rev. A*, 76(4):043807, October 2007. ISSN 1050-2947.

[117] Alessio Chiocchetta and Iacopo Carusotto. Quantum Langevin model for nonequilibrium condensation. *Phys. Rev. A*, 90:023633, Aug 2014. doi: 10.1103/PhysRevA.90.023633.

[118] Lukas M. Sieberer, S D Huber, Ehud Altman, and Sebastian Diehl. Nonequilibrium Functional Renormalization for Driven-Dissipative Bose-Einstein Condensation. 2013.

[119] K Vogel and H Risken. Quantum-tunneling rates and stationary solutions in dispersive optical bistability. *Phys. Rev. A*, 38(5), 1988.

[120] Christopher J. Foster, PB Blakie, and Matthew J. Davis. Vortex pairing in two-dimensional Bose gases. *Phys. Rev. A*, 81(2):023623, February 2010. ISSN 1050-2947.

[121] Luca Giorgetti, Iacopo Carusotto, and Yvan Castin. Semiclassical field method for the equilibrium Bose gas and application to thermal vortices in two dimensions. *Phys. Rev. A*, 76(1):013613, 2007. doi: 10.1103/PhysRevA.76.013613.

[122] Dario Gerace and Iacopo Carusotto. Analog Hawking radiation from an acoustic black hole in a flowing polariton superfluid. *Phys. Rev. B*, pages 29–31, 2012.

[123] Georgios Roumpos, Michael Lohse, Wolfgang H Nitsche, Jonathan Keeling, Marzena Hanna Szymanska, Peter B Littlewood, Andreas Loffler, Sven Höfling, Lukas Worschech, Alfred Forchel, and Yoshihisa Yamamoto. Power-law decay of the spatial correlation function in exciton-polariton condensates. *Proceedings of the National Academy of Sciences*, 109(17):6467–72, April 2012. ISSN 1091-6490.

[124] R Spano, J Cuadra, C Lingg, D Sanvitto, MD Martin, PR Eastham, M Van Der Poel, J. Hvam, and L Viña. Build up of off-diagonal long-range order in microcavity exciton-polaritons across the parametric threshold. *Optics express*, 21(9):1–5, 2013.

[125] J. Keeling, F. Marchetti, M. Szymańska, and P. Littlewood. Collective coherence in planar semiconductor microcavities. *Semicond. Sci. Technol.*, 22:R1, 2007.